UNIVERSIDAD COMPLUTENSE DE MADRID

FACULTAD DE CIENCIAS BIOLÓGICAS

Departamento de Bioquímica y Biología Molecular I

TESIS DOCTORAL

Explorando el plegamiento metallo-beta-lactamasa en el genoma de *Acinetobacter baumanni*

MEMORIA PARA OPTAR AL GRADO DE DOCTOR

PRESENTADA POR

Fabiola Rodríguez Calviño

Director

Antonio Romero Garrido

Madrid, 2012

UNIVERSIDAD COMPLUTENSE DE MADRID

FACULTAD DE CIENCIAS

DEPARTAMENTO DE BIOQUÍMICA Y BIOLOGÍA MOLECULAR I

EXPLORANDO EL PLEGAMIENTO METALLO-BETA-LACTAMASA EN EL GENOMA DE *Acinetobacter baumannii*

TESIS DOCTORAL

Mención Europea

FABIOLA RODRÍGUEZ CALVIÑO

TUTOR ACADÉMICO

Julián Perera González

DIRECTOR DE TESIS

Antonio Romero Garrido

UNIVERSIDAD COMPLUTENSE DE MADRID

FACULTAD DE CIENCIAS BIOLÓGICAS

DEPARTAMENTO DE BIOQUÍMICA Y BIOLOGÍA MOLECULAR I

EXPLORING THE METALLO-β-LACTAMASE FOLD IN THE GENOME OF *Acinetobacter baumannii*

TESIS DOCTORAL

Mención Europea

FABIOLA RODRÍGUEZ CALVIÑO

TUTOR ACADÉMICO

Julián Perera González

DIRECTOR DE TESIS

Antonio Romero Garrido

Madrid, 2012

INDEX

I. RESUMEN

II. INTRODUCTION

1. Acinetobacter baumannii
2. β-lactam antibiotics and different resistance determinants
3. β-lactamases, antibiotic-modifying enzymes
4. Metallo β-lactamase superfamily
   - 4.1. GROUP 1: CLASS B β-LACTAMASES (METALLO-β-LACTAMASES, MBLs)
   - 4.2. GROUP 2: GLIOXALASE II
   - 4.3. GROUP 4: tRNASE Z-FAMILY
   - 4.4. GROUP 5: TYPE II POLYKETIDE SYNTHASES
   - 4.5. GROUP 10: PhnP PROTEIN
   - 4.6. GROUP 12: N-ACYL HOMOSERINE LACTONE HYDROLASE
   - 4.7. GROUP 13: ALKYL SULFATASE
   - 4.8. GROUP 15: METHYL PARATHION HYDROLASE
   - 4.9. GROUP 16: 3´,5´-CYCLIC NUCLEOTIDE PHOSPHODIESTERASE
   - 4.10. GROUP 0: PqsE ENZYME

III. OBJECTIVES

IV. MATERIALS AND METHODS

1. Cloning
   - 1.1. PCR AMPLIFICATION AND SUBCLONING
   - 1.2. AGAROSE GEL ELECTROPHORESIS
   - 1.3. DNA PURIFICATION AND RESTRICTION ENZYME DIGESTION
   - 1.4. DNA LIGATION
   - 1.5. DNA MUTAGENESIS
   - 1.6. DNA TRANSFORMATION
2. Protein expression and purification
   - 2.1. EXPRESSION
   - 2.2. PROTEIN PURIFICATION OF GST-TAGGED PROTEINS
   - 2.3. EXPRESSION OF SEMET-LABELED PROTEINS
3. Biophysical and Biochemical Protein Characterization
   - 3.1. ANALYTICAL GEL FILTRATION
   - 3.2. ANALYTICAL ULTRACENTRIFUGATION
   - 3.3. MASS SPECTROMETRY
4. Protein crystallization
   - 4.1. CRYOGENIC PROTECTION OF THE CRYSTALS
5. Structure determination
   - 5.1. X-RAY DIFFRACTION AND ANOMALOUS SCATTERING

5.2. DATA COLLECTION
5.3. DATA PROCESSING
5.4. CRYSTALLOGRAPHIC COMPUTING PROGRAMS AND MODEL REFINEMENT
6. *Functional assays*
6.1. ENZYMATIC ACTIVITY
6.1.1. ANALYSIS OF β-LACTAMASE ACTIVITY
6.1.2. ANALYSIS OF GLIOXALASE II ACTIVITY
6.1.3. ANALYSIS OF PHOSPHATASE ACTIVITY
6.1.4. ANALYSIS OF PHOSPHODIESTERASE ACTIVITY
6.1.5. ANALYSIS OF ESTERASE ACTIVITY
6.1.6. ANALYSIS OF THIOESTERASE ACTIVITY
6.2. ANTIBIOTIC SUSCEPTIBILITY TEST
6.2.1. QUANTITATIVE RT-PCR

V. RESULTS

CHAPTER I aMBL-1

1. *Sequence analysis*
1.1. *SEQUENCE ANALYSIS*
2. *Cloning*
3. *Protein expression and purification*
3.1. PROTEIN EXPRESSION
3.2. PROTEIN PURIFICATION
3.3. PROTEIN IDENTIFICATION BY MALDI-TOF-MS
3.4. EXPRESSION OF SeMET-LABELED PROTEIN
4. *Biophysical characterization*
4.1. ANALYTICAL GEL FILTRATION
4.2. ANALYTICAL ULTRACENTRIFUGATION
5. *Protein crystallization*
6. *Structure determination*
6.1. NATIVE DATASETS
6.1.1. DATA COLLECTION AND PROCESSING
6.2. DERIVATIVE DATASETS
6.2.1. DATA COLLECTION AND PROCESSING
6.2.2. STRUCTURE DETERMINATION AND REFINEMENT
6.3. VALIDATION OF THE STRUCTURE
7. *Architecture of aMBL-1*
7.1. OVERALL FOLDING
7.2. DIMER INTERFACE
7.3. PUTATIVE ACTIVE SITE
7.4. CRYSTAL PACKING IN THE TWO CRYSTAL FORMS
7.5. FUNCTIONAL ASSAYS
7.5.1. SUSCEPTIBILITY TESTING
7.5.2. KINETIC EXPERIMENTS

CHAPTER II **aMBL-2**

1. *Sequence analysis*
   - *1.1. ALIGNMENT AND SEQUENCE ANALYSIS*
2. *Cloning*
3. *Protein expression and purification*
   - *3.1. PROTEIN EXPRESSION*
   - *3.2. PROTEIN PURIFICATION*
   - *3.3. PROTEIN IDENTIFICATION BY MALDI-TOF-MS*
   - *3.4. EXPRESSION OF SeMET-LABELED PROTEIN*
4. *Biophysical characterization*
   - *4.1. ANALYTICAL GEL FILTRATION*
   - *4.2. ANALYTICAL ULTRACENTRIFUGATION*
5. *Protein crystallization*
6. *Structure determination*
   - *6.1. NATIVE DATASETS*
     - *6.1.1. DATA COLLECTION AND PROCESSING*
   - *6.2. DERIVATIVE DATASETS*
     - *6.2.1. DATA COLLECTION AND PROCESSING*
   - *6.3. STRUCTURE DETERMINATION AND REFINEMENT*
   - *6.4. VALIDATION OF THE STRUCTURE*
7. *Architecture of aMBL-2*
   - *7.1. OVERALL FOLDING*
   - *7.2. ACTIVE SITE*
   - *7.3. QUATERNARY STRUCTURE*
8. *Functional assays*
   - *8.1. MICROBIOLOGICAL ASSAYS*
   - *8.2. ENZYMATIC ACTIVITY*

VI. DISCUSSION

CHAPTER I **aMBL-1**

1. *Overall fold*
2. *Putative active site*
3. *Putative binding site*
4. *Comparison with other members of the MBL superfamily / Classification*

CHAPTER II **aMBL-2**

1. *Overall fold*
2. *Putative active site*

1. *Overall fold*
2. *Dimerization*
3. *Active site*

VII. CONCLUSIONES

VIII. BIBLIOGRAPHY

FIGURES

FIGURE 1: MODEL OF VESICLE BIOGENESIS.
FIGURE 2: HYDROLYSIS OF THE ESSENTIAL FOUR-MEMBER LACTAM RING OF A B-LACTAM ANTIBIOTIC BY A B-LACTAMASE.
FIGURE 3: METALLO-B-LACTAMASE SUPERFAMILY OVERALL STRUCTURES.
FIGURE 4: SCHEMATIC REPRESENTATION OF THE DOMAIN ORGANIZATION OF THE METALLO-B-LACTAMASE SUPERFAMILY GROUPS.
FIGURE 5: ACTIVE SITES OF THE THREE SUBCLASSES.
FIGURE 6: THE GLYOXALASE SYSTEM.
FIGURE 7: COMPARISON OF THE YCBL METAL BINDING SITE (PDB CODE 2XF4) WITH THE DIION SITE IN GLX2 (PDB CODE 2QED) BOTH FROM *S. TYPHIMURIUM*.
FIGURE 8: THE METHYL PARATHION HYDROLASE ACTIVE SITE.
FIGURE 9: THE IRON BINDING SITE IN PQSE WITH THE COPURIFIED BENZOATE-SHAPED LIGAND (BEZ).
FIGURE 10: SCHEMATIC REPRESENTATION OF THE PGEX6P-2 VECTOR AND THE GENE SEQUENCES CORRESPONDING TO AMBL-1 AND AMBL-2.
FIGURE 11: THE SKETCH ON THE LEFT ILLUSTRATES THE PRINCIPLE OF THE SITTING-DROP VAPOUR DIFFUSION TECHNIQUE.
FIGURE 12: ANALYSIS OF THE AMBL-1 AMINO ACIDS SEQUENCE.
FIGURE 13: PURIFICATION OF AMBL-1.
FIGURE 14: MASS SPECTRA OF THE NATIVE (BROWN) AND THE SEMET LABELED (GREEN) AMBL-1.
FIGURE 15: ELUTION PROFILE OF AMBL-1 (BLACK LINE).
FIGURE 16: ANALYTICAL ULTRACENTRIFUGATION EXPERIMENTS OF AMBL-1.
FIGURE 17: INITIAL CRYSTAL HITS OF AMBL-1 FROM THE COMMERCIAL CRYSTALLIZATION KITS.
FIGURE 18: ORTHORHOMBIC CRYSTALS OBTAINED USING THE HOME MADE E10 CONDITION FROM CUSTOM I.
FIGURE 19: DIFFRACTION PATTERN OF THE NATIVE ORTHORHOMBIC CRYSTAL FORM OF AMBL-1.
FIGURE 20: EXPERIMENTAL ANOMALOUS SCATTERING CURVES FROM A CRYSTAL OF SE-MET LABELED AMBL-1.
FIGURE 21: RESULTING ELECTRON DENSITY MAP.
FIGURE 22: (A) 2Fo-Fc ELECTRON DENSITY MAP IN THE REGION OF ASN57 CONTOURED AT 1.2σ. (B) THE QUALITY OF THE FINAL REFINED MODEL OF AMBL-1.
FIGURE 23: STRUCTURE OF AMBL-1.
FIGURE 24: RAMACHANDRAN PLOTS FOR THE B-BULGES, SHOWING THE Ψ/Φ ANGLES OF THE RESIDUES INVOLVED.
FIGURE 25: DIMER INTERFACE OF AMBL-1.
FIGURE 26: (A) PUTATIVE ACTIVE SITE OF AMBL-1. (B) STRUCTURAL ALIGNMENT OF THE PUTATIVE ACTIVE SITE OF AMBL-1 WITH THE METAL BINDING MOTIF OF THE NDM.
FIGURE 27: PUTATIVE ACTIVE SITE OF AMBL-1.
FIGURE 28: LIGPLOT REPRESENTATION OF THE HYDROGEN-BOND NETWORK INVOLVING THE BENZOATE IN THE PUTATIVE ACTIVE SITE OF AMBL-1.
FIGURE 29: ARRANGEMENT OF THE AMBL-1 DIMERS IN THE TWO CRYSTAL FORMS
FIGURE 30: SUPERPOSITION OF THE Cα TRACES OF THE DIMERIC AMBL-1 OBSERVED IN THE TWO DIFFERENT CRYSTAL FORMS
FIGURE 31: SECONDARY STRUCTURE PREDICTION OF AMBL-2.
FIGURE 32: AGAROSE GELS.
FIGURE 33: PURIFICATION OF AMBL-2.
FIGURE 34: MASS SPECTRA OF THE NATIVE AND THE SEMET LABELED AMBL-2.
FIGURE 35: ELUTION PROFILE OF AMBL-2.
FIGURE 36: ANALYTICAL ULTRACENTRIFUGATION EXPERIMENTS OF AMBL-2.
FIGURE 37: CRYSTALS OF AMBL-2 OBTAINED WITH THE OPTIMIZED CRYSTALLIZATION SOLUTION.
FIGURE 38: SELF ROTATION FUNCTION AT CHI = 180° AND 90° CALCULATED FOR THE P1 NATIVE DATA OF AMBL-2.
FIGURE 39: EXPERIMENTAL ANOMALOUS SCATTERING FROM A CRYSTAL OF SE-MET LABELED AMBL-2.
FIGURE 40: DIFFRACTION PATTERN OF THE SEMET LABELED TRICLINIC CRYSTAL OF AMBL-2.
FIGURE 41: SECTIONS OF THE ANOMALOUS DIFFERENCE PATTERSON MAP CALCULATED FOR THE PEAK DATA OF THE SEMET LABELED AMBL-2 CRYSTAL.

FIGURE 42: RAMACHANDRAN PLOT FOR EACH CHAIN (A, B, C AND D) OF aMBL-2.
FIGURE 43: STRUCTURE OF AMBL-2.
FIGURE 44: ELECTRON DENSITY IN THE ACTIVE SITE OF AMBL-2 SHOWING THE 2Fo-Fc MAP (CONTOURED AT 1.2σ).
FIGURE 45: SUPERPOSITION OF THE HIGH AFFINITY ZINC BINDING SITE OF L1 FROM S. MALTOPHILIA AND AMBL-2.
FIGURE 46: QUATERNARY STRUCTURE OF AMBL-2.
FIGURE 47: ZOOM OF THE DIMERIZATION AREA BETWEEN CHAINS A (DARK BLUE) AND B (LIGHT BLUE).
FIGURE 48: ANTIBIOTIC DEGRADATION ASSAYS BY AN ADAPTATION OF THE MASUDA METHOD.
FIGURE 49: STRUCTURAL ALIGNMENT AND SUPERPOSITION OF THE ACTIVE SITE RESIDUES IN THE METAL BINDING SITE.
FIGURE 50: TUNNELS AT THE PUTATIVE BINDING SITE OF AMBL-1.
FIGURE 51: STRUCTURAL ALIGNMENT OF aMBL-1 (BLUE, P21, AND GREEN, P212121), PSQE (RED), AND ST1585 (YELLOW).
FIGURE 52: RIBBON REPRESENTATION OF THE QUATERNARY STRUCTURE
FIGURE 53: STRUCTURAL ALIGNMENT OF THE MONOMERS OF aMBL-2 (BLUE) AND L1 (GREEN).
FIGURE 54: SEQUENCE ALIGNMENT OF CLASS B B-LACTAMASE ENZYMES.
FIGURE 55: STRUCTURAL ALIGNMENT OF THE MONOMERS OF aMBL-1 (YELLOW) AND aMBL-2 (BLUE).
FIGURE 56: SEQUENCE ALIGNMENT OF THE ACTIVE SITE OF aMBL-1 AND aMBL-2 ENZYMES.

TABLES

TABLE 1: B-LACTAMASE CLASSIFICATION SYSTEMS.
TABLE 2: METALLO-B-LACTAMASE SUPERFAMILY CLASSIFICATION.
TABLE 3: ENZYMES FOR DNA-SUBCLONING.
TABLE 4: OLIGONUCLEOTIDES FOR DNA-SUBCLONING.
TABLE 5: DATA COLLECTION
TABLE 6: ACTIVITY TESTS WITH GENERAL CHROMOGENIC SUBSTRATES
TABLE 7: DATA COLLECTION STATISTICS FOR AMBL-1 CRYSTALS
TABLE 8: DATA COLLECTION STATISTICS FOR SEMET LABELED AMBL-1 CRYSTALS
TABLE 9: FINAL COORDINATES AND OCCUPANCIES OF THE SE ATOMS
TABLE 10: REFINEMENT ANALYSIS OF AMBL-1
TABLE 11: CONTACTS BETWEEN MONOMERS AT THE DIMER INTERFACE
TABLE 12: DATA COLLECTION STATISTICS FOR AMBL-2
TABLE 13: FINAL COORDINATES AND OCCUPANCIES OF THE SE ATOMS
TABLE 14: REFINEMENT ANALYSIS OF AMBL-2
TABLE 15: MICS OF A. BAUMANNII STRAINS WITH CLONED GENES USED IN THIS WORK
TABLE 16: KINETIC PARAMETERS OF AMBL-2 AGAINST SOME B-LACTAMS
TABLE 17: BEST MATCHES FOR aMBL-1 ACCORDING TO DALI

RESUMEN

RESUMEN

Acinetobacter baumannii fue considerado siempre como un patógeno de relativa baja virulencia, pero durante las dos últimas décadas, este microorganismo oportunista ha emergido como uno de los mayores problemas encarados por el sistema clínico en hospitales de todo el mundo. Como consecuencia inevitable de la presión selectiva impuesta por el uso abusivo de antibióticos en el tratamiento de infecciones, se han descrito cepas clínicas multirresistentes de *A. baumannii*, con una alta capacidad para desarrollar diferentes mecanismos de resistencia.

Atendiendo a los antibióticos β-lactámicos, el principal mecanismo de resistencia es la producción de β-lactamasas, que son enzimas bacterianas capaces de degradar el antibiótico antes de que alcance su diana en la bacteria, permitiéndole a ésta una gran facilidad de adaptación al medio hospitalario y de crecimiento en asociación con su hospedador humano. Estas enzimas pueden ser clasificadas en diferentes grupos en base a su secuencia de amino ácidos o acorde a su perfil hidrolítico de sustratos e inhibidores. Dentro de esa clasificación, en este trabajo nos hemos centrado en la clase B de las β-lactamasas, que son un grupo de proteínas con una conservada estructura tridimensional, pertenecientes a una conocida superfamilia de proteínas, las metallo-β-lactamasas.

Esta superfamilia de las metallo-β-lactamasas fue por primera vez descrita por Neuwald en 1997. Sus miembros presentan una ubicua distribución a través de los tres dominios biológicos, lo cual sugiere una gran importancia funcional así como un origen ancestral. Son proteínas que se caracterizan por compartir un estable plegamiento tridimensional compuesto por cuatro regiones bien definidas, que son dos grupos centrales de láminas-beta rodeados a ambos lados por αlfa-hélices que quedan expuestas al solvente. En todas las estructuras conocidas hasta el momento, el sitio activo se sitúa entre los dos grupos de láminas beta enfrentadas, dónde uno o dos átomos metálicos, preferencialmente zinc, queda unido por una fuerte interacción con los residuos altamente conservados que confeccionan el motivo característico de esta superfamilia en su sitio activo. Este canónico plegamiento representa el mínimo dominio necesario para definir a una proteína funcional dentro de esta superfamilia, aunque gracias a diversos dominios adicionales el rango de reacciones químicas que estas proteínas pueden catalizar ha sido ampliamente extendido. Los diversos miembros fueron clasificados en 16 grupos, describiendo su variedad estructural adicional al plegamiento canónico y sus distintas funciones biológicas. Recientemente dentro de esta clasificación, un nuevo grupo 0 fue definido, el cual incluye dos enzimas sin actividad conocida por el momento, pero con un característico dominio adicional al canónico de metalo-β-lactamasa.

Con el presente estudio, quisimos identificar nuevos posibles miembros de esta superfamilia dentro del genoma de *A. baumannii*, que a su vez pudieran intervenir de algún modo en el mecanismo general de resistencia de este conocido patógeno. A través de un meticuloso análisis de su genoma, dos genes fueron identificados, ABAYE3862 y ABAYE0164, codificando para dos proteínas putativas pertenecientes a la superfamilia de las metalo-β-lactamasas. La predicción de su estructura secundaria sugirió el canónico plegamiento en αββα de esta superfamilia, llamando nuestra atención el que ninguna de ellas presentase el conservado motivo (HXHXD/H) de unión a zinc en el sitio activo. Estas dos proteínas fueron bautizadas como aMBL-1 y aMBL-2, respectivamente, de *acinetobacter Metallo*-Beta-Lactamase.

Esos dos genes, ABAYE3862 y ABAYE0164, fueron clonados a partir del ADN genómico de *A.baumannii* y las respectivas proteínas a las que codifican, aMBL-1 y aMBL-2, fueron caracterizadas mediante las correspondientes técnicas biofísicas y bioquímicas. Además, su estructura tridimensional fue resuelta mediante cristalografía de rayos X, haciendo uso para ello de técnicas de faseo experimental, habiendo marcado previamente ambas proteínas con átomos pesados.

Estas estructuras representan los primeros datos estructurales de dos nuevos miembros de esta superfamilia ya que ambas proteínas muestran el típico plegamiento metalo-beta-lactamasa aunque con ciertas particularidades. Ambas exhiben un estado de oligomerización mayoritariamente dimérico en solución, con un alongado C-terminal. En el caso de aMBL-1 representa un dominio adicional que por su similitud con los restantes miembros del grupo 0 de la MBL superfamilia podría darnos algún indicio del posible papel de aMBL-1 como transportador de señales extracelulares dentro de la bacteria. En cambio para aMBL-2, esa extensión del C-terminal es la que facilita la formación del dímero dejando los dos sitios activos de cada monómero enfrentados dentro de la U que forman ambas cadenas.

Además, los residuos del presunto sitio activo de aMBL-1 difieren ampliamente del canónico, mientras que los de aMBL-2 se asemejan bastante al motivo (HXHXD/H) de unión a zinc e incluso un átomo del metal pudo ser definido (aunque con baja ocupación) en su estructura. Con aMBL-2 creemos haber contribuido en la comprensión de la evolución de la diversidad molecular que caracteriza a esta superfamilia. La proteína aMBL-2 podría definirse como una beta-lactamasa de clase B ancestral que *Acinetobacter* aún conservar en su genoma, con un sitio activo inmaduro y una modesta actividad hidrolítica frente a los antibióticos beta-lactámicos.

INTRODUCTION

II. INTRODUCTION

1. Acinetobacter baumannii

Acinetobacter baumannii was considered a low-grade commensal microorganism and a potential opportunistic pathogen, but over the last 20 years, it has emerged as a major cause of nosocomial infections associated with significant morbidity and mortality in hospitalized patients [1-2]. This fact has been attributed to the worldwide expansion of Intensive Care Units that led to a change in the type of infections caused by *Acinetobacter*, and the emergence of multidrug-resistant (MDR) strains to many classes of antibiotics [3-7].

Genetic determinants of antimicrobial resistance have been described extensively as well as some of the mechanisms by which *A. baumannii* regulates its antibiotic resistance profile. But little is known about whether resistance phenotypes are constitutive and therefore static, or whether resistance is modulated in response to external signals. In 2010, Hood *et al* [8], using a proteomic-based approach and transcriptional analyses, established that *A. baumannii* regulates its intrinsic antibiotic resistance profile in response to a commonly encountered environmental signal, underscoring the adaptability of this organism to growth in the hospital environment and within its host. They found that monovalent cations are important environmental signals sensed by *A. baumannii*. In particular, NaCl in physiological concentrations was identified as the responsible for signal sensing thus altering the increased-resistance phenotype of *A. baumannii* [8].

The human isolated *A. baumannii* AYE is a multidrug resistant strain (MDR) responsible for an outbreak in France in 2001 [9]. Its genome, made of a single chromosome of 3.9 Mb and 4 plasmids, was sequenced with the main goal of identifying the genes concentrated on a resistance island of ca. 86-kb long. Whole-genome sequencing approaches comparing MRD *A. baumannii* isolates with a susceptible strain as *Acinetobacter baylyi ADP1* have highlighted additional genetic features that potentially contribute to antibiotic resistance suggesting that *A. baumannii* has acquired an extensive regulatory capacity as a consequence of growth in association with the human host [10].

2. β-lactam antibiotics and different resistance determinants

The introduction of β-lactam antibiotics into the health care system represented one of the most important contributions to medical science [11].

β-lactam antibiotics interfere with the final step of peptidoglycan synthesis [12]. The β-lactam ring is sterically similar to the D-Ala-D-Ala peptide of the cell wall peptidoglycan skeleton. Hence, in the presence of the antibiotic, the penicillin binding proteins (PBPs) form a lethal covalent penicilloyl–enzyme complex that blocks the normal transpeptidation reaction [13]. The acylated PBP cannot hydrolyze the β-lactam and subsequent steps in the peptidoglycan synthesis are blocked while the action of autolysins destroying the existing cell wall causes bacteriolysis yielding a wall unable to withstand osmotic forces [14-16].

Today, β-lactams remain the most widely used antibiotics but unfortunately, once an antibiotic is proven to be effective and enters widespread human therapeutic use, its days are numbered. The use of subtherapeutic levels of antibiotics could induce resistance [17], given the large number of bacteria in an infection cycle, the rapid generation time and the intrinsic rate of mutation [18]. If one of those mutations confers resistance to an applied antibiotic, whereas all sensitive bacteria are killed, the resistant one will grow, fill the space vacated by its dead neighbors and become the dominant variant in the population [18]. Antibiotics might therefore have a central role in the evolution of resistance other than simply providing selective pressure [19].

The efficacy of β-lactam antibiotics is dependent on accessibility to its targets, the degree of resistance to enzymatic inactivation by β-lactamases and the ability of β-lactam to inhibit the target PBPs. Altering one or a combination of these parameters may result in bacterial resistance [20].

A. baumannii has been able to develop primary mechanisms of resistance against most of antimicrobial agents [21] that can be summarized as follows:

a) Alteration of the antibiotic target site. PBPs that exhibit low affinity for β-lactam antibiotics and are relatively resistant to inactivation by penicillins. They will be able to assume the functions of other PBPs when the latter are inactivated.

b) Altered permeability of the membrane. Reduced expression of outer membrane proteins (OMPs) restricts the entry of certain β-lactams into the periplasmic space of Gram-negative bacteria and hence, access to PBPs on the inner membrane. Pumping out of drugs, through efflux pumps, faster than they diffuse in, resulting in lower intrabacterial antibiotic concentrations which is known to be ineffective against the bacteria.

c) Extracellular secretion of products by vesicles, which enable the extracellular dispersal of specific proteins as part of complexes of proteins and lipids. These complexes can act synergistically to activate toxic and immune pathways in the host. Vesicles can also help bacteria carve out a niche in the environment by modulating interactions between neighboring bacteria and between bacteria and the immune system. By this mechanism, both pathogenic and nonpathogenic species of *A. baumannii* interact with prokaryotic and eukaryotic cells in their environment. In nonpathogenic bacteria, outer membrane vesicles (OMVs) sometimes play a protective role. They could just contribute to bacterial survival by reducing levels of toxic compounds or even by using vesicles as an offensive tactic to gain a growth advantage over other bacteria. In *A. baumannii*, OMVs are typically spherical, in the 50-200 nm size range, and composed of outer membrane proteins, lipopolysaccharides (LPSs), periplasmic proteins, phospholipids, DNA, and RNA (Figure 1) [22-23].

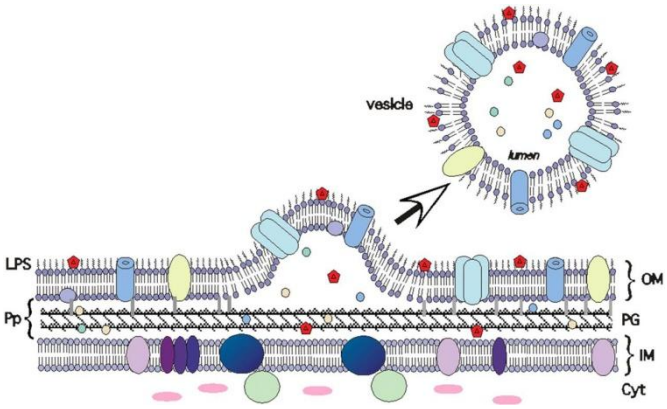

Figure 1: Model of vesicle biogenesis. Outer membrane (OM) vesicles are proteoliposomes consisting of OM phospholipids and LPS, a subset of OM proteins, and periplasmic proteins. Proteins and lipids of the inner membrane and cytosolic content are excluded from OM vesicles. Vesicles are likely to bud at sites where the links between the peptidoglycan and OM are infrequent, absent, or broken. (LPS) Lipopolysaccharide; (Pp) periplasm; (OM) outer membrane; (PG) peptidoglycan; (IM) inner membrane; (Cyt) cytosol. Taken from Kuehn et al, 2005 [23].

d) Production of β-lactamases. They are bacterial enzymes that degrade or modify the antibiotic before it can reach the appropriate PBP target. The structural similarity that β-lactamases share with PBPs allows these enzymes to hydrolyze and thereby inactivate the β-lactam antibiotic [24].

3. β-lactamases, antibiotic-modifying enzymes

β-lactamases probably evolved from PBPs, such as the peptidoglycan modifying DD-peptidases [24-25]. Structures and biochemical mechanisms of these proteins are conserved and are widely distributed among bacteria. Most likely in this case, evolutionary pressure has selected modifications that

allow the degradation of antibiotics. They are globular proteins that confer significant antibiotic resistance to their bacterial hosts through the irreversibly hydrolysis of the amide bond of the β-lactam ring resulting in biologically inactive products (Figure 2) [26-27].

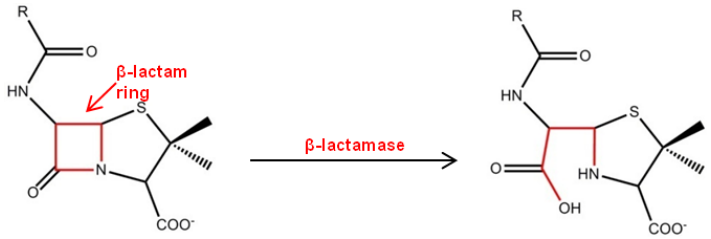

Figure 2: Hydrolysis of the essential four-member lactam ring of a β-lactam antibiotic by a β-lactamase.

These enzymes are especially important in Gram-negative bacteria as they constitute the major defense mechanism against β-lactam-based drugs [21]. Once expressed, β-lactamases are secreted into the periplasmic space where they maintain the local antibiotic concentration below the bactericidal threshold.

Their impact in the treatment of bacterial infections has already been huge, and their potential to challenge antimicrobial chemotherapy remains unexhausted [28].

β-lactamases were characterized by the Special Commission of the International Union of Biochemistry as enzymes acting on amide and cyclic amide bond [28]. Therefore, they have the classification number E.C 3.5.2.6 and received the systematic name of β-lactam hydrolases.

They can be classified based on their amino acid sequences into four classes (classes A-D; Ambler classification) or according to functional similarities based on their substrate and inhibitor profiles (Groups 1 -4; Bush-Jacoby-Medeiros) (Table 1)) [29] [30-33].

Table 1: β-lactamase classification systems

Ambler	Function; Inhibitors	Examples
Class A	Penicillinases; Clavulanic acid, sulbactam and tazobactam	TEMs, SHVs, CTX-Ms, SME-1
Class B	Metallo-β-lactamases; Zn(II) chelator agents	IMP-1, VIM-1, Ccr A, NDM-1
Class C	Cephalosporinases; Aztreonam	AmpCs, CMY-2, ACT-1
Class D	Oxacillinases; Clavulanic acid	OXA-1
Bush-Jacoby-Medeiros		
Group 1	Cephalosporinases	AmpCs, CMY-2, ACT-1, MIR-1
	hydrolyze extended-spectrum cepalosporins; clavulanate resistant	
Group 2	All clavulanic acid susceptible	
2ª	Penicillinase	PC1
2b	Broad-spectrum penicillinase	TEM-1, SHV-1, TEM-2
2be	ESBLs	SHV-2, TEM-10, CTX-Ms
2br	Inhibitor resistant	TEMs, IRTs TEM-30, TEM-31
2c	Carbenecillin hydrolyzing	PSE-1
2d	Oxacillin hydrolyzing	OXA-10, OXA-1
2e	Cephalosporinases inhibited by clavulanate	FEC-1
2f	Carbapenemases	KPC-1, SME-1
Group 3	Metallo-beta-lactamases	IMP-1, VIM-1, Ccr A
	hydrolyze imipenem, inhibited by EDTA, resistant to clavulanate	
Group 4	Miscellaneous	Penicillinase from *Pseudomonas cepacia*

4. Metallo β-lactamase superfamily

The metallo-β-lactamase fold represents a stable scaffold that has repeatedly been used during evolution to catalyze a diverse range of chemical reactions. Structurally, this diversity is achieved by varying the sequence and length of loops near the active site to accommodate different substrates. By combining the metallo-β-lactamase core domain with auxiliary substrate- , product- or cofactor-binding domains, the range of functions has been extended yet further.

In 1997, Neuwald *et al.* defined the metallo-β-lactamase superfamily [34] which includes most of the 6000 members distributed over three domains of living organism: *Eukarya, Archaea*, and *Bacteria*. This ubiquitous distribution suggests its functional importance and the ancient origin of the protein family.

In order to describe the functional and structural varieties of this superfamily, members were classified into 16 groups (Table 1), based on the biological functions [35], without reflecting any phylogenetic relationship. A new group has been recently described (number 0) including enzymes from *Pseudomonas* [36] and *Archaea* [37] of unknown function.

Table 2: Metallo-β-lactamase superfamily classification

Group		Description
1	Metallo β-lactamases	Class B of β-lactamases enzymes with one domain of around 250 amino acids, acting on carbon-nitrogen bonds to hydrolyze β-lactam antibiotics. Their production is regarded as a resistance mechanism against β-lactams [38] for eubacteria.
2	Glyoxalases II	Glyoxalases II present a N-terminal metallo-β-lactamase domain [39]. They catalyze the hydrolysis of the thioester of S-D-lactoglutathione to produce glutathione and D-lactic acid.
3	Flavoproteins and rubredoxin oxygen: oxidorreductase	They contain two distinct domains. One flavodoxin-like domain and a second metallo-β-lactamase domain. These enzymes carry out a terminal reaction in an unique oxygen scavenging pathway that enables the anaerobe to survive under aerobic conditions [40].
4	tRNase Z-family	Enzyme with an exosite which is not required for their phosphodiesterase activity but it is essential for pre-tRNA processing and tRNA binding.
5	Cyclases	Type II polyketide synthases are bifunctional enzymes, which shows both cyclase activity [41] and dehydrase activity [42-43].
6	Cleavage and polyadenylation specificity factor	Proteins involved in the processing of mRNA 3´-ends [44]. This group includes the 100-kDa [45] and 73-kDa [46] subunits of the mammalian cleavage and polyadenylation specific factor, and a subunit of the yeast polyadenylation factor I [47].
7	DNA cross-link repair	Enzymes involved in the repair of DNA interstrand crosslinks which induce lethal DNA damage. Upstream of the β-lactamase-like domain, they could have a DNA ligase I domain or a zinc finger domain with a very high diverse linker region connecting both domains [47-48]. In addition, members of this group share a region called β-CASP domain downstream of the metallo-β-lactamase domain [49].
8	DNA uptake for natural genetic transformation	Proteins involved in DNA uptake for natural genetic transformation [50-51]. They may cleave exogenous DNAs into small fragments to facilitate genetic transformation.
9	Choline binding Protein E	Known as teichoic acid phosphorylcholine esterase from *Streptococcus pneumoniae* [52]. This enzyme is involved in removing phosphorylcholine residues from the cell wall, such as teichoic acid and lipoteichoic acid [53].
10	*phnP* protein	Enzyme involved in the organophosphonate catabolism in bacteria [54].
11	CMP-N-acetylneuraminate monooxygenase	Key enzyme for N-glycolylneuraminic acid synthesis [55].
12	N-acyl homoserine lactone hydrolase	The quorum-quenching AHL lactonase (AiiA) from *B. thuringensis* [56].
13	Alkyl sulfatase	Identified as a determinant of sodium dodecyl sulfate biodegradation [57].
14	Carbofuran hydrolase	Enzyme composed of two repetitive MBL domains, capable of the hydrolysis of the insecticide carbofuran [58].

15	Methyl parathion hydrolase	This enzyme from *Plesiomonas* sp. M6 is able to degrade the insecticide, methyl parathion.
16	3´,5´-cyclic nucleotide phosphodiesterase	Low-affinity cAMP phosphodiesterase in *Saccharomyces cerevisiae* that controls the level of cAMP in yeast cells [59]. The same enzyme derived from *Vibrio fisherii* is present in the periplasm, and it is involved in the use of extracellular cAMP as a source of carbon, nitrogen and phosphorus for growth.
0	Unkown function	PqsE a "PQS response protein" from *Pseudomonas* [36] and ST1585 from *Sulfolobus tokodaii* [37].

The general common structure of these enzymes is based on the four-layer αβ/βα fold, composed by two central β-sheets with solvent-exposed α-helices (Figure 3). Each half of the molecule comprise a β-strand and two α-helices and they can be superposed by a 180° rotation around a central axis, suggesting that the structure might have arisen from the gene duplication [60]. In all known structures, the active site is located at the external edge of the β-sandwich.

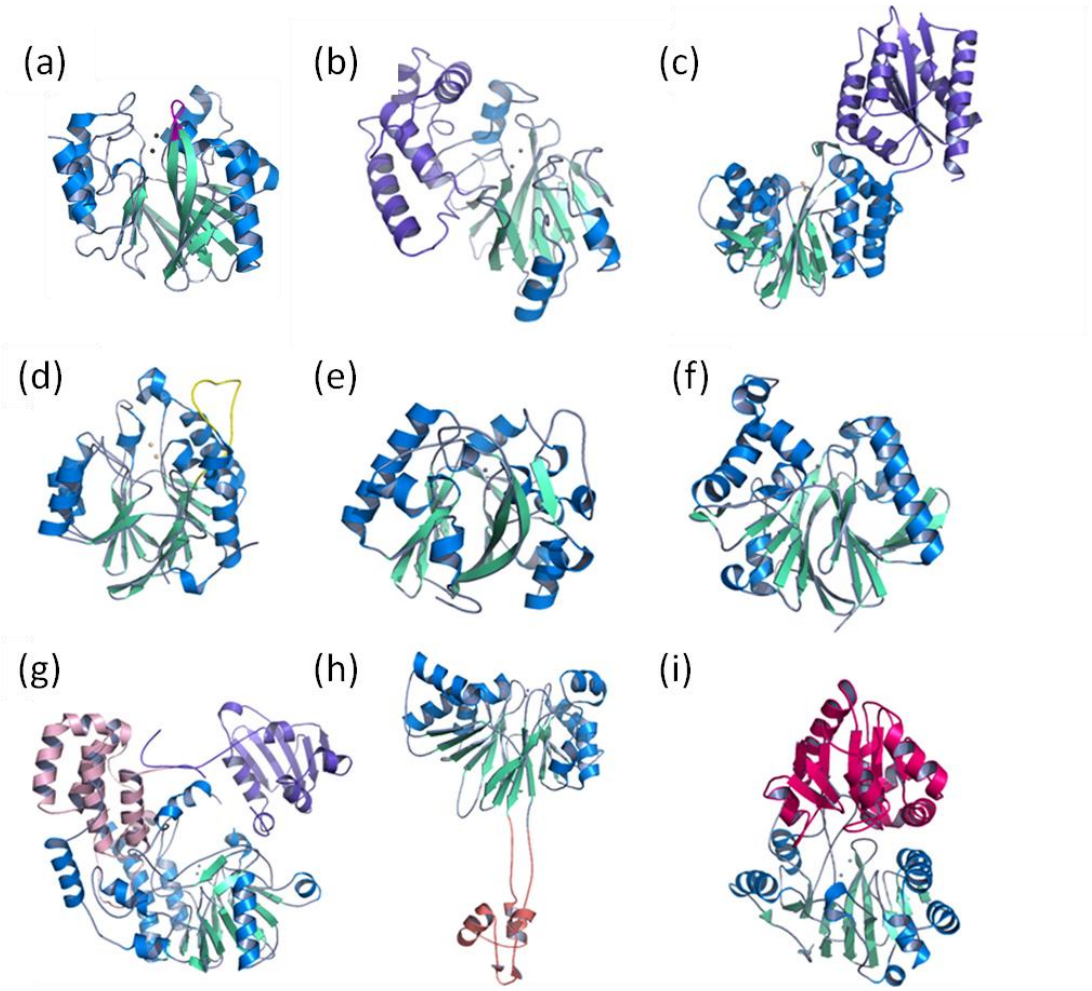

Figure 3: Metallo-β-lactamase superfamily overall structures. The metallo-β-lactamase domain is represented in blue (helices), green (strands) and grey (loops). Zinc and iron ions are shown as grey and beige spheres, respectively. (a) BcII, class B β-lactamase from *Bacillus cereus* (group 1) (b) Glyoxalase II (group 2) with the additional α-helical domain in violet, (c) ROO (group 3) with the additional flavodoxin-like domain in violet, (d) phosphorylcholine esterase (Pce) (group 9) domain of the virulence factor choline-binding protein E with the elongated loop lying on the top of the active site represented in yellow, (e) N-acyl homoserine lactone hydrolase (group 12) , (f) MPH monomer (group 15), (g) SdsA1 (group 13) monomer with the additional central dimerization domain in pink and C-terminal domain in violet, (h) ZiPD (group 4) monomer with the 50 amino acids exosite in salmon, (i) TTHA0252 with the β-CASP (group 6 and 7) domain in hotpink. (Taken from Bebrone et al, 2007 [61]).

Characteristic motif of the metallo-β-lactamase domain can be detected in the sequence of a large number of hypothetical genes in the GenBank [62]. They majority of these proteins have not been functionally or structurally characterized yet [61].

It should be noted that some members of this superfamily contain additional domains, suggesting that a functional diversification has occurred during evolution. The following figure is a schematic diagram showing different domains present in members of the superfamily (Figure 4).

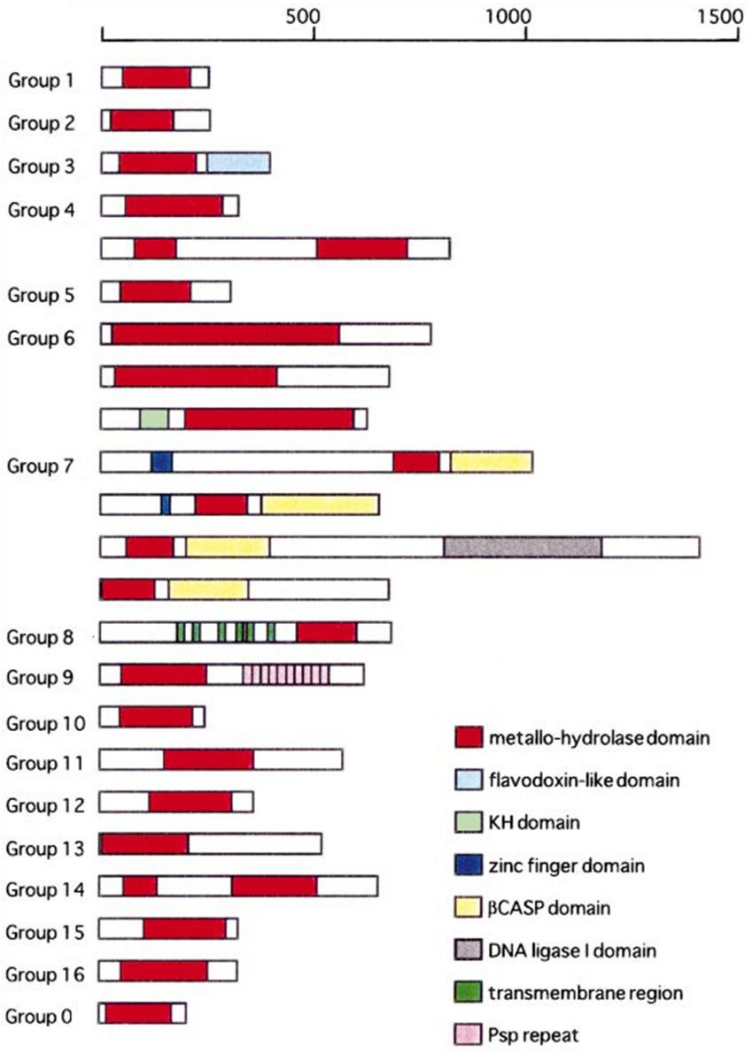

Figure 4: Schematic representation of the domain organization of the metallo-β-lactamase superfamily groups. Distinct domains are represented by colored boxes. The upper ruler indicates the number of amino acids Taken from Daiyasu [35].

A brief description of the groups where only residues from the metallo-β-lactamase domain are involved in its function will be presented.

4.1. GROUP 1: CLASS B β-LACTAMASES (METALLO-β-LACTAMASES, MBLs)

The MBLs (Ambler class B, Bush-Jacoby-Medeiros Group 3) are a diverse group of enzymes all sharing a common αβ/βα fold, in which the catalytic active site is located in an open cleft at the interface between the two domains and contain one or two Zn(II) ions (Figure 3a). Each metal site shares elements from both halves of the sandwich. The conserved His-X-His-X-Asp/His motif is the most characteristic signature of this superfamily and its integrity is maintained by a second shell that orients and polarizes the histidine ligands [63]. Zinc ions are 3.5-3.7 Å apart, with a metal-bridging water molecule positioned asymmetrically with respect to the binuclear metal center.

Many MBLs genes are present in environmental species constituting reservoirs of β-lactam resistance genes [44, 47-49]. MBLs are found as metal-free in vivo, binding zinc only in presence of the substrate [64]. Moreover, mutations of those amino acids present in the active site not belonging to the metal binding conserved motif dramatically reduce the substrate binding properties but retain the β-lactam-hydrolyzing activity [65-66]. Crowder et al. [63] have shown that the most important determinant in the broad substrate specificity of MBLs is the Zn (II) coordination shell that determines the productive interactions with the functional groups of the different substrates. Meanwhile, additional protein motifs, such as the conserved residues and the flexible loops, may play only minor roles in stabilizing the enzyme-substrate complex.

The MBLs classification task was complicated due to the low degree of sequence similarity among the different subclasses, but has been facilitated by the availability of X-ray structures, which allowed the identification of relevant secondary structure elements. Based on a combination of structural features, zinc affinities for the two binding sites and hydrolytic characteristics the MBLs are currently classified into three different lineages, identified as subclasses B1, B2, and B3 (Figure 5).

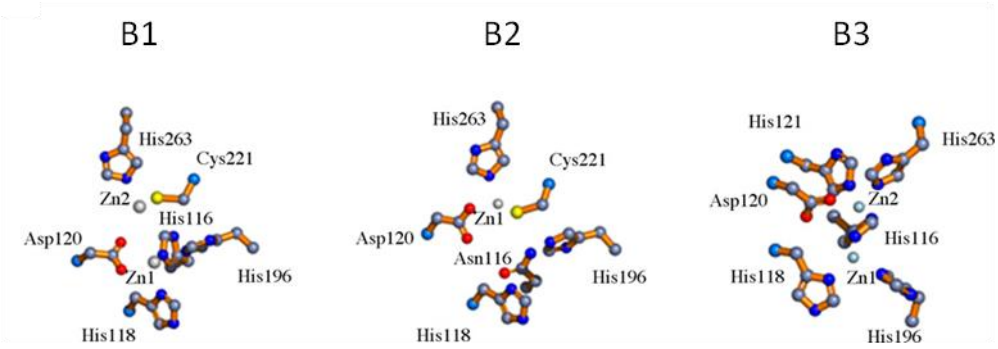

Figure 5: Active sites of the three subclasses. *B. cereus* BcII (subclass B1, left), *A. hydrophila* CphA (subclass B2, center), and *F. gormanii* Fez-1 (subclass B3, right). Zinc ions are rendered as gray spheres and residues are represented in ball-and-stick mode (nitrogen, blue; carbon, light blue; oxygen, red; and sulphur, yellow).

4.2. GROUP 2: GLIOXALASE II

The glyoxalase system consists of two distinct enzymes, glyoxalase I and glyoxalase II, that catalyse the conversion of toxic 2-oxoaldehydes into the corresponding 2-hydroxycarboxylic acids using glutathione (GSH) as a cofactor. This system has been found in many organisms ranging from bacteria to humans [67].

The substrate for glyoxalase I is the thiohemiacetal produced when GSH reacts non-enzymatically with a 2-oxoaldehyde (Figure 7). Glyoxalase I catalyses the isomerisation of thiohemiacetal to produce a thiolester of GSH and the corresponding 2-hydroxycarboxylic acid. Glyoxalase II then catalyses the hydrolysis of the thiolester generating 2-hydroxycarboxylic acid and free GSH. The primary physiological function of the glyoxalase system appears to be detoxication of methylglyoxal, a metabolic byproduct [68].

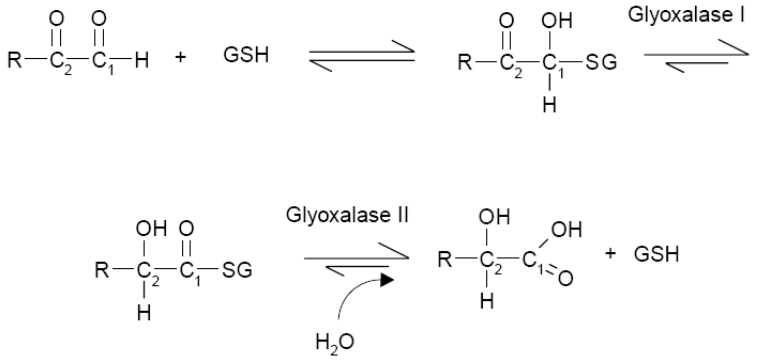

Figure 6: The glyoxalase system. GSH represents reduced glutathione (g-L-Glu-L-Cys-Gly). Glyoxalase II is a thiolesterase that catalyses the hydrolysis of S-D-lactoylglutathione to form glutathione and D-lactic acid. Taken from Cameron [39].

Glyoxalase II, GLX2, is made up by two domains (Figure 3b). The N-terminal domain shows the expected similarity with the MBLs, a four-layered β-sandwich containing a binuclear zinc-binding site. The smaller C-terminal domain is unique to this enzyme and consists mainly of α-helices situated at one edge of the main core. This typical domain is considered to be essential for substrate binding [39, 69].

The canonical GLX2 enzyme shares most of the key zinc binding residues of MBLs but in some members of this family structural differences can be observed. YcbL from *Salmonella enterica* serovar *Typhimurium* binds a single metal ion and has lost some recognition determinants for the glutathione substrate. Despite these changes, it has a robust GLX2 activity.

Moreover, several GLX2 have been characterized with different ratios of iron, zinc, and manganese ions in the active center displaying similar activities all the forms. This metal promiscuity can be explained by the presence of a conserved Asp residue acting as a second-shell ligand that increases the hardness of the metal binding site, therefore favoring iron uptake in GLX2.

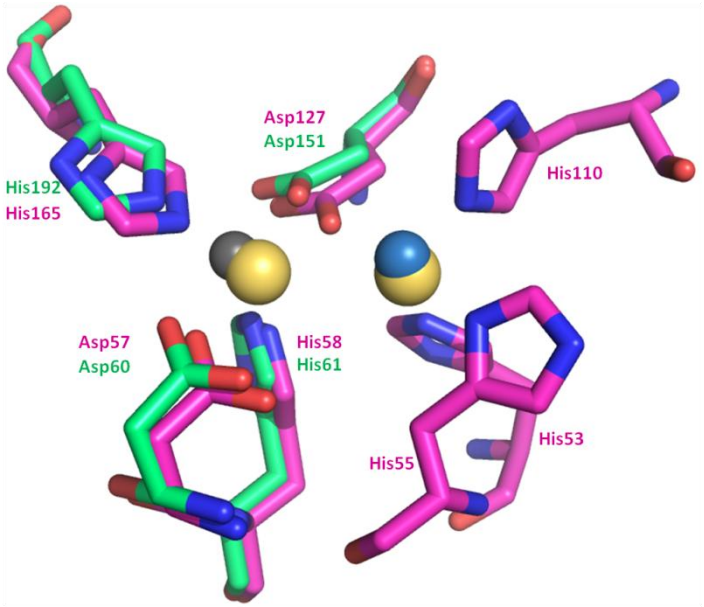

Figure 7: Comparison of the YcbL metal binding site (PDB code 2xf4) with the diion site in GLX2 (PDB code 2qed) both from *S. typhimurium*. This overlay indicates that the YcbL zinc site corresponds to the D-H-D-H site in GLX2. For GLX2, the second iron ion is bound at the H-H-H site, which in the case of YcbL is occupied by a water molecule. The carbon atoms of GLX2 are colored in pink and those of YcbL are in green. Iron ions are shown as yellow spheres and zinc ion as a grey sphere. Water molecule is rendered as a blue sphere.

4.3. GROUP 4: tRNASE Z-FAMILY

The elaC gene product from *Escherichia coli* (designated ZiPD [70], ecoZ [71], tRNase Z [72], or RNase BN [73]) is an enzyme with limited *in vivo* 3´ tRNA-processing endonuclease activity thats belongs to the tRNase Z family. It is not required for cell viability and its physiological role remains unknown. Although, the initial functional assignment in the literature was as the arylsulfatase/ElaC family, Vogel *et al.* [70] demonstrated that this was a wrong annotation. This enzyme has phosphodiesterase activity and is strongly dependent on the presence of zinc.

This protein is present as homodimer, with each monomer exhibiting the typical MBL fold (Figure 3h). Mono- or binuclear metal binding sites are identified in part by residues from the conserved sequence motif HXHXD/H [62]. Additional weakly conserved amino acids and water molecules complement the 4–6-fold Zn (II) coordination. An extra domain extending from the main body of the protein, called exosite, is necessary for tRNA recognition but is not required for the intrinsic phosphodiesterase activity or for dimerization [74]. It has been suggested that the exosite acts as a clamp to lock pre-tRNA into the correct

orientation for catalysis, using one monomer to bind the substrate and the other to catalyze hydrolysis with the homodimer capable of cleaving two pretRNA molecules at once [75].

4.4. GROUP 5: TYPE II POLYKETIDE SYNTHASES

Polyketides are a large group of secondary metabolites, exhibiting remarkable diversity in their structure and function [11]. They are synthesized by sequential reactions catalyzed by polyketide synthases (PKSs), large multienzyme protein complexes that contain many different enzyme active sites (acyltransferase, keto-syntase, methyltransferase…). The biosynthesis occurs in a stepwise manner from simple 2-, 3-, 4-carbon building blocks such as acetyl-CoA, propionyl CoA, butyryl-CoA and their activated derivatives, malonyl-, methylmalonyl- and ethylmalonyl-CoA.

The iterative Type II systems consist of complexes of mono-functional proteins exemplified by the PKS from *Streptomyces coelicolor* [42]. In these synthases, active sites are distributed among several smaller, typically monofunctional polypeptides. Type II synthases catalyze the formation of compounds that require aromatization and cyclization, but not extensive reduction or reduction/dehydration cycles. These PKSs are analogous to bacterial Fatty Acid Synthases and are involved in the biosynthesis of bacterial aromatic natural products such as actinorhodin, tetracenomycin and doxorubicin.

4.5. GROUP 10: PhnP PROTEIN

Phosphorus (P) is a nutrient of fundamental importance in the cell physiology of bacteria and achieve this, *E. coli* has evolved several gene systems whose products allow for P acquisition and assimilation from a variety of compounds [76]. These compounds participate in the high-affinity P inorganic transport, for uptake of glycerol-3-phosphate, for hydrolysis of phosphomonoesters, for passage of polyanions into the periplasm, and for the degradation of phosphonates (Pn).

Pn are similar to phosphate esters but have a direct carbon-phosphorus (C-P) bond instead of a carbon-oxygenphosphorus (C-O-P) bond. Unlike the C-O-P bond, the C-P bond can be extremely stable. All genes for phosphonate (Pn) utilization in *E. coli* are in a large cluster of 14 genes.

The *phnP* gene encodes for a phosphodiesterase that plays an important role within the bacterial CP-lyase pathway by recycling a “dead-end” intermediate, 5-phospho-α-D-ribosyl 1,2-cyclic phosphate, that is formed during organophosphonate catabolism. PhnP is a dimeric enzyme with a dinuclear active site that is typical for the MBL superfamily, as well as a structural zinc ion that is conserved in PhnP homologues [77]. Its *in vivo* substrate is 5-phospho-α-D-ribosyl 1,2-cyclic phosphate, which is a “dead-end” intermediate generated by the CP bond cleaving step in the CP-lyase pathway [78-79] PhnP regiospecifically converts this cyclic intermediate to α-D-ribosyl 1,5-bisphosphate, the putative initiator of the CP-lyase reaction.

4.6. GROUP 12: N-ACYL HOMOSERINE LACTONE HYDROLASE

Over 50 species of Gram-negative bacteria are known to produce N-acyl-L-homoserine lactones (AHLs) as signaling molecules used in quorum-sensing pathways that indirectly sense cell density and regulate communal behavior [80].

Quorum-sensing can be disrupted by enzymes that can hydrolyze either the amide [81] or the lactone [82] moiety of AHL-signaling molecules.

Currently, the best characterized quorum-quenching enzymes catalyze the opening of the AHL ring by hydrolyzing lactones to the corresponding γ-hydroxy acid. AiiA lactonases reduce AHL accumulation, alter swarming motility, and decrease the expression and secretion of numerous virulence factors. They are members of the MBL superfamily and contain two zinc ions in their active sites (Figure 3e).

4.7. GROUP 13: ALKYL SULFATASE

The first member of group III sulfatases is SdsA1 of *P. aeruginosa* [57], a secreted sodium dodecyl sulfate (SDS) hydrolase that allows the bacterium to use primary sulfates such as the detergent SDS as the sole carbon or sulfur source.

Homologues of SdsA1 are found in many pathogenic and some nonpathogenic bacteria. The crystal structure of SdsA1 reveals three distinct domains (Figure 3g). The N-terminal catalytic domain with a binuclear Zn cluster, the central dimerization domain ensures resistance to high concentrations of SDS, while the C-terminal domain provides a hydrophobic groove, presumably to recruit long aliphatic substrates [83].

4.8. GROUP 15: METHYL PARATHION HYDROLASE

The dimeric enzyme methyl parathion hydrolase isolated from *Pseudomonas* is a Zn(II)-containing enzyme (Figure 3f) that catalyzes the degradation of the organophosphate pesticide methyl parathion to produce p-nitrophenol and phosphate. Despite the lack of any sequence or structural homology with phosphotriesterase, there are obvious similarities in their metal-binding centers that suggest a common catalytic mechanism. An aromatic cluster formed by three amino acid residues oriented at the entrance to the catalytic center plays a key role in enzyme affinity to methyl parathion [84].

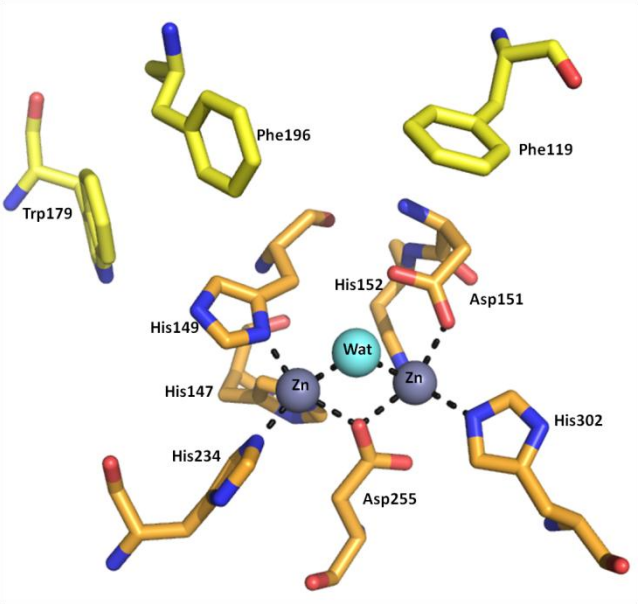

Figure 8: The methyl parathion hydrolase active site. The carbon atoms of the active site residues are colour in orange. Zinc ions are shown as grey spheres and the bridging water molecule is in blue. Residues forming an aromatic cluster at the entrance of the catalytic center (Phe119, Trp179, Phe196) are shown in yellow.

4.9. GROUP 16: 3´,5´-CYCLIC NUCLEOTIDE PHOSPHODIESTERASE

3',5'-Cyclic nucleotide phosphodiesterase (PDEs) converts 3',5'-cyclic nucleotides (e.g., 3',5'-cyclic AMP [cAMP] and 3',5'-cyclic GMP [cGMP]) to their corresponding 5'-nucleoside monophosphates.

The classification of all PDEs in classes I, II, and III shows evolutionary characteristics: All PDEs from higher eucaryotes (vertebrates, *Drosophila*, and *Caenorhabditis*) and only few from fungi belong to PDE class I, whereas PDE class II consists of several enzymes from fungi as lower eucaryotes and one from bacteria (the periplasmic PDE from *Vibrio fischeri* [85]). PDE class III consists, as far as is known, only of enzymes from procaryotes.

In general, PDEs enzymes show the typical secondary structure arrangement for members of the MBL superfamily but each class posses a defined motif in their active center. PDE from class I conserve a C-terminal catalytic domain of about 250 amino acids, which includes two invariant motifs of the formula $H(X)_3H(X)_{25–35}D/E$ containing the residues that form the two metal ion binding sites that usually are

occupied by Zn2+ and Mg2+/ Mn2+ [86-87]. One structure of the catalytic domain of human PDE4B2B was solved [86] providing detailed insight into the mechanism and structure of this active site.

Members of PDE class II share a conserved motif containing three histidine residues in the signature sequence HXHLDH which may be part of a metal ion binding site as it is known that the enzyme from *Vibrio fischeri* is Zn2+ dependent [88]. Further details about this active site are not yet known.

E. coli cpdA gene represents the first member of PDE class III does not have structural homologs in higher organisms. And although the structural and functional organization of its catalytic site is comparable to the rest of members of the dimetallophosphoesterases, any scheme for its catalytic site has been yet developed.

4.10. GROUP 0: PqsE ENZYME

P. aeruginosa integrates the biosynthesis of virulence factors and the generation of biofilms under the quorum sensing control [89], a signal transduction mechanism involving the production of small freely diffusible "autoinducer" molecules that activate their cognate regulatory proteins. The "Pseudomonas quinolone signal" (PQS) is produced from genes encoded in the pqs operon, which in addition to the biosynthetic enzymes PqsA-D contains a fifth gene, pqsE, that is not required for production of PQS but whose disruption leads to loss of signal transduction in several operon-dependent processes. PqsE was hence termed "PQS response protein", but its exact mechanism of action is unknown.

The overall fold of this protein resembles that of a typical MBL hallmarked by an αβ/βα sandwich core structure. In comparison to other members of this superfamily, the monomeric PqsE has two additional α-helices at its C-terminus that cover the active center and that might be involved in the control of substrate binding.

PqsE contains a redox-stable Fe(II)/Fe(III) center (Figure 9), in contrast with other proteins with the same first metal coordination sphere usually dependent on zinc binding. The number of functionally assigned proteins with two-iron centers within the superfamily is relatively small.

A copurified ligand assigned as benzoate was found in the crystal structure (PDB code 2q0i), its location coincides with the substrate binding site in related enzymes, and its carboxylate group participates in coordinating one of the two metal ions of the active center. It has been suggested that the regulatory effect of PqsE is mediated through a chorismate derived molecule, a central metabolite distributed into numerous tightly regulated pathways [90].

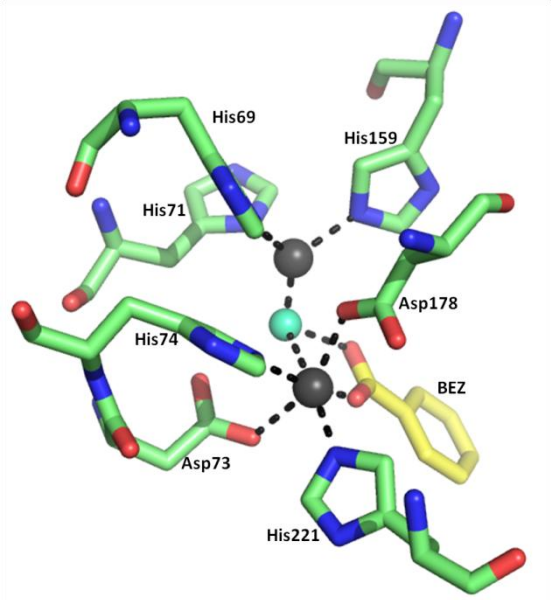

Figure 9: The iron binding site in PqsE with the copurified benzoate-shaped ligand (BEZ). The carbon atoms of the active site residues are colour in green. Iron ions are shown as black spheres and the bridging water molecule is in blue. The BEZ molecule is in yellow.

PqsE exerts its physiological role by acting as a hydrolase but also, by controlling the expression of important virulence factors like elastase and pyocyanin in *P. aeruginosa* and possibly also functions in a number of other pathogenic bacteria [91-93]. Furthermore, PqsE was found to slowly hydrolyze phosphodiesters including single- and double-stranded DNA as well as mRNA and also thioesters, but this activity seems too low to be meaningful.

OBJECTIVES

II. OBJECTIVES

Acinetobacter baumannii has emerged as an important oportunistic pathogen and therefore, represents one of the most challenging problems facing modern medicine. This microorganism has the ability to develop several resistance patterns starting from precursor resistance genes under the appropriate selection pressure. Among them are the class B β-lactamases. They are bacterial enzymes that show the canonical β-sandwich fold belonging to the metallo-β-lactamase superfamily, a wide group of enzymes with an important functional diversity.

The goal for the present study was to identify targets in *A. baumannii* associated with multidrug resistance. This approach was designed through an acurate analysis of the genome of this pathogen. Two genes, ABAYE3862 and ABAYE0164, encoding for two putative proteins belonging to the MBL superfamily were selected. Their secondary structure predictions suggested the canonical αββα fold typical for this superfamily, besides the presence on a non-canonical zinc binding motif in their amino acid sequences. We have called these proteins aMBL-1 and aMBL-2, respectively, from *acinetobacter Metallo*-Beta-Lactamase family.

With these premises, the following objectives were proposed for the present project:

- To describe an optimal protocol for the production and the purification of aMBL-1 and aMBL-2, for further functional and structural studies.
- To characterize aMBL-1 and aMBL-2 by biophysical and biochemical techniques, including enzymatic activity assays against β-lactam antibiotics and a broad collection of general chromogenic substrates.
- To determine the 3D-structures of aMBL-1 and aMBL-2 by X-ray crystallography and characterize the structural differences that could shed light on function.
- To classify these new members into the MBL superfamily according to their structure-function relationship with other related enzymes.

MATERIALS AND METHODS

II.MATERIALS AND METHODS

The development of efficient DNA sequencing methods has led to the achievement of the DNA sequence of entire genomes from different strains of *Acinetobacter baumannii*. In this study, the use of bioinformatics tools was essential for protein structure prediction from the target genes. Indeed, it provided the right design of different constructions for cloning. In a brief outline, the routine sequence analysis performed (used websites are indicated by brackets) is shown in next figure.

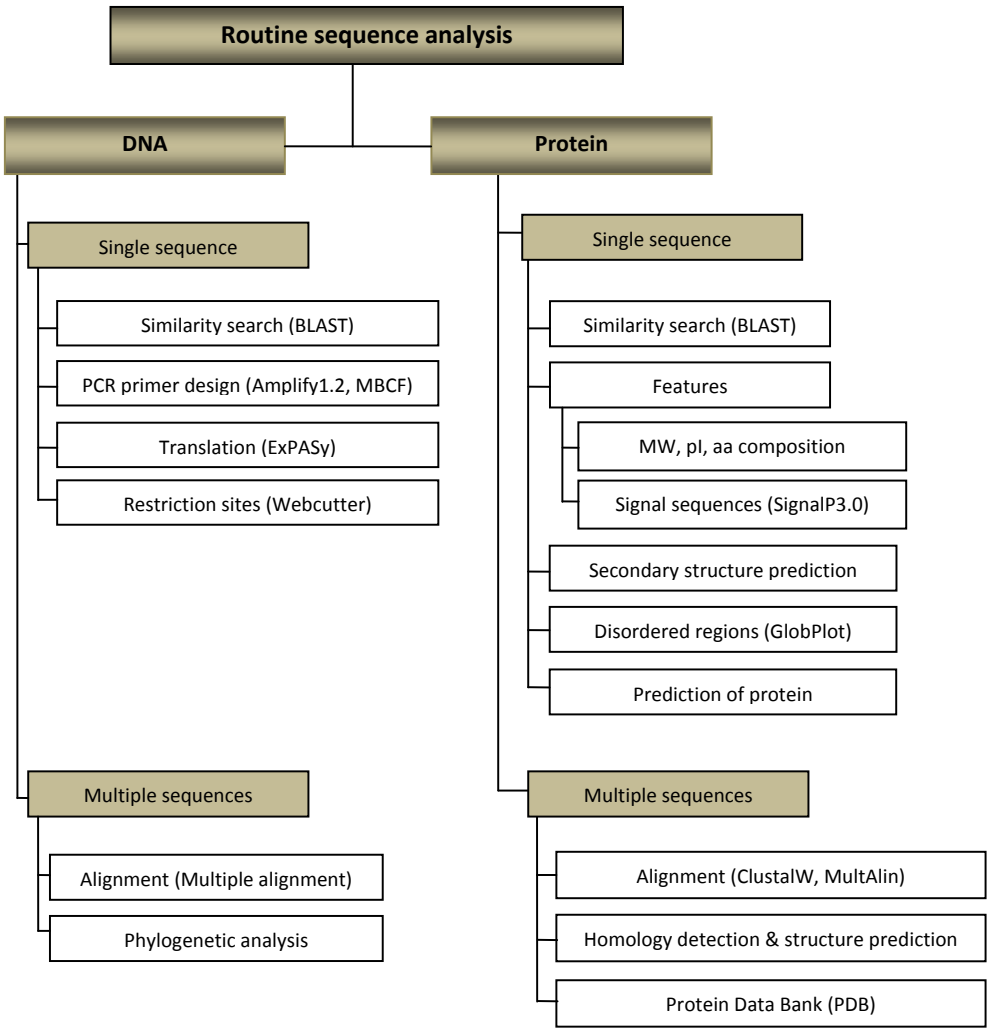

1. Cloning

Genomic DNA was isolated from *A. baumannii* strain AYE [94] kindly provided by Dr. Germán Bou from Hospital A Coruña (Spain). Enzymes, buffers and solutions used for DNA synthesis by polymerase chain reaction (PCR), DNA restriction assays, DNA ligation and recombination are shown in Table 3.

Table 3: Enzymes for DNA-subcloning

	Manufacturer	Reaction Conditions	1X Buffer Composition
***Bam*HI**	NEB	1X NEBuffer 3 supplemented with 100 µg/ml Bovine Serum Albumin (BSA)	50 mM Tris-HCl pH 7.9 @ 25°C, 100 mM NaCl, 10 mM $MgCl_2$, 1 mM Dithiothreitol (DTT)
***Eco*RI**	NEB	1X NEBuffer EcoRI	100 mM Tris-HCl pH 7.5 @ 25°C, 50 mM NaCl, 10 mM $MgCl_2$, 0.025 % Triton X-100
***Xba*I**	NEB	1X NEBuffer 4 supplemented with 100 µg/ml BSA	20 mM Tris-acetate pH 7.9 @ 25°C, 50 mM potassium acetate, 10 mM Magnesium Acetate, 1 mM DTT
***Nco*I**	NEB	1X NEBuffer 3	50 mM Tris-HCl pH 7.9 @ 25°C, 100 mM NaCl, 10 mM $MgCl_2$, 1 mM Dithiothreitol (DTT)
T4 DNA ligase	Fermentas	T4 DNA Ligase Buffer	40 mM Tris-HCl pH 7.8 at 25°C, 10 mM $MgCl_2$, 10 mM DTT, 0.5 mM ATP
***Dpn*I**	NEB	1X NEBuffer 4	20 mM Tris-acetate pH 7.9 @ 25°C, 50 mM potassium acetate, 10 mM Magnesium Acetate, 1 mM DTT

1.1. PCR AMPLIFICATION AND SUBCLONING

DNA for subcloning was amplified by PCR using specific primers individually designed for each sequence tag. The PCR primers used for the amplification of the different gene constructs were synthesized by Sigma-Aldrich. Primers were designed to a melting temperature T_m of more than 50° C. The melting temperature (T_m) for oligonucleotides were calculated by the following formula [95]:

$$T_m = 81.5 – 16.6 + 0.41(\%G+C) – 600/l$$

where: %G+C : G/C content in % and l : number of basepairs.

Primers were checked for self-complementary or two primers complementary and mispriming with the program AMPLIFY (Bill Engels, University of Wisconsin, Madison, USA) using default parameters. Detailed descriptions of the oligonucleotides used for the cloning of the two gene lactamase constructs are summarized in Table 4. Restriction enzyme sites added are underlined in the sequences. Stop codons (shown in bold) were positioned downstream of each restriction target. Additional residues were added 5' to the restriction sites to facilitate the complete restriction enzyme cleavage at the ends of PCR oligonucleotides. Two different plasmid vectors were used for the construction of the different gene constructs.

Table 4: Oligonucleotides for DNA-subcloning

Name	Sequence 5' - 3'	Residues cloned	Tm (° C)	Restriction enzyme	Description
Forward aMBL-1_pGEX	gatcGGATCCcaagatctgaaaattcagagttttctgg	27-288	66.3	*Bam*HI	For cloning into the pGEX-6P-2 vector
Reverse aMBL-1_pGEX	gatcGAATTC**tta**tggccactgcatttcacctttacc		66.3	*Eco*RI	
Forward aMBL-2_pGEX	gatcGGATCCatggggtttgaaaaaacaacatcacagatattatttgataatgg	full length, FL	68.1	*Bam*HI	
Reverse aMBL-2_pGEX	gatcGAATTC**tta**tgttggacagctaaaaatttgttctgtcattaaatctacacc		67.5	*Eco*RI	
Forward aMBL-1_pETRA	gatacTCTAGAatgaaattatttaaattatccgcttccgcacttgc	full length, FL	66.2	*Xba*I	For cloning into the pET-RA vector
Reverse aMBL-1_pETRA	gatcCCATGG**tta**tggccactgcatttcacc		66.8	*Nco*I	
Forward aMBL-1_pETRA	gatcTCTAGAatggggtttgaaaaaacaacatcacagatattatttgataatgg		66.5	*Xba*I	
Reverse aMBL-2_pETRA	gatcCCATGG**tta**tgttggacagctaaaaatttgttctgtcattaaatctacacc		68.7	*Nco*I	
Forward aMBL-2_DpnI	gcttcgcatcaggacccagatattatcacc	full length, FL	64.4	*Dpn*I	For mutagenesis PCR reaction
Reverse aMBL-2_DpnI	ggtgataatatctgggtcctgatgcgaagc		64.4	*Dpn*I	

- Different recognition sites were underlined in the primer sequences.
- In reverse primers design, one stop-translation codon (in bold in the sequences) was positioned downstream to the restriction target.
- Nucleotides corresponding to the site-directed mutation are highlighted in red.

The pGEX-6P-2 vector [96] was used to generate in frame fusion proteins with glutathione S-transferase (GST) at the N-terminal region. This tagging system allows for the removal of the GST carrier protein from the fusion protein by enzymatic cleavage with human rhinovirus 3C protease linked to GST [97] (see Figure 10).

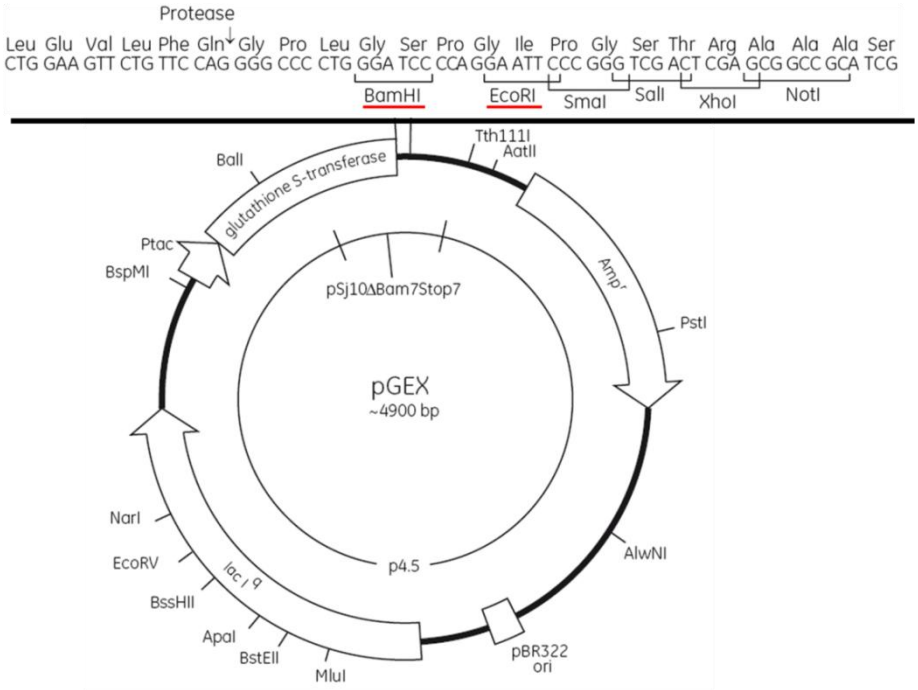

Gene sequence of aMBL-1:

BamHIcaagatctgaaaattcagagttttctggctaaaccagagcactttggtgtcacctcaaccttaatagaaggcgacaaagaagttttactggttaat
gcacaattctcaaaatctgaagcattacgtattgctgcaaatattctcgatagcggtaaaacattaaaaactattttcgtaagctatggcgacccggattatt
atttcggcttagatgtatttaaacagtatttcccgaatgtacagatcattgctacgccggaaacagtaaagcatattcaggatactcaagcgcttaaagtta
aatattgggggccacaaatgggtgcaaatgcacctagccaaattattgtgcctcaagcttacactgctaaaactttaaaacttgagaatgagtcaatcgag
attaaaggtaaaaaagagcttacttatttatgggttccttctgcaaaagcagtcgtgggggggtattccggtatcttcaggtattcatttatggatggcagata
cacctaaaaccagagatcgtgtggaagttattcaatctttagaaagcatcaaagcactacaacctaaaattgttgtacctgctcatatggttgagggagctc
cacaaggtttagatgctgttaacttttcgattaactatttaaatagttatgaaaaagcagctaaagcaactaaaaatgctactgagctgagcaagctcatgc
agaagcaatacccaacgcttcaaagtgttgatagcttagagctcggcgctaaagtggtaaaaggtgaaatgcagtggcca**taa****EcoRI**

Gene sequence of aMBL-2:

BamHIgggtttgaaaaaacaacatcacagatattatttgataatggcgtacacaaatgtattagttttaccagtttggtcaaaggggaaggcatacaagc
caatcaatttttaattattgatcatgagcgtgctgccgtgatcgacccaggtggtgatttgacctatgttccgttgacaatggaacttaataaatatacgcgcc
ttaaaaatcttgattatgtgatggcttcgcatcaggatccagatattatcacctcaatgccccgctggttagtctataccgatgctaaagtggtggcctcaaa
attatgggcacgtttttttacctcacttaaattcatcatttatgagtgagcgtatgaaagggaattgggaagaccgtctgattgagctgcctgatcgtggtcaa
gtgattcaattaggtgaatcgaaacttgtaatcattccagcgcattttctacattcggtgggtaattttcagttttatgatcccgttgctaaaatttttattttcgg
gcgatatgggagcatctattgtagatgatgcaagtcagcctctaaaagattttgatagccatgtgatgaaaatgaaagcttttcatcaacgttatatgtgttc
aaataaagttattcgcttatgggtcaacatgattcgtcagatggatattgaaatgattgtccctcagcacggtagtccatttattggtaaagagatgattaat
cagtttttagactggattgaaacattgccatgcggtgtagatttaatgacagaacaaatttttagctgtccaaca**taa****EcoRI**

Figure 10: Schematic representation of the pGEX6p-2 vector and the gene sequences corresponding to aMBL-1 and aMBL-2. The pGEX6p-2 vector (4900 bp) involves: a glutation-s-transferase tag followed by a 3C-protease target, a multiple cloning site, an ampicillin resistance gene and a lacI promotor.

However, this cloning procedure leaves five additional N-terminal residues (Gly, Pro, Leu, Gly and Ser). Since the gene encoding aMBL-2 also contained an internal *Bam*HI site at nucleotide position 249 (See Figure 10), this site had to be eliminated by site directed mutagenesis without changing the amino acid sequence. Site directed mutagenesis, removing the *Bam*HI restriction site was achieved by a two step PCR amplification procedure. First, blunt ending of PCR fragments was carried out using KOD Hot Start DNA Polymerase (Novagen) from genomic DNA and ligated into pCR®-Blunt vector following the protocol of The Zero Blunt® PCR Cloning Kit (Invitrogen). Then, a silent mutation (t – c at position 249) was introduced using the QuikChangeTM Site Directed Mutagenesis Kit (Stratagene).

For microbiological assays the pET-RA plasmid [98] was used. This plasmid carries a rifampicin resistance cassette, a gene coding for a green fluorescent protein (GFP), and the *A. baumannii* replication origin. It was used to express promoterless genes under control of the CTX-M14 β-lactamase gene promoter [98].

Unless indicated otherwise, the amplification reactions were conducted in 50 µl volumes, using 24 ng of template DNA, 0.25µM of each oligonucleotide primer, dNTPs (0.25 µM each), 1µM $MgSO_4$, 1x KOD Polymerase Buffer (see Table 3), and 1µL KOD Hot Start DNA Polymerase. DMSO (Sigma-Aldrich) was added to a final concentration of 2% to reduce secondary structures in the DNA and thus increase product yield. The samples were transferred to a preheated thermocycler block at 98° C.

PCR reactions were performed using an Eppendorf Mastercycler with the following program:

Step	Target size 1000 bp	Target size 4300 bp
1. Polymerase activation	95 °C for 2 min	95°C for 2 min
2. Denature	95 °C for 20 s	95°C for 30 s
3. Annealing	(Tm - 5 °C) for 10 s	(Tm - 5 °C) for 1 min
4. Extension	68 °C for 15 s	68°C for 9 min
5. Repeat steps 2–4	20–40 cycles	18 cycles
6. Final extension	68 °C for 10 min	68°C for 10 min

1.2. AGAROSE GEL ELECTROPHORESIS

All amplification products were analyzed using agarose gel electrophoresis. 5 µl of each PCR reaction was mixed with 1 µl of 6x DNA gel loading buffer Blue/Orange Loading Dye from Promega (0.4 % orange G, 0.03 % bromophenol blue, 0.03 % xylene cyanol FF, 15 % Ficoll® 400, 10mM Tris-HCl pH 7.5 and 50mM EDTA pH 8.0) and loaded in 1% agarose gel in 1x Tris-Acetate- Ethylenediaminetetraacetic acid (EDTA) buffer (TAE) (40 mM Tris-Acetate pH 8.3 and 1 mM EDTA). 30 mL gels were stained with 3 µL of 10,000x SYBR® Safe DNA gel stain. After loading, the electrophoresis was performed at 90 Volts using 1x TAE as running buffer. Fragment sizes were determined by comparison with molecular weight standards (1 kb DNA ladders, Fermentas). DNA bands were visualized under Ultraviolet (254 nm) light and analyzed using the Gel Doc EZ automated imaging system (BIO-RAD).

1.3. DNA PURIFICATION AND RESTRICTION ENZYME DIGESTION

PCR products were purified using the QIAquick PCR Purification Kit (Qiagen) while the vectors were purified using QIAquick Gel Extraction Kit (Qiagen). Both, amplified DNA fragments and vectors were digested with the appropriate restriction enzymes following the supplier´s instructions (NEB). For preparative purposes, 2 - 4 µg of DNA were digested with 10 - 15 units of restriction enzyme in a volume of 20 - 30 µl of the recommended NEB buffer. After incubation at 37° C for two hours samples were electrophoresed on an agarose gel as described for PCR amplification gel purification (see above).

1.4. DNA LIGATION

After digestion, in order to prevent recircularization, vectors were dephosphorylated with 1 µl of calf intestine phosphatase (CIP, 10U) (NEB) for 30 min at 37 °C [99]. Then, PCR and vector DNA concentrations were measured with a UV-visible spectrophotometer Nanodrop ND-1000 (BIO-RAD) from the Proteomics and Genomics Facilities at CIB.

For ligation, approximately 150 ng (3 µl) of purified vector DNA and different ratios of vector:insert DNA (1:1, 1:3, 1:5) were mixed in a final volume of 15 µl . Then 20 U/µg of T4 DNA Ligase (400 U/µL) (Fermentas) were added. Reactions were incubated overnight at 22 °C and then used for transformation. To confirm performance of the reaction a negative control without DNA insert was also set for trouble-shooting of the ligation reaction itself.

1.5. DNA MUTAGENESIS

The methylated, non-mutated and parental DNA from mutagenesis PCR was first digested, for 1 h at 37°C, with the restriction enzyme *Dpn*I (NEB) (20 U/µL). The mutagenic insert was confirmed in 1 % agarose gel by control digestion with *Bam*HI.

1.6. DNA TRANSFORMATION

The products of the ligations were confirmed by DNA sequencing (Secugen, CIB) and transformed into TG1 electrocompetent cells (Stratagene).

2. Protein expression and purification

For protein expression in LB media, the plasmids DNAs were transformed into the *E. coli* expression strain Rosetta (DE3) pLysS (Novagen) following the heat shock method.

2.1. EXPRESSION

A single colony of the Rosetta transformants was inoculated in 10 mL of LB medium containing 100 µg/mL ampicillin and 33 µg/mL chloramphenicol and incubated for 10-14 hours at 37 °C in a shaking incubator at 250 rpm. The overnight culture was inoculated into 1L of LB medium supplemented with the same antibiotics. The cultures were grown at 37 °C in a shaking air incubator at 250 rpm until the optical density at 600 nm (OD_{600nm}) reached 0.6 – 0.8. Protein expression was induced by addition of Isopropyl β-D-1-thiogalactopyranoside (IPTG) (Calbiochem) to the culture to a final concentration of 1 mM and then incubated for further 4 hours at 37 °C. Cell cultures were harvested by centrifugation (6000 xg, 20 min, 4 °C). Cell pellets were resuspended in 30 mL of lysis buffer (PBS buffer supplemented with 0.5 % Tween-20 (BIO-RAD)). The cells were sonicated in a Misonix S4000 Sonicator following a single sonication protocol:

1. Amplitude: 30; Time: 1 min 30 s; Intervals: 2 s ON, 1 s OFF.
2. Amplitude: 40; Time: 2 min; Intervals: 2 s ON, 1 s OFF.
3. Amplitude: 50; Time: 2 min; Intervals: 2 s ON, 1 s OFF.

Insoluble material was pelleted at 30000 rpm using a 60Ti rotor (Beckman) for 30 min at 4 °C and the supernatant was collected and filtered with a 0.45 µm syringe filter (Sartorius Stedim Biotech).

2.2. PROTEIN PURIFICATION OF GST-TAGGED PROTEINS

Before loading the supernatant containing the soluble GST-tagged proteins, a GST Trap HP 5 mL column (GE Healthcare-Amersham Biosciences) was connected to a single-channel peristaltic pump that was extensively washed with water and finally equilibrated with the PBS binding buffer supplemented with 1mM Dithiothreitol (DTT) (Sigma). After loading the sample, the column was washed with 30 mL of binding buffer to reduce non-specific binding of other proteins.

Bound proteins were then subjected to an on-column cleavage of the fusion GST protein with 200 µg of 3C protease with GST-tag [97]. For that, the binding buffer was changed to the cleavage buffer (50 mM Tris-HCl (Merck), 150 mM NaCl (Merck), 1 mM DTT (Sigma) and adjusted to pH 7.5). 3C protease was diluted in this buffer (5 mL total volume) and manually injected into the column. Following injection, the column was closed, sealed and incubated overnight at 4 °C.

The target protein was eluted from the column with 6 column volumes of the cleavage buffer. A final 10 column volumes wash with elution buffer (50 mM Tris-HCl and 10 mM L-glutathione reduced (GSH), adjusted to pH 8.0) was applied to complete elution of the GST-tag, the uncleaved protein and the GST-3C protease. The different elute batch fractions were analyzed by 15 % SDS-PAGE and pure fractions were concentrated by ultracentrifugation with AMICON ULTRA-15 10KDa (Millipore) for the next step of purification.

The concentrated fractions were then loaded into a HiPrep 16/60 Sephacryl S-100 HR prepacked column (GE Healthcare-Amersham Biosciences) connected to an ÄKTAprime™ (GE Healthcare-Amersham Biosciences). The column was equilibrated with cleavage buffer (50 mM Tris-HCl, 150 mM NaCl, 1 mM DTT adjusted to pH 7.5) at room temperature with a flow rate of 0.5 mL/min. The pooled peak fractions were

concentrated by ultracentrifugation to a final concentration of 20 mg/mL for the following crystallization trials.

2.3. EXPRESSION OF SEMET-LABELED PROTEINS

To solve macromolecular structures, phases can be determined experimentally using methods that rely on finding the positions of a few special anomalously scattering atoms. Protein expression in suitable host and growth media allows incorporation of Se-Met for SAD or MAD phasing experiments [100].

In this project, a method was used, which is based on the inhibition of the methionine biosynthesis, where a high incorporation of SeMet (> 90%) in the labeled protein can be observed. Inhibition of this metabolic pathway can be achieved by the use of high concentrations of Ile, Leu, Phe, Lys and Thr [101].

The procedure was as follows: From *E. coli* culture glycerol stocks: [pGEX6p-2-(aMBL-1)] and [pGEX6p-2-(aMBL-2)], were inoculated in 20 mL of LB medium containing 100 µg/mL ampicillin and 33 µg/mL chloramphenicol and incubated overnight at 37 °C in a shaking incubator. Then cells were inoculated into 1L of LB medium and grown until an OD_{600nm} of 0.6-0.8 was reached. Cells were then harvested at 6000 x g for 10 min at 4 °C. The pellet was washed with M9 medium and after centrifugation, resuspended in 1L of enriched M9 medium with the inhibitory cocktail of amino acids. SeMet (50 mg/1L) was added to the medium 15 min before induction.

The expression and protein purification were performed as described for the unlabeled protein. The degree of Se incorporation was checked by mass spectrometry [102].

Used medium composition (All the solutions were autoclaved except for the vitamin stock and glucose which should be sterile filtered using a 0.2 µm syringe filter):

- Enriched M9 medium (1X): M9 medium 1X, Ca/Mg solution, 10 mg/L B1 vitamin and 0.4 % Glucose.
- M9 medium (1X): 8.8 g/L Na2HPO4-2H2O; 3 g/L KH2PO4; 0.5 g/L NaCl y 1 g/L NH4Cl.
- Ca/Mg solution (for 1 L culture): 14.7 mg/L CaCl2-2H2O and 246 mg/L MgSO4-7H2O.
- Amino acids cocktail (for 1 L culture): 100 mg Lysine; 100 mg Threonine; 100 mg Phenylalanine; 50 mg Leucine; 50 mg Isoleucine and 50 mg Valine.

3. Biophysical and Biochemical Protein Characterization

3.1. ANALYTICAL GEL FILTRATION

Gel filtration provides a mean for the estimation of the molecular weight of proteins under study. It could be determined by comparing the retention volume parameter (Vr) with the values obtained for several known calibration standards.

The samples were injected onto a calibrated gel filtration column Sephadex200 10/300 GL column (GE Healthcare) at room temperature and with a flow rate of 0.5 mL/min. The column was previously equilibrated in buffer, containing 50 mM Tris-HCl, pH 7.5, 150 mM NaCl, 1 mM DTT. The peak fractions as detected at 280 nm were analyzed by SDS/PAGE.

Calibration of the Sephadex200 10/300 GL column was carried out using the following standards: Blue Dextran (2000 KDa), Ferritin (450 KDa), Catalase (240 KDa), Aldolase (158 KDa), Bovine Serum Albumin (BSA) (68 KDa), Albumin egg (45 KDa), Chymotrypsinogen A (25 KDa) and Cytochrome C (13 KDa). These lyophilized proteins were dissolved in the storage buffer of the target protein (50 mM Tris-HCl, pH 7.5, 150 mM NaCl, 1 mM DTT) at concentrations recommended by the manufacturer (Boehringer).

3.2. ANALYTICAL ULTRACENTRIFUGATION

These experiments were carried out by the Analytical Ultracentrifugation Facility at CIB (Madrid), on an Optima XL-I analytical ultracentrifuge (Beckman-Coulter) equipped with UV-visible absorbance

optics. Experiments were conducted at 20 °C using an AnTi50 rotor and Epon-charcoal standard double sector centerpieces (12 mm optical path length). Absorbance scans were taken at the appropriate wavelength (280–295 nm).

Two different experiments were carried out: Sedimentation velocity (SV) and sedimentation equilibrium (SE). Protein samples at 0.3, 0.9 and 2 mg/mL were pre-cleared at 16.000 x g beforehand.

SV experiments were performed at 48 krpm using 400 µL samples in buffer consisting of 50 mM Tris-HCl pH 7.5, 150 mM NaCl, 0.3 mM DTT. The resulting concentration gradient of material in the cell as a function of time and radial position was monitored by absorbance at 280 nm. Differential sedimentation coefficient distributions (c(s)) were calculated by least-squares boundary modeling of sedimentation velocity data using SedFit software (Version 12.1b) as described [103]. The calculated frictional ratios were used to transform the c(s) distribution into the corresponding molecular mass distribution [104-105].

For SE experiments, short column (85 µL) runs were carried out at multiple speeds (9 and 11 krpm) by taking absorbance scans at the different wavelengths depending on sample concentration: for AMBL-1 at 0.3 and 2 mg/mL (was to 280 nm) and at 0.9 mg/ml (290 nm), for AMBL-2 at 0.3 mg/ml (280 nm), at 0.9 mg/ml (295 nm) and 2 mg/ml (290 nm). After the equilibrium scans, a high-speed centrifugation run at 45 krpm was done to estimate the corresponding baseline offsets.

The weight-average buoyant molecular weight of both proteins was calculated using the Hetero-Analysis program (Version 1.1.44) [106]. The molecular weight of the proteins was determined from the experimental buoyant masses using the values of 0.7486 cm3/g and 1.00601 g/cm^3 as the partial specific volume and density, respectively.

3.3. MASS SPECTROMETRY

These experiments were performed on an Autoflex III MALDI-TOF-TOF instrument (Bruker Daltonics, Bremen, Germany) with a smartbeam laser by the Proteomic platform at INIBIC-CHUAC (A Coruña). The spectra were acquired using a laser power just above the ionization threshold. Samples were analyzed in the linear mode using positive ion detection with delayed extraction of ions.

Through matrix-assisted laser desorption ionization (MALDI) peptide mass fingerprinting, mass spectrometry in tandem (MS/MS analysis) and database searching were performed. Samples were analyzed in a MALDI-TOF/TOF instrument (4800 ABSciex) and 4000 series Explorer v.4.2 software was used to generate the spectra and peak list. Fragmentation spectra were acquired by selecting the 20 most abundant ions of each MALDI-TOF (time-of-flight mass spectrometer) peptide mass map (excluding trypsin autolytic peptides and other background ions). For database queries and protein identification, the monoisotopic peptide mass fingerprinting data obtained from MS and the amino acid sequence tag obtained from each peptide fragmentation in MS/MS analyses were used to search for protein candidates using ProteinPilot 3.0 software (ABSciex). The search for tandem MS spectra was performed in last release of Uniprot-Swisprot database for *Acinetobacter baumannii.*

Molecular weight analysis of derived protein (SeMet labeled protein) was carried out by MS-MALDI TOF at the Proteomics and Genomics Facilities at CIB (Madrid). Concentration protein was 10.8 mg/ml in 50mM Tris-HCl pH 7.5, 150mM NaCl and 1mM DTT buffer.

4. Protein crystallization

Macromolecular structure determination by X-rays relies on the availability of single crystals. Producing high-quality crystals is not trivial and the process can be long and frustrating because many parameters may have to be tested and optimized to find the optimal conditions. Crystallization of macromolecules is the major bottleneck in protein structure determination. There is no single way to efficiently predict under what specific conditions a protein will form single crystals. Crystallization is a multi-parametric process involving three main steps: nucleation, growth and cessation of growth. Crystal growth occurs from a supersaturated solution as a result of homogeneous nucleation. If the protein

concentration does not reach the required supersaturated state, no nucleation event occurs and the crystallization drop remains clear (see Figure 11).

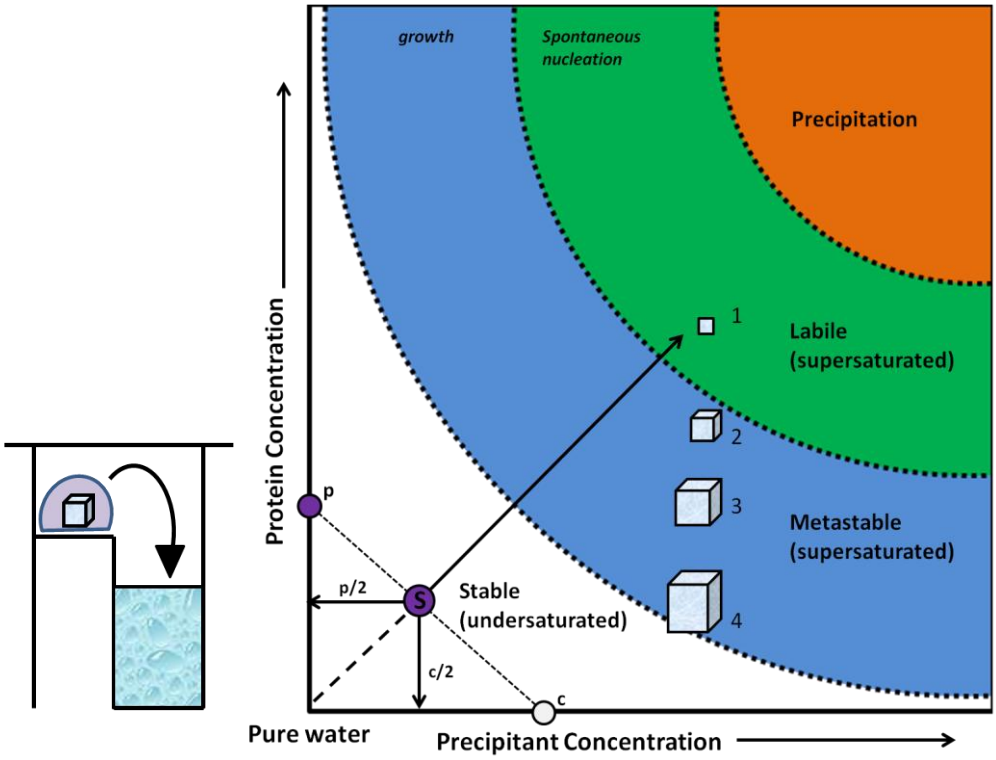

Figure 11: The sketch on the left illustrates the principle of the sitting-drop vapour diffusion technique. From the resulting starting drop (S, purple), water vapor diffuses into the precipitation cocktail reservoir and both protein and solute concentration in the drop increase. Once the region of spontaneous nucleation is reached (Labile), crystallization nuclei can form (1) and a crystal may start to grow. While the crystal grows (2,3), the solution depletes in protein, and a few of the initial crystals continue to grow large in the growth region of the phase diagram (Metastable). Once the crystals are in equilibrium with the saturated protein solution (4) they have reached their final size and growth stops. The diagram is divided into four zones: Stable: undersaturated where crystallization is not possible; Metastable: supersaturated where nuclei cannot form but crystals from seeds can grow; Labile: supersaturated where crystallization can occur; Precipitation.

Vapour diffusion is the most commonly employed technique for protein crystallization. The droplet containing a solution of the protein (buffered at a given pH), the precipitating agent and additives is allowed to equilibrate in a closed system with the reservoir solution at a higher precipitant concentration. To find the optimal crystallization conditions, hundreds to over a thousand of different solutions are screened in order to get a suitable condition that yield diffracting crystals.

The first approach to search for initial crystallization conditions was based on the sparse matrix formulation [107] using the sitting drop vapour diffusion technique with multidimensional commercial crystallization kits from Emerald Bioscience (Wizard I - II - III), Jena Bioscience (JBScreen 1 - 10) and Axygen Bioscience (CUSTOM I - V). Crystallization drops were prepared with a Cartesian HoneyBee X8 nanolitre-dispensing robot (Genomic Solutions) using the MRC 96-well sitting drop plates (Molecular Dimensions). The wells were filled up with 50 µL of the appropriate reservoir condition. Subsequently, the robot dispensed 200 nL of protein plus 200 nL of the reservoir solution. These experiments were performed at two different protein concentrations, aMBL-1: 30 mg/mL and 10 mg/mL; aMBL-2: 20 mg/mL and 10 mg/mL. The plates were sealed and stored at room temperature (22 °C).

The progress of the initial crystallization setups was monitored under a microscope (Leica) equipped with a polarization filter. If promising crystalline material is obtained during the initial screening, the next step was to fine-tune the initial crystallization setups in order to get the best conditions to obtain bigger and better diffracting crystals.

Optimization was carried out with a finer adjustment of the protein and/or precipitant concentrations, or changes in the pH. Furthermore, the rate at which supersaturation occurs may greatly

affect crystal growth. Because of this, we have increased the size of the droplets (1 µL of protein + 1 µL of reservoir condition) dispensed manually in the 24-well crystallization plates (Cryschem plates from Hampton). Crystals were grown at room temperature (22 °C).

In some cases, crystals were adhered to the well surface making it very difficult to manipulate. To avoid this phenomenon we added Silicon Oil (Molecular Dimensions) to the bottom of the well and left for drying at 70 °C for 20 minutes. Then, drops were set up.

4.1. CRYOGENIC PROTECTION OF THE CRYSTALS

Radiation damage in protein crystals upon exposure to high X-ray energies is mainly produced by free radicals. Among effects of radiation damage in crystals are the decreasing of the diffraction intensity and resolution. In some cases, the crystal completely stops diffracting. Cryocooling of protein crystals into liquid nitrogen is usually employed to reduce radiation damage during X-ray data collection [108].

Mounting a crystal for cryoprotection involves suspending it by surface tension in an appropriate cryobuffer within a nylon loop and then flash-cooling in liquid nitrogen. In flash-cooling the temperature of the crystal is lowered as rapidly as possible in order to suppress crystalline ice formation. The protein crystal resides into a clear, rigid and vitreous glass. However, ice will form in most solutions used for crystals grow. It is necessary to suppress this tendency by addition of cryoprotectants to the solutions. Cryoagents help to form vitrified water rather than crystalline ice. Although there is quite a choice of cryoprotectant compounds, we used polyethylene glycol 400 (PEG400) (see Table 5) at 5-20 % concentration as cryoagent.

5. Structure determination

5.1. X-RAY DIFFRACTION AND ANOMALOUS SCATTERING

X-ray crystallography is one of the most important techniques to get the structure of biological macromolecules at atomic resolution. The X-rays are scattered in all directions by the electrons contained in the protein crystal with a magnitude proportional to the number of scatterers.

In a diffraction experiment, the position and intensities of waves scattered from planes (denoted by hkl) in the crystal are measured. Intensity is proportional to the sum of the atomic numbers of all the atoms in the crystal structure and from each one it is calculated a scalar structure factor amplitude, F_h, but the phase angle, α_h of the complex structure factor, $\mathbf{F_h}$ is missing in this measurement ($\mathbf{F_h} = F_h \cdot \exp(i\alpha_h)$). This is the main obstacle in crystal structure analysis: the phase problem.

Supplying the phases for each reflection is possible through additional experimental phasing (MIR, MAD, SAD) or by molecular replacement when a structure or part of the structural model is known. Once the phase problem is solved, the electron density within the crystal can be derived from the diffraction pattern through a mathematical method, the Fourier transform, which allows to calculate the density at every point in the space:

$$\rho(\mathbf{x}) = \frac{1}{V} \sum_{h=-\infty}^{+\infty} F_h \cdot exp(i\alpha_h) \cdot \exp(-2\pi i(\mathbf{hx}))$$

In this final form of the density summation at a grid point x (x,y,z), the Fourier coefficients Fh·exp(i αh) explicitly include both the structure factor amplitude Fh and its associated phase, αh. As the physical source of diffraction was the scattering of X-ray photons by the electrons distributed around the atoms of the molecules into the crystal, this mathematical inversion of the diffraction process will deliver the electron density distribution within the unit cell of the crystal.

Resonance between beams of X-ray waves and electronic transitions from bound atomic orbital leads to a phenomenon known as anomalous scattering. If there are anomalous scatterers in the crystal it is possible to determine the crystal structure by the MAD (multiple anomalous dispersion) or SAD (single

anomalous dispersion) techniques. A typical MAD experiment is performed at three different wavelengths, at minimum f' and maximum f'' of the absorption edge of the anomalous scatterer, and at a distant wavelength (remote) where the anomalous signal is small. In some cases, data collected at one wavelength (SAD) were enough to determine phases. It could be demonstrated, that good phases estimates can be obtained by a more accurate measurement of diffraction intensities.

5.2. DATA COLLECTION

The data were collected using synchrotron radiation at the ESRF Structural Biology Beamlines (ID14-1 and ID14-4) using the MXCuBE ("MX Customised Beamline Environment") control module [108]. Frames were taken when the crystal was rotated around itself in small increments (1°) while it was exposed to X-rays and the reflections were recorded using a high-resolution 2D detector: the X-ray sensitive charge-coupled device (CCD) detector (ADSC). The appropiate wavelength was selected by a multilayer mirror. The structure determination was achieved by multiple wavelength anomalous dispersion (MAD) experiment for aMBL-1 [109] and by the single-wavelength anomalous diffraction (SAD) phasing method for aMBL-2 using energy tunable synchrotron radiation and selenomethionine (SeMet) recombinant proteins. The first step in designing the MAD or SAD experiments was to select specific wavelengths from the broad spectrum of energies that optimize the anomalous signal for the selected atom (K-absorption edge of Selenium). Since the scattering factors that determine these signals depend on the initially unknown chemical environment of the site and on the energy resolution of the beam, an X-ray fluorescence spectrum from the crystal across the heavy atom absorption edge is required. X-ray fluorescence spectra were measured by an XFlash fluorescence detector (Rontec) to provide the necessary information for finding f' and f'' at the appropiate wavelength for measuring anomalous diffraction data.

Complete MAD data sets were collected to 2.39 Å at three different wavelengths (see Table 5). To avoid radiation damage, the strategy was to collect under similar circumstances for a given reflection the appropiate Bijvoet mate. Thus, after each rotation increment, the ϕ-axis is rotated quickly by 180º for inverse-beam measurements [110]. This reduces potential difficulty in the later scaling stage, when reflections from temporally distant exposures need to be combined and merged into a single data set.

Table 5: Data collection

	aMBL-1					aMBL-2	
	Native Monoclinic	**Native Orthorhombic**	**Se_pk**	**Se_ip**	**Se_rm**	**Native**	**Se_pk**
X-ray source	ID14.4	ID14.1	ID14.4			ID14.4	
X-ray detector	Q315r ADSC CCD	Q210 ADSC CCD	Q315r ADSC CCD			Q315r ADSC CCD	
Wavelength (Å)	0.9770	0.9334	0.9794	0.9795	0.9770	0.9393	0.9794
Energy (keV)	12.69	13.28	12.66	12.66	12.69	13.2	12.66
Beam transmission (%)	41	100	74			5	41
Detector distance (mm)	255.31	166.52	290.7			340.91	376.4
Cryo condition	15 % PEG400	5 % PEG400	15 % PEG400			15 % PEG400	

5.3. DATA PROCESSING

After the data are collected, one needs to index each of the reflections in all the images by assigning each diffraction spot to its corresponding HKL value along with its intensity (or amplitude, F) and the error (σ). The indexing, processing and data reduction involves several steps that can be summarized as follows:

1. Visual inspection and preliminary analysis of the unprocessed diffraction images by MOSFLM [111], a graphical user interface for diffraction data.
2. Indexing of the diffraction data. This means identifying the dimensions of the unit cell.

3. Refinement of the crystal and detector parameters to minimize the discrepancies between observed and calculated spot positions in the data images.
4. Study of the crystal symmetry and determination of the space group.
5. Integration of the diffraction intensities; partial reflections extended over multiple frames are combined onto single reflections.
6. Crystal parameters post-refinement using all the data acquired.
7. Scale the indexed data set: equivalent reflections (symmetry related) will be merged and listed just once along with the error associated with all the equivalent measurements.

There are a variety of programs available to carry out the data processing. Native datasets were integrated and scaled using the programs MOSFLM [111] and SCALA from the CCP4 suite [112-114]. Structure factor amplitudes were derived from the intensities using the program TRUNCATE [115] from the CCP4 suite. Selenomethionine data were processed with the X-ray Detector Software (XDS) package [116]. The HKL files (an unmerged XDS ASCII file) obtained from the XDS package included the inferred crystal symmetry and metrics, and a list of corrected integrated intensities of the reflections. XSCALE [117] placed it on a common scale, optionally merged them into one or several sets of unique reflections and reported their completeness and the quality of the integrated intensities. XDSCONV [115] was used to convert these reflection data files into standard MTZ format, as it is required by various software packages for crystal structure determination.

5.4. CRYSTALLOGRAPHIC COMPUTING PROGRAMS AND MODEL REFINEMENT

For the rest of crystallographic analysis, it was very important to index accurately the space group which the crystals belong to. That was carried out by Pointless [118] and Reindex [112], both from the CCP4 suite for both kinds of datasets.

Heavy atom positions were determined using SHELX [119]. AutoSHARP (Statistical Heavy-Atom Refinement and Phasing) [120] was used for MAD/SAD experiments, using three wavelengths (peak, inflection and remote) for obtaining initial phases for aMBL-1 and on a single data set (peak wavelength) for aMBL-2.

In Phenix suite (Python-based Hierarchical ENvironment for Integrated Xtallography [121]), phases found by AutoSHARP were refined using *AutoSol*, rendering a first model for both new structures of this project. The resulting three-dimensional structures were extended through a combination of manual building in Coot [122] with alternating refinement cycles in the reciprocal space with the program *phenix.refine*.

The structure determination and refinement procedures might have biases that prone the structure models to systematic errors. Therefore, it is necessary to validate the quality of the final model. There are a variety of tools available that measure the deviation of the geometric and conformational parameters of the model from those of other small molecules or high-quality structures of other macromolecules. After the last refinement was completed, the validation of the final models was performed with all available tools in Coot and the derived software from the Molprobity web server [123].

The program PyMol [124] (http://www.pymol.org) was used for the 3D visualization and representation of both solved structures.

6. Functional assays

6.1. ENZYMATIC ACTIVITY

In accordance with studying the catalytic behavior of aMBL-1 and aMBL-2, enzymatic activity experiments were performed against a set of general chromogenic substrates.

By the application of general enzymatic screens and substrate profiling [125], glioxalase II, phosphatase, phosphodiesterase, esterase and thioesterase activities were tested for aMBL-1. Two different protein samples were used in these assays: aMBL-1 produced in LB medium and AMBL-1 produced in M9 medium. Both samples were applied at 30 mg/ml concentration and assays were performed at 37° C. The screens were inspected by eye or in a spectrophotometer.

Table 6: Activity tests with general chromogenic substrates

Enzyme Type	Reaction Mixture	OD (nm)
B-lactamase	1x PBS, 2mM BSA, 2 mM nitrocefin	490
Glioxalase II	100 mM MOPS (pH 7.2), 900 µM S-D-lactoylglutathione, 200 µM DTNB	412
Phosphatase	50 mM HEPES (pH 7.5), 5 mM Mg2+, 0.5 mM Mn2+, 4 mM pNPP	405
PDE/Nuclease	50 mM Tricine (pH 8.5), 5 mM Mg2+, 0.5 mM Mn2+, 0.83 mM bis-pNPP	405
Esterase	50 mM Tris (pH 8.0), 0.4% Triton X-100, 1 mM pNP-palmitate	410
Thioesterase	50 mM HEPES (pH 7.5), 0.4% Triton X-100, 1mM DTNB, 1mM palmitoyl-CoA	412

6.1.1. ANALYSIS OF β-LACTAMASE ACTIVITY

The hidrolytic activity of aMBL-2 protein was only tested against nitrocefin, a chromophoric cephalosporin without therapeutic utility but which undergoes intense spectroscopic changes upon hydrolysis. These kinetic experiments study the hydrolysis and accumulation of a ring opened, anionic intermediate of nitrocefin [126-127].

β-lactamases and β-lactam antibiotics interact to form a noncovalent enzyme-substrate complex. After β-lactam antibiotic is acylated, a strategically water molecule positioned on the active site hydrolyzes the acylated substrate [128]. In this manner, the β-lactamase is regenerated and can inactivate additional β-lactam molecules.

Competitive inhibition assays were carried out when a tested inhibitor competes with the substrate for the substrate binding site. For reversible inhibition, the reaction can be described as was shown above in equation 1, where S represents the (very) slowly hydrolyzed substrate. An equilibrium constant, Ki, can be calculated from the pre steady state rate constants, k-1/k1, and yields an estimate of affinity.

The 50% inhibitory concentration (IC50) measures the amount of inhibitor required to decrease enzyme activity to 50% of its uninhibited velocity. While an IC50 can reflect an inhibitor's affinity or kcat/kinact ratio, these parameters are not always congruent; e.g., an inhibitor can have a very poor "affinity" and acylate the enzyme slowly but still yield a low IC50 because of very low deacylation rates.

Kinetic experiments were performed with pure proteins (aMBL-1 at 33 mg/mL and aMBL-2 at 9 mg/mL) at 25 °C using a Nicolete Evolution 300 spectrophotometer (Thermo Electron Corporation, Waltham, MA) with quartz cuvettes of optical path lengths of 1 cm. The tests were each repeated three times in phosphate-buffered saline (PBS) with 20 µg/mL bovine serum albumin (BSA). The kinetic parameters kcat (Catalitic constant), Km (Michaelis-Menten constant), and kcat/Km (efficacy catalytic ratio) were studied for the antibiotics ampicillin, piperacillin, cefuroxime, ceftazidime and imipenem. The Km values were calculated as Ki values in competitive assays with nitrocefin (Oxoid Ltd.) as the substrate. The Vmax was calculated by considering an antibiotic concentration six times the Km and by use of the Michaelis-Menten equation, as previously described [129].

6.1.2. ANALYSIS OF GLIOXALASE II ACTIVITY

1 mL volumes of 100 mM 3-(N-morpholino)propanesulfonic acid (MOPS) pH 7.2 containing 900 µM S-D-lactoylglutathione (Sigma), 200 µM 5, 50 dithiobis-2-nitrobenzoate (DTNB) (Sigma) were monitored for the increase in absorbance at 412 nm for 1 min. Glutathione produced by the action of enzyme reduces the DTNB to form the yellow-colored product 5-thio-2-nitrobenzoic acid (TNB). The enzyme reactions were initiated by the addition of enzyme and were carried out at 37 °C.

6.1.3. ANALYSIS OF PHOSPHATASE ACTIVITY

First, appropriate serial dilutions of AMBL-1 samples were made with PA Assay Buffer (50 mM HEPES (pH 7.5), 5 mM Mg2+, 0.5 mM Mn2+). Then, 50µl diluted test samples were transferred in a 96-well plate as well as 50µl PA Assay Buffer without enzyme for blank wells. The reaction started with the addition of 50µl PA Substrate (50 mM HEPES (pH 7.5), 5 mM Mg2+, 0.5 mM Mn2+, 4 mM p-nitrophenyl phosphate (pNPP)) to each well. After 10-30 minutes of incubation at 37 °C, 50 µl Stop Solution (3M NaOH) was added to each well to stop the reaction. The phosphatases remove the phosphate group to generate p-nitrophenol, which is deprotonated under alkaline conditions to produce p-nitrophenolate that has strong absorption at 405nm.

6.1.4. ANALYSIS OF PHOSPHODIESTERASE ACTIVITY

Experiments were performed in 50 mM Tricine, pH 8.5, and 2 mM MnCl2. Bis-pNPP hydrolysis was determined following the absorption of p-nitrophenolate at 405 nm.

Other potential phosphodiesterase substrates as double stranded DNA (λ DNA), single stranded DNA (M13mp8 phage DNA) and lineal 1000 bp DNA were tested by agarose gel electrophoresis stained with ethidium bromide. Negative controls of DNA degradation included incubation with reaction buffer supplemented with EDTA or ATP.

6.1.5. ANALYSIS OF ESTERASE ACTIVITY

A stock solutions of 100–250 mM p-nitrophenyl ester was prepared in CH_2Cl_2. Immediately prior to initiation of the assay, 20 µL of the stock was diluted into 10 mL of buffer containing 20 mM Tris–HCl (pH 8.0), 150 mM NaCl, and 0.01% Triton X-100 while vortexing. Protein samples of up to 20 µL are incubated with 0.2 mL substrate solution in 96-well clear microtiter plates. During the incubation period at 37 °C (up to 30 min), the liberation of p-nitrophenol is measured as the increase in absorbance at 410 nm in an ultraviolet–visible spectrophotometer against a blank without enzyme.

6.1.6. ANALYSIS OF THIOESTERASE ACTIVITY

The acyl-CoA thioesterase activity of purified AMBL-1 was measured using DTNB. Hydrolysis of acyl-CoA molecules leads to a rapid reaction between DTNB and CoA to form TNB, which absorbs light at 412 nm. Reactions were carried out in 200 µl volumes within the wells of 96-well Nunc plates (Fisher Scientific). The substrate palmitoyl-CoA was prepared as 10 mM stock solutions in water.

Appropriate volumes were mixed with reaction buffer to achieve final concentrations in 50 mM HEPES (pH 7.5), 0.4% Triton X-100 and 1mM DTNB. Then, 33 mg of AMBL-1 were added to initiate acyl-CoA hydrolysis. Plates were immediately loaded into a temperature-controlled SpectraMax M5 microplate reader (Molecular Devices), mixed for 5 s and absorbance readings at 412 nm were taken at 1 min intervals for up to 60 min. Incubation without substrate served as a control to determine background degradation of DTNB.

6.2. ANTIBIOTIC SUSCEPTIBILITY TEST

Antibiotic susceptibility experiments are used to confirm bacteria resistance against antibiotics and to determine the MIC (Minimum Inhibitory Concentration) values of a strain, establishing the lowest concentration of an antibiotic inhibiting visible growth of bacteria.

These quantitative methods were executed with two different strains: *A. baumannii* ATCC 17978 and *Acinetobacter sp.* strain ADP1 both harboring the proteins under study subcloned in the pETRA vector. As a negative control an empty pETRA vector was used.

MICs breakpoints of several antibiotics were determine by two different methods: standard disk diffusion method (Becton, Dickinson and Company) and epsilometer test (E-test) (AB Biodisk) on Mueller-Hinton agar at 37 °C following the manufacturer´s criteria. After *Acinetobacter* bacteria suspensions were adjusted to a turbidity equivalent to a 0.5 McFarland standard, approximately $5x10^5$ CFU/mL of these suspensions was inoculated onto agar plates using sterile cotton-tipped swabs to produce a confluent lawn of bacterial growth. When the inoculum on the plates was dry, some antibiotic disks were distributed following the disk diffusion method to determine the zone diameter breakpoints. On the other hand,

some of these inoculated plates were used to determine MIC breakpoints by Etest, which are thin plastic strips covered with a continuous antimicrobial gradient of an antibiotic on one side and a number scale on the other. When they are placed in an inoculated plate, the antibiotic is immediately released into the agar forming a stable continuous gradient of antibiotic concentrations underneath the strip. After 16-18 h of incubation at 37°C, bacterial growth has become visible and an ellipse formed inhibition zone is seen centered along the strip. MIC value is read from the scale (μg/ml) where the ellipse edge intersects the strip. MIC measures are accurate and reproducible.

The different used disks and Etest were: 10 μg ampicillin (AM10), 10 μg penicillin (P10), 100 μg piperacillin (PIP_{100}), 110 μg piperacillin-tazobactam (TZP_{110}), 30 μg cephalothin (CF_{30}), 30 μg cefoxitin (FOX_{30}), 30 μg cefotaxime (CTX_{30}), 30 μg ceftazidime (CAZ_{30}), 30 μg cefepime (FEP_{30}), 10 μg meropenem (MEM_{10}), 10 μg imipenem (IMP_{10}), 30 μg aztreonam (ATM_{30}), 30 μg amoxicillin-clavulanic acid (AMC_{30}) and 10 μg colistin (CL10). The MIC breakpoints and the zone diameter breakpoints of each antimicrobial agent were determined according to the recommendations of Clinical and Laboratory Standards Institute [130].

These preliminary MICs values obtained from on plates methods were tuned by broth microdilution method [130]. The corresponded *Acinetobacter* inoculums of $5x10^5$ CFU/mL were incubated for 24 to 48 h at 37 °C in LB medium. As the end point, the lowest concentration of the compound that completely inhibited growth was recorded as the MIC.

The used antibiotics for this assay were purchased from Sigma-Aldrich: ampicillin, penicillin, piperacillin, cephalothin, cefoxitin, cefuroxime and aztreonam. Cefepime was obtained from Sigma-Genosys Ltd. (United Kingdom) and imipenem was obtained from Merck Sharp and Dohme (Madrid, Spain).

The hydrolytic activity against antibiotics was also determined by an adaptation of the Masuda method. Over a Mueller-Hinton agar plate, an inoculum of *E. coli* DH5α cells/ml 0.5 McFarland was extended and several disks were placed around an ampicillin disk in the middle (AM10, 10μg). Different disks contain: OXA (45μg), (+) control (enzyme with well-known β-lactamase activity), BSA (45μg), (-) control (enzyme without β-lactamase activity) and the target proteins (45 μg). It could be observed that the halo of growth around the ampicillin disk was deformed by bacteria which could incorporate the protein with hydrolytic activity.

6.2.1 QUANTITATIVE RT-PCR

To confirm increased expression of the target genes, the original *A. baumannii* ATCC 17978 strain as well as *A. baumannii* ATCC 17978 with different constructions in pE-TRA vector were used in a reverse-transcriptase PCR (RT–PCR) to determine the over-expression of target genes relative to the house-keeping gene gyrB from *A. baumannii* ATCC 17978 which codes for two of the four subunits of the bacterial DNA gyrase enzyme. Total RNA was extracted by High Pure RNA Isolation kit (ROCHE) according to the manufacturer's instructions. RNA samples were tested by performing PCR without Reverse Transcriptase confirmed the absence of DNA. The concentration and integrity of the RNA were determined by measuring the OD260/230 and OD260/280 as well as by 1% agarose gel electrophoresis. A total of 50 ng of RNA was used in the target gene studies.

Real-time RT-PCR analysis of genes expression was performed for aMBL-1 and aMBL-2 and gyrB (housekeeping) for triplicate using specific internal oligonucleotide primers and Taqman probe UPL (Universal ProbeLibrary), ROCHE. The concentrations of them were adjusted to give amplification efficiencies of 90 to 110%.

Gene expression was normalized versus that of gyrB in the same strain and calibrated relative to ATCC 17978 *A.baumannii*, which was assigned a value of 1.0.

Primers for RT-PCR:

aMBL-1 (full length): Probe **gatggcag**

Forward: 5’- gggtattccggtatcttcagg- 3´

Reverse: 5’- ttccacacgatctctggtttt- 3´

aMBL-2 (full length): Probe **gctgcctg**

Forward: 5’- gaattgggaagaccgtctga - 3´

Reverse: 5’- tcacctaattgaatcacttgacca - 3´

Housekeeping gene (gyrB) **tggtggaa**

Forward: 5’- cattcttcttccgtcaaatgc- 3´

Reverse: 5’- tattgcacagccacctttgt- 3´

RESULTS

III. RESULTS

CHAPTER 1: aMBL-1

1. Sequence analysis

In an attempt to solve the structure and to understand the function of this uncharacterized protein found in the genome of *Acinetobacter baumannii*, bioinformatics tools were used to explore the presence of conserved domains in the sequence as well as for protein family classification.

3.1.1. SEQUENCE ANALYSIS

The *ABAYE3862* gene encodes a protein, aMBL-1 (http://www.ncbi.nlm.nih.gov/gene/6002746) classified by the InterPro web server [131] belonging to the metallo-β-lactamase superfamily, containing a β-lactamase domain and a signal peptide in its sequence. Also, the program HHpred [132] found a number of related proteins, of which the eight closest homologues proteins shared the typical αβ/βα metallo-β-lactamase fold:

2yz3 β-lactamase VIM-2 from *Pseudomonas aeruginosa* [133]; (E-value 1.3E-32)

2fhx β-lactamase SPM-1 from *Pseudomonas aeruginosa* [134]; (E-value 2.3E-30)

2vw8 Quinolone protein from *Pseudomonas aeruginosa* PAO1 [135]; (E-value 2.7E-30)

3q6x β-lactamase NDM-1 from *Klebsiella pneumoniae* [136]; (E-value 7E-31)

2cfu SdsA1-hydrolase from *Pseudomonas aeruginosa* [83]; (E-value 7E-30)

2q9u A-type flavoprotein from *Giardia intestinalis* [137]; (E-value 1E-26)

1xm8 Glyoxalase II from *Arabidopsis thaliana* [138]; (E-value 1.1E-26)

1e5d Rubredoxin from *Desulfovibrio gigas* [139]; (E-value 3.9E-26)

A BLAST search (Basic Local Alignment Search Tool [140]) found several highly similar protein sequences in the non-redundant (NR) database. Thus, aMBL-1 was found to be similar to several Zn-dependent hydrolases of the metallo-β-lactamase superfamily from *Acinetobacter sp.*, and with proteins from other bacterial species:

Accession	Description	Query coverage (%)	E value	Max ident (%)
YP_001715574.1	**Hypothetical protein ABAYE3862 [Acinetobacter baumannii AYE]**	100	0.0	100
YP_002317466.1	**Metallo-β-lactamase family protein [Acinetobacter baumannii AB0057]**	100	0.0	99
YP_001085962.1	Putative signal peptide [Acinetobacter baumannii ATCC 17978]	100	0.0	99
ZP_05830273.1	Metallo-β-lactamase superfamily protein [Acinetobacter baumannii ATCC 19606]	100	0.0	99
YP_001844693.1	Zn-dependent hydrolase [Acinetobacter baumannii ACICU]	100	0.0	99
ADY82986.1	Metallo-β-lactamase superfamily protein [Acinetobacter calcoaceticus PHEA-2]	100	0.0	99
YP_048103.1	Conserved hypothetical protein; putative signal peptide [Acinetobacter sp. ADP1]	96	6,00E-158	77
NP_248747.1	Unnamed protein product [Pseudomonas aeruginosa PAO1]	86	2e-74	45
ZP_05878299.1	Metallo-β-lactamase family protein [Vibrio furnissii CIP 102972]	96	1,00E-75	41

To define ordered regions that are usually more prone to crystallization, secondary structure elements were predicted by PSIPRED [141] and disordered regions by GlobPlot [142]. aMBL-1 was defined as a globular protein with a predicted signal sequence at the N-terminal region. Analysis of the protein sequence with LipoP server [143] suggested a signal peptide with a cleavage site between Ala25 and Gln26.

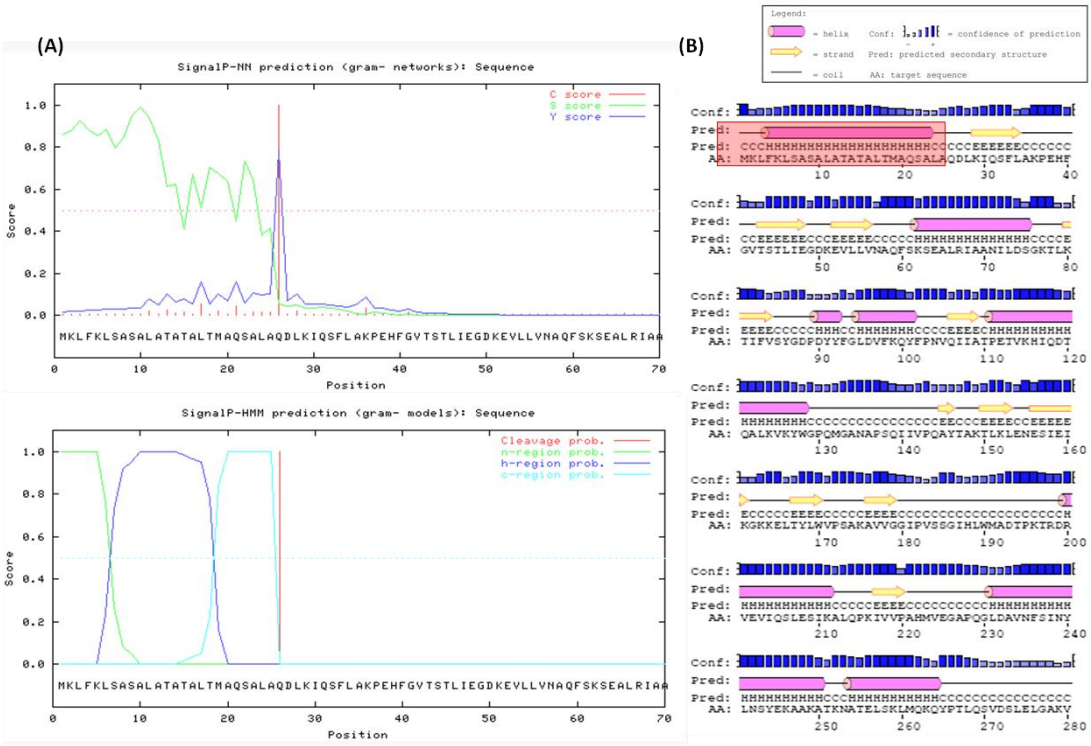

Figure 12: Analysis of the aMBL-1 amino acids sequence. (A) Analysis of the presence of a signal peptide in the protein sequence of aMBL-1 (M1-A25) using the LipoP server. (B) Secondary structure prediction of aMBL-1 by the PSIPRED server (pink cylinders represent α-helix structure (H), yellow arrows are β-sheets (E) and the black line shows the coil region (C)).

Crystallization propensity predictions based on the peptide sequence were performed with XtalPred [144]. According to statistical analysis and additional protein sequence properties (sequence length, isoelectric point, percentage of coil structure…), this protein showed a higher tendency to crystallize once the predicted signal peptide was removed.

In conclusion, aMBL-1 is a globular protein with a predicted αβ/βα fold of the metallo-β-lactamase superfamily. It is highly conserved among different strains of the *Acinetobacter sp.*, and it is also conserved in other bacterial species.

2. Cloning

The gene encoding aMBL-1 was amplified by PCR from the genome of *Acinetobacter baumannii* strain AYE using the primers designed on the basis of the nucleotide sequence (see Materials and Methods). One step PCR subcloning technique allowed the insertion of the aMBL-1 coding sequence into the bacterial plasmid expression vector pGEX-6p-2 between the *Bam*HI and *Eco*RI restriction sites. This vector expresses the coding sequence for aMBL-1 (amino acids from Gln26 to Pro288) with an N-terminal GST fusion-tag and a 3C-protease cleavage site between them. This cloning strategy leaves five extra residues at the N-terminus of aMBL-1 after removing the GST-tag (GPLGS). The fused protein (GST-aMBL-1 [26-288]) has a calculated molecular weight (MW) of~56 KDa.

3. Protein expression and purification

3.1. PROTEIN EXPRESSION

E. coli strain Rosetta (DE3) pLysS was used for small- and large-scale expression of aMBL-1. The experiment was carried out as described in Materials and Methods. In order to check the expression level

and the soluble fraction of the protein, after cell lysis and centrifugation, pellet and supernatant samples were loaded on 15% SDS polyacrylamide gels (Figure 13). The supernatants showed an overexpressed band with approximate, the same MW as the GST-aMBL-1 fusion protein.

3.2. PROTEIN PURIFICATION

aMBL-1 was purified following the protocol described in Materials and Methods. Briefly, after sonication and centrifugation, the soluble fraction was loaded onto a GST-HiTrap column followed by on-column cleavage of GST tag with 3C-protease, overnight at 4 °C with a yield of approximately 95%. Then, the target protein (~30 KDa) was eluted with the cleavage buffer. The GST-tag, that remained bound to the column, was extracted from the column with the elution buffer.

Further purification of the sample was carried out through a size exclusion chromatography step (Sephacryl S-100). The second elution peak (lanes 11 to 13) of the chromatogram showed a very pure protein as could be seen by SDS PAGE (Figure 13). These fractions were treated separately and used for the crystallization experiments.

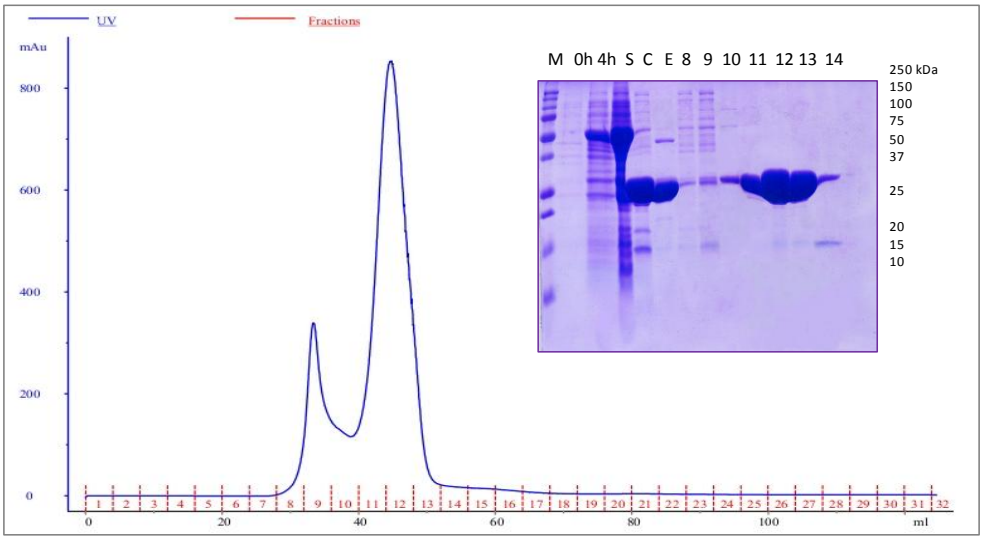

Figure 13: Purification of aMBL-1. Sephacryl S-100 column elution profile of the protein eluted in the second peak as confirmed by SDS PAGE. The inset shows the analysis by SDS-PAGE of the different purification steps of the protein (M, molecular weight markers; 0h: sample before induction; 4h, sample after 4h induction with IPTG, S, supernatant; C, eluted protein after cleaving with 3C-protease; E, elution of the GST-Tag with 10 mM reduced glutathione; 8-14, corresponding fractions of the size-exclusion chromatography.

3.3. PROTEIN IDENTIFICATION BY MALDI-TOF-MS

A mass fingerprint of aMBL-1 was obtained by MALDI-TOF mass spectrometry. The protein band was excised from the gel followed by limited proteolytic digestion using trypsin. The peptide masses of the breakdown products were compared to that of the theoretically tryptic peptides, and fourteen tryptic peptides were identified. They cover 67 % of the protein sequence and showed different percent confidence intervals: 99.0 (green), 97.4 (purple) and 18.4 (red).

M K L F K L S A S A L A T A T A L T M A Q S A L A Q D L K I Q S F L A K P E H F G V T S T L I E G D K E V L L V N A Q F S K **S E A L R I A A N I L D S G K T L K** T I F V S Y G D P D Y Y F G L D V F K Q Y F P N V Q I I A T P E T V K **H I Q D T Q A L K V K** Y W G P Q M G A N A P S Q I I V P Q A Y T A K **T L K L E N E S I E I K G K K** E L T Y L W V P S A K A V V G G I P V S S G I H L W M A D T P K T R D R V E V I Q S L E S I K **A L Q P K** I V V P A H M V E G A P Q G L D A V N F S I N Y L N S Y E K **A A K A T K N A T E L S K L M Q K** Q Y P T L Q S V D S L E L G A K **V V K G E M Q W P**

3.4. EXPRESSION OF SeMET-LABELED PROTEIN

The expression and purification of the SeMet-labeled aMBL-1 were the same as those used for the native protein. SeMet incorporation was confirmed by mass spectrometry [145]. Sequence analysis and mass spectrometry experiments were consistent with substitution of the five methionine residues (expected mass increase of 234 Da) (Figure 14).

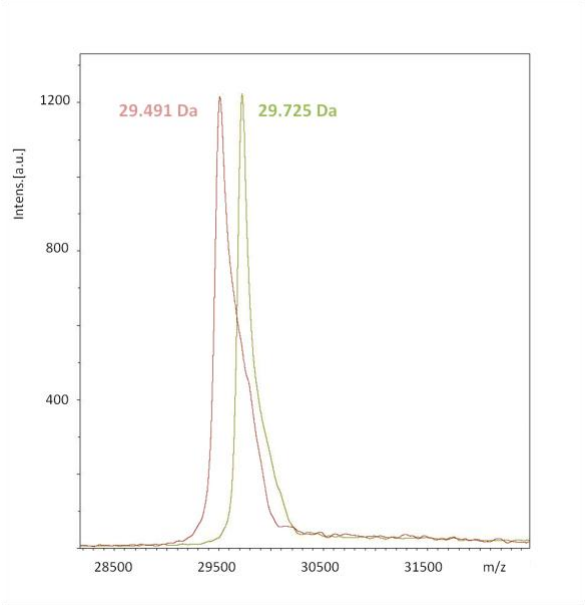

Figure 14: Mass spectra of the native (brown) and the SeMet labeled (green) aMBL-1.

4. Biophysical characterization

Structural studies require conditions where the protein has not only a high degree of purity but also it is stable and structurally homogeneous. Through gel filtration, an estimation of the molecular weight of aMBL-1 could be performed comparing its retention volume (Vr) with the values obtained for several known calibration standards eluted from the same column under similar conditions.

Moreover, analytical ultracentrifugation (AU) experiments provide valuable details about dynamic interactions, solution conformation and oligomerization properties of protein molecules by exposing them to large centrifugal forces [146].

4.1. ANALYTICAL GEL FILTRATION

The elution profile of aMBL-1 shows one single peak eluting at 14.94 ml (Figure 15). This corresponds to an apparent molecular mass of 54.95 ± 5 KDa. This indicates that this protein is present as a dimer in solution.

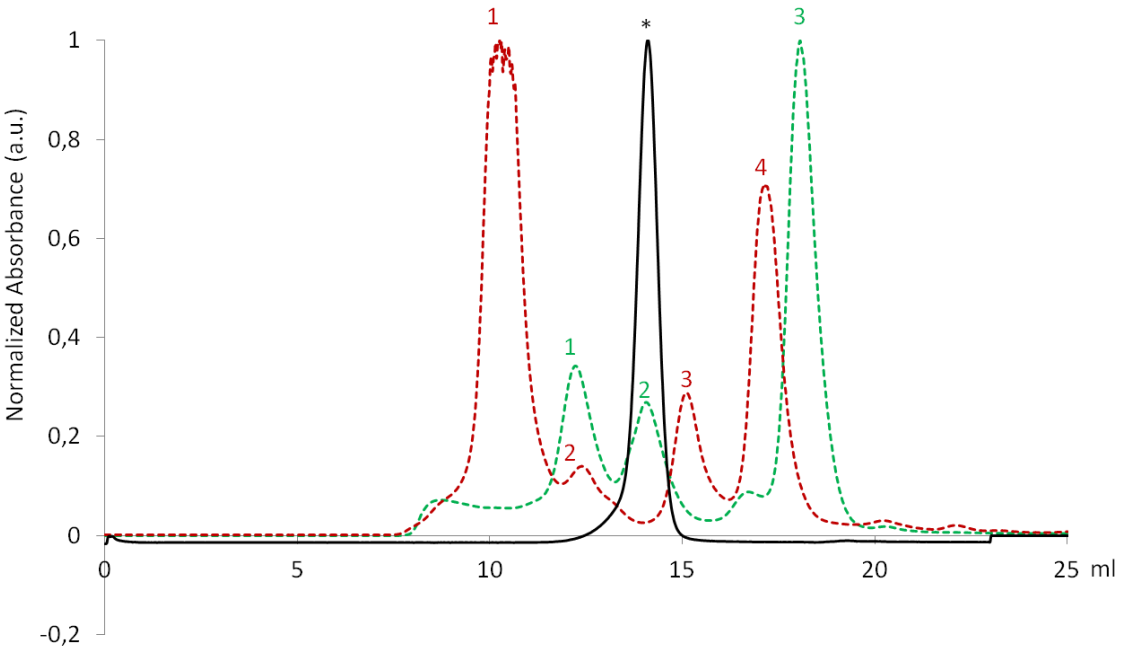

Figure 15: Elution profile of aMBL-1 (black line). Broken lines represent the different molecular weight standards used for calibrating the column. 1, Catalase (240 KDa), 2, Bovine Serum Albumin (68 KDa), 3, Cytochrome C (13 KDa). And 1, Ferritin (450 KDa), 2, Aldolase (158 KDa), 3, Egg albumin (45 KDa), 4, Chymotrypsinogen A (25 KDa).

4.2. ANALYTICAL ULTRACENTRIFUGATION

The oligomerization state in solution of aMBL-1 was analyzed by analytical ultracentrifugation (AU) [104]. The sedimentation profile of the protein obtained in the velocity experiments (Figure 16) showed a single peak with a sedimentation coefficient of 3.7 ± 0.1 S for all tested protein concentrations (see Materials and Methods).This corresponds to an estimated molecular weight of 55,124 Da.

A more precise determination of the molecular mass of the single species of aMBL-1 present in solution, as seen by sedimentation velocity was carried out by sedimentation equilibrium. The experimental data could be fitted to the presence of a monodisperse single species in solution with an apparent molecular mass of 59,400±550 Da. This corresponds to the presence of a dimer in solution (Figure 16).

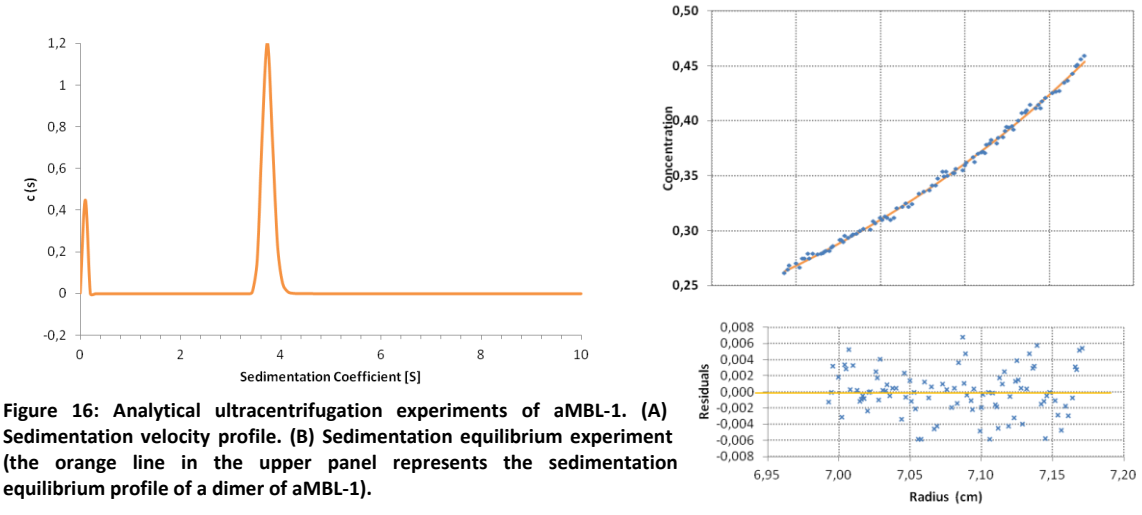

Figure 16: Analytical ultracentrifugation experiments of aMBL-1. (A) Sedimentation velocity profile. (B) Sedimentation equilibrium experiment (the orange line in the upper panel represents the sedimentation equilibrium profile of a dimer of aMBL-1).

5. Protein crystallization

Initial crystallization assays were carried out by the sitting drop vapour-diffusion method using sparse matrix crystallization screens at 22 °C [134]. The protein used for crystallization was in 50 mM Tris-HCl, buffered at pH 7.5, containing 100 mM NaCl and 1 mM DTT at 20 mg/ml with drops of 0.2 + 0.2 µl (protein + reservoir solution). Initial crystal hits from the commercial crystallization kits are shown in Figure 17.

Figure 17: Initial crystal hits of aMBL-1 from the commercial crystallization kits: (a) CUSTOM I - (A12): 27.49 % PEG-MME 5K, 100 mM Imidazole-Maleate 7.5; (b) CUSTOM I - (E10): 35.09 % PEG 2K, 1.12 % Ethanol, 0.67 % LDAO; (c) Jena Bioscience Classics 2 - (C3): 25 % W/V PEG 4000, 100 mM MES Sodium Salt 6.5, 200 mM Magnesium Chloride; (d) Jena Bioscience Classics 7 - (C5): 30 % MPD, 10 % w/v PEG 4000, 100 mM Imidazole-HCl 8.0; (e) CUSTOM IV – (D9): 26.43 % PEG 6K, 100 mM BisTriPro 4.5;

These initial crystallization conditions were further optimized to improve diffraction quality. Refinement of conditions A12 from CUSTOM I, C3 from Jena Bioscience Classics 2, C5 from Jena Bioscience Classics 7 and D9 from CUSTOM IV were carried out varying the precipitant concentration and the buffer pH in a fine gradient, while keeping fixed the other components of the solution. For condition E10 from CUSTOM I, the concentration of the detergent (LDAO) was kept constant varying the concentration of PEG2K and the percentage of ethanol.

The best diffracting crystals grew in the optimized CUSTOM I (E10) solutions (45-49 % PEG2K, 1.2-1.7 % ethanol and 0.67 % LDAO) in 1-2 weeks using a drop size of 0.5 µl (Figure 18). The typical crystal size was 400 x 60 x 60 µm. The initial trials with the commercial solution gave crystals that belonged to the $P2_1$ monoclinic space group. However, the home made solutions of this condition gave crystals that belonged to the $P2_12_12_1$ orthorhombic space group.

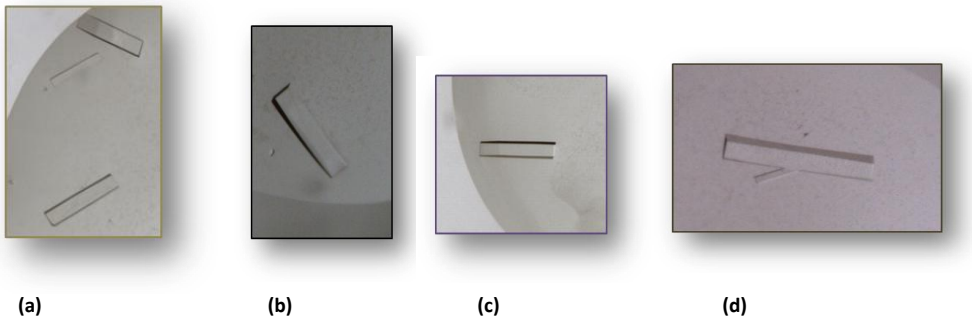

Figure 18: Orthorhombic crystals obtained using the home made E10 condition from CUSTOM I. (a) 45 % PEG2K, 1.2 % Ethanol, 0.67 % LDAO; (b) 47 % PEG2K, 1.5 % Ethanol, 0.67 % LDAO; (c) 47 % PEG2K, 1.7 % Ethanol, 0.67 % LDAO; (d) 49 % PEG2K, 1.5 % Ethanol, 0.67 % LDAO.

6. Structure determination

6.1. NATIVE DATASETS

6.1.1. DATA COLLECTION AND PROCESSING

aMBL-1 crystallized in two different space groups (Monoclinic and Orthorhombic). Two high-resolution datasets were collected on ID14-1 and ID14-4 beamlines at the ESRF (Grenoble, France) at cryogenic temperatures. Crystals were cryoprotected with 5-15% PEG 400 in the crystallization condition and then flash-cooled in liquid nitrogen.

The monoclinic crystal form diffracted X-rays to significantly higher resolution (1.7 Å) than the orthorhombic crystal form (1.9 Å) (Figure 19). This lower resolution could be explained because monoclinic crystals were collected at ID14.4, a beam line which is about 10 times more intense than ID14.1, but also by the solvent content. It should be mentioned that orthorhombic crystals contained higher solvent content than the monoclinic one (44.0 and 38.6 %, respectively).

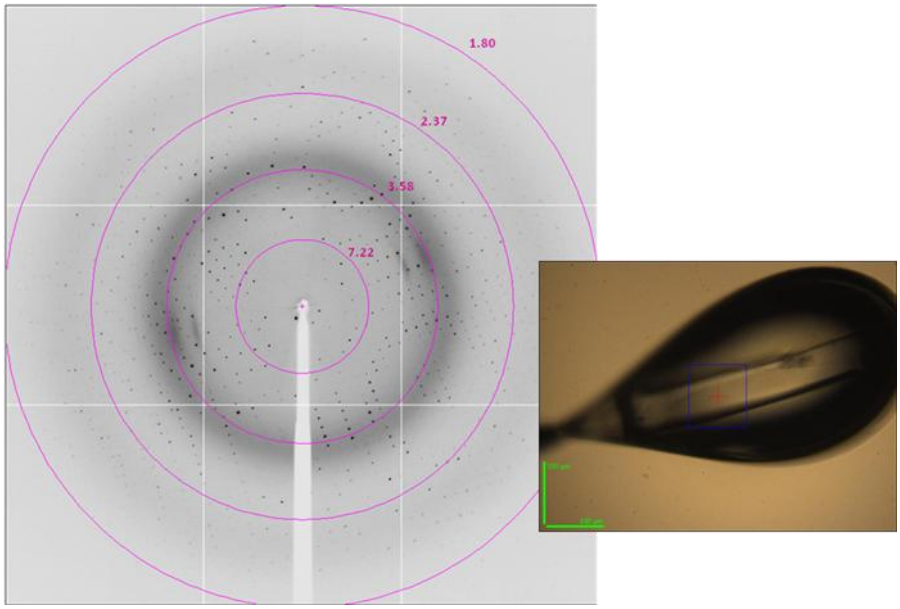

Figure 19: Diffraction pattern of the native orthorhombic crystal form of aMBL-1.

Data were integrated with MOSFLM [111]. The unit cell dimensions, crystal symmetry and crystal orientation were obtained from the experimental diffraction pattern. Then, a local scaling of the data was applied to reduce systematic errors with programs of the CCP4 suite (see Materials and Methods). Data collection statistics are summarized in Table 7.

Table 7: Data collection statistics for aMBL-1 crystals

	Monoclinic	**Orthorhombic**
X-ray source	ESRF/ID14.4	ESRF/ID14.1
X-ray detector	Q315r ADSC CCD	Q210 ADSC CCD
Wavelength (Å)	0.97700	0.93340
Space group	P 2_1	P 2_1 2_1 2_1
a,b,c (Å)	52.71, 56.18, 79.98	44.35, 86.41, 135.15
α,β,γ (°)	90.00, 93.59, 90.00	90.00, 90.00, 90.00
Matthews coefficient (Å ^{3} Da^{-1})	2.00	2.19
Solvent content (%)	38.64	44.00
Molecules in the asymmetric unit	2	2
Resolution range (Å)*	79.83 – 1.70 (1.79 – 1.70)	45.05 – 1.90 (2.0 – 1.90)
Number of observations*	171137 (17384)	296679 (41900)
Unique reflections*	50385 (6658)	41051 (6030)
Completeness (%)*	97.9 (89.7)	99.9 (99.7)
Multiplicity *	3.4 (2.6)	7.1 (6.8)
R sym [a]*	0.061 (0.294)	0.051 (0.493)
R meas[b]*	0.072 (0.368)	0.055 (0.533)
R pim [c]*	0.038 (0.217)	0.021 (0.202)
Mean I/σ(I)[d]*	13.9 (3.6)	26.7 (3.8)

[a] Rsym = Σhkl Σi |Ii(hkl) - <I(hkl)>| / Σhkl Σi Ii(hkl); [b] Rmeas = {Σhkl [N/(N-1)]1/2 Σi |Ii(hkl) - <I(hkl)>|}o / Σhkl Σi Ii(hkl), where Ii(hkl) are the observed intensities, <I(hkl)> are the average intensities and N is the multiplicity of reflection hkl; [c] Rp.i.m. = Σ √(1/n-1) | Ihl - <Ih>| / Σ | <Ih>|; [d] [I/σ(I)] is the relation between the intensity of the diffraction and the background; *Values in parentheses are for the highest resolution shell.

An initial molecular replacement search was carried out separately for both crystal forms with Molrep [147] from the CCP4 package. No reasonable solutions could be retrieved using the coordinates of several members of the MBL superfamily (**2fhx** with 36% of identity, **2yz3** with 35% of identity) as search models.

Due to the failure of the molecular replacement, crystals of the SeMet labeled aMBL-1 were obtained in order to obtain the phases through experimental methods (Multiple-wavelength Anomalous Dispersion).

6.2. DERIVATIVE DATASETS

6.2.1. DATA COLLECTION AND PROCESSING

The Se-Met labeled aMBL-1 protein produced crystals that belonged to the orthorhombic space group $P2_12_12_1$. The presence of selenium atoms was confirmed by X-ray fluorescence (Figure 20) and three datasets at three different wavelengths were collected at ID14.4 beamline (ESRF-Grenoble, France). The fluorescence scan was used to determine the peak, inflection and remote experimental wavelengths for the Se present in the protein.

Energy (eV)	**f´**	**f´´**
12.6597	-8.51	5.70
12.6577	-9.66	3.36

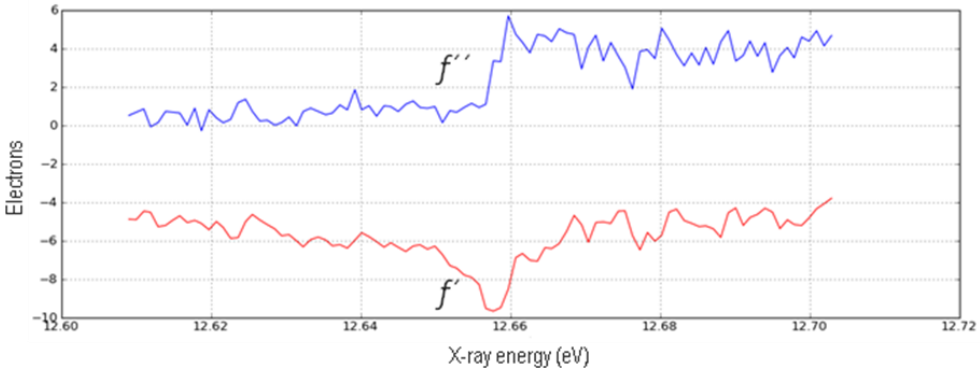

Figure 20: Experimental anomalous scattering curves from a crystal of Se-Met labeled aMBL-1. The f'' (blue curve) is proportional to the atomic absorption coefficient at the K absorption edge of Se. Dispersive difference between data is proportional to the difference in f' (red curve).

The three datasets collected at the peak, inflection and remote wavelengths of the selenium were indexed, integrated and reduced using XDS and scaled with SCALA from the CCP4 suite. Local scaling of the data was applied to reduce errors among the datasets and to place the data on an approximately absolute scale. Data collection statistics of SeMet labeled aMBL-1 crystals are summarized in Table 8.

Table 8: Data collection statistics for SeMet labeled aMBL-1 crystals

	PEAK	INFLECTION	REMOTE
X-ray source	ESRF/ID14.4		
X-ray detector	Q315r ADSC CCD		
Oscillation range (°)	1.0		
Exposure Time (s)	0.4		
Wavelength (Å)	0.9794	0.9795	0.9770
Space group	$P2_12_12_1$		
a,b,c (Å)	45.95, 87.61, 137.27	45.78, 87.52, 136.98	45.80, 87.72, 137.12
α,β,γ (°)	90.00, 90.00, 90.00		
Matthews coefficient ($Å^3 Da^{-1}$)	2.34		
Solvent content (%)	47.57		
Molecules in the asymmetric unit	2		
Resolution range (Å)	45.79 - 2.40 (2.53 - 2.40)	45.78 - 2.65 (2.79 - 2.65)	45.78 - 2.85 (3.0 - 2.85)
Number of observations*	176916 (25865)	118017 (17320)	105406 (15488)
Unique reflections*	22393 (3210)	16659 (2382)	13502 (1925)
Completeness (%)*	99.8 (100.0)	99.7 (100.0)	99.7 (100.0)
Anomalous completeness	99.9 (100.0)	99.8 (100.0)	99.8 (100.0)
Anomalous multiplicity	4.2 (4.2)	3.8 (3.8)	4.2 (4.2)
R meas [a]*	0.088 (0.551)	0.073 (0.527)	0.090 (0.444)
R pim [b]*	0.041 (0.263)	0.037 (0.268)	0.048 (0.242)
Mean I/σ(I) [c]*	15.4 (3.2)	20.2 (4.1)	17.8 (3.4)
Anomalous signal+	1.027	0.837	0.864
Phasing power+	1.162	-	-
Figure of merit+	0.45	-	-

[a] R meas = {Σhkl [N/(N-1)]1/2 Σ_i $|I_i(hkl) - \langle I(hkl)\rangle|$} / Σhkl Σ_i $I_i(hkl)$, where $I_i(hkl)$ are the observed intensities, $\langle I(hkl)\rangle$ are the average intensities and N is the multiplicity of reflection hkl; [b] R p.i.m. = Σ √(1/n-1) | Ihl - <Ih>| / Σ | <Ih>|; [c] [I/σ(I)] is the relation between the intensity of the diffraction and the background; *Values in parentheses are for the highest resolution shell. [+] Values at 3.0 Å resolution.

6.2.2. STRUCTURE DETERMINATION AND REFINEMENT

Probably due to the low phasing power, the Patterson maps didn't show clear peaks at the corresponding Harker sections. Heavy-atom sites, initial phases, map calculation and density modification were carried out with the program AutoSHARP [120] at 2.39 Å , using the peak, inflection and remote datasets, with the peak as the reference. The 10 expected Selenium sites were found (Table 9) and used for the estimation of the initial phases.

Table 9: Final coordinates and occupancies of the Se atoms

	(fractional coordinates)			
Se atom	x	y	z	Occupancy
1	0.2213	0.2105	0.1854	0.2774
2	0.4652	0.3063	0.1841	0.3442
3	0.8275	0.4649	0.0681	0.2774
4	0.2640	0.4402	0.2688	0.3046
5	0.6274	0.5982	0.1359	0.2506
6	0.3073	0.1227	0.2041	0.2860
7	0.0468	0.2372	0.3043	0.2844
8	0.6523	0.4573	-0.0595	0.2519
9	0.5617	0.5137	0.1053	0.2180
10	0.3816	0.6223	0.0091	0.1976

The MAD maps were calculated on both hands. Two criteria were used to choose the correct hand: 1) the correlation coefficient between observed E2 values (normalized structure factors [148]) and E2 values based on the modified map and 2) by inspection of the resulting electron density maps. The initial map (Figure 21a) shows clear boundaries between the protein and the solvent. Phases were further improved by density modification and a closer inspection revealed some secondary structure elements, such as the two α-helices in Figure 21b showing clear density for the side chains.

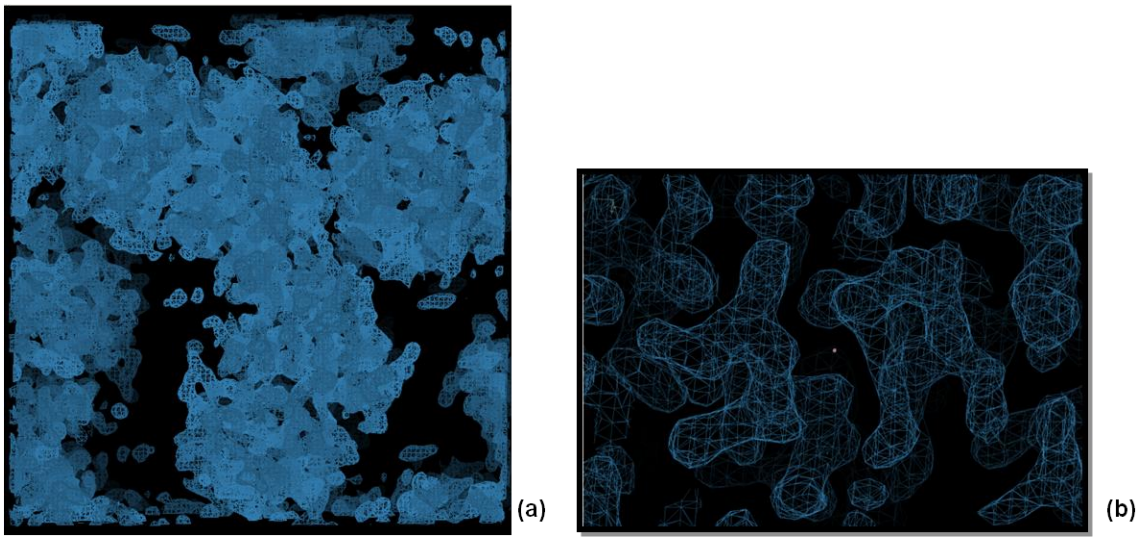

Figure 21: Resulting electron density map where (a) clear boundaries between protein and solvent region can be identified. (b) Clear electron density map of two parallel helices and the lateral chains of some aromatic residues.

An initial model of the content of the asymmetric unit was obtained with the program AUTOBUILD implemented in the PHENIX suite [121] using the initial phases (in form of Hendrickson-Lattman coefficients) obtained with the program SHARP.

The initial model was built automatically, and consisted of 519 residues in 22 fragments and 76 waters ([R/Rfree]=0.2923/0.3514 values and CC=75 %). A final model was obtained after several rounds of iterative manual building Coot [122] and refinement PHENIX using the 2.4 Å peak dataset with R_{work} and R_{free} values of 21.6 and 25.5%, respectively. Finally, this model was further refined against the native orthorhombic data set up to a resolution of 1.9 Å

The final model was optimized in an iterative process of refinement and manual model building, applying translation-libration-screw (TLS) groups which were identified by PHENIX, using a method similar to that defined by the TLSMD server [149]. Then, molecules were analyzed for inter-domain motions or flexibility and individual chains were partitioned into multiple segments that were modeled as rigid bodies.

After the structure for the orthorhombic crystal form of aMBL-1 was solved, the monoclinic crystal structure was elucidated by molecular replacement using the orthorhombic model and then refined up to a resolution of 1.7 Å. This allowed a better fit of some regions of the molecule that were not well defined in the electron density maps from the orthorhombic crystals.

Finally, water molecules were added automatically with Coot and checked manually at the final refinement step for both crystal forms. The final refinement statistics are shown in Table 10.

Table 10: Refinement analysis of aMBL-1

Space group	$P2_1$	$P2_12_12_1$
Resolution (Å)	1.7	1.9
No. of reflections	50368	41826
R [a] (Rfree [b]) (%)	15.44 (18.48)	17.07 (21.86)
Number of atoms		
Protein	4756	4514
Water	602	378
Cl	-	3
SO_4	-	1
PEG	-	1
BEZ	2	2
R.m.s.d. [c]		
Bond length (Å)	0.007	0.006
Bond angles (^{o})	1.058	1.019
B factor [d] (Å^2)		
Protein (main/side chain)	13.74/20.36	27.81/33.70
solvent	25.44	34.95

[a] R = Σhkl {[Fobs(hkl)] - [Fcalc(hkl)]} / Σhkl [Fobs(hkl)], where Fobs(hkl) and Fcalc(hkl) are the observed and calculated structure factors, respectively. [b] R_{free} corresponds to R calculated using 5 % of the total reflections selected randomly and excluded during refinement; [c] R.m.s.d. is the root mean square deviation. [d] B-factor indicates the true static or dynamic mobility of an atom.

6.3. VALIDATION OF THE STRUCTURE

The aMBL-1 structure displayed two chains in the asymmetric unit together with 807 water molecules and two ligands (benzoate, BEZ). Five residues, Asn184, Glu188 and Arg247 in subunit A and Tyr67 in both subunits, have been modeled in dual conformations. As the monoclinic crystal form diffracts

to higher resolution than the orthorhombic one, the $P2_1$ structure will be used as the representative model in all further discussions.

The final model has a good geometry with 97 % of the residues located in the most favored regions of the Ramachandran plot and only one residue was located in the outlier region, adopting an unusual backbone conformation: Asn57 in both subunits, although it is perfectly fitted in the electron density map (Figure 22a). Summary statistics from the protein geometry obtained for the final model are summarized in Figure 22b.

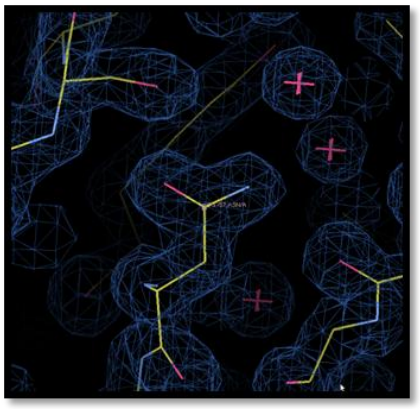

(a)

Molprobity: PROTEIN GEOMETRY		Goal (%)
Poor rotamers	0	< 1
Ramachandran outliers	0.95	< 0.2
Ramachandran favored	96.95	> 98
Cβ deviations >0.25Å	0	0
Residues with bad bonds:	0	0
Residues with bad angles:	0	< 0.1

(b)

Figure 22: (a) 2Fo-Fc electron density map in the region of Asn57 contoured at 1.2σ. (b) The quality of the final refined model of aMBL-1 was overall very good, with [R/Rfree]=0.1544/0.1848 values and displaying a good stereochemistry as defined by Molprobity.

7. Architecture of aMBL-1

7.1. OVERALL FOLDING

The monomer of aMBL-1 has a globular shape with approximate dimensions of 55 x 42 x 42 Å. The secondary structure elements are organized in a typical αβ/βα fold that characterizes the MBL superfamily (Figure 3a) [35] [61]. The central core composed by the two β-sheets of six (A1-A6) and five strands (B1-B5), facing each other, is surrounded by five solvent exposed α-helices. The first β-sheet (A) is formed by β-strands A1 (from residue Lys29 to Leu34), A2 (Thr43-Glu48), A3 (Glu52-Leu55), A4 (Thr78-Phe83), A5 (Gln106-Ala109) and A6 (Gln144-Ala146), while the second includes β-strands B1 (Thr150-Leu153), B2 (Glu156-Lys163), B3 (Leu166-Val171), B4 (Ala176-Val178) and B5 (Lys216-Val219). Both β-sheets have mixed parallel (A3, A4, A5 and A6; B4 and B5) and antiparallel (A1, A2 and A3; B1, B2, B3 and B4) β-strands. They are linked on one side by α3-helix and a 10 residue-long loop (Gly133-Pro143), whereas on the other side strands A2 and B5 are connected by hydrogen bond interactions (Gly41-Met223 and Thr43-Ala221) as well as by a tight packing of hydrophobic residues. The connectivity of the structural elements is shown in Figure 23b.

Four of the α-helices (α1 (Lys62-Ser75), α2 (Leu95-Tyr101), α4 (Thr197-Ala212) and α5 (Gly230-Ala250) are flanking both sides of the plane of the β-sandwich, two (α1 and α2) on the side of sheet A and two (α4 and α5) on the side of sheet B whereas helix α3 (Pro111-Met132) covers one face of sheet A (Figure 23a).

This protein also presents two extra helices α6 (Ala254-Gln264) and α7 (Val271-Val281) (Figure 23, purple) located at the C-terminal region. These helices, not belonging to the MBL fold, are placed covering the entrance to the putative active site of a typical protein with this type of fold.

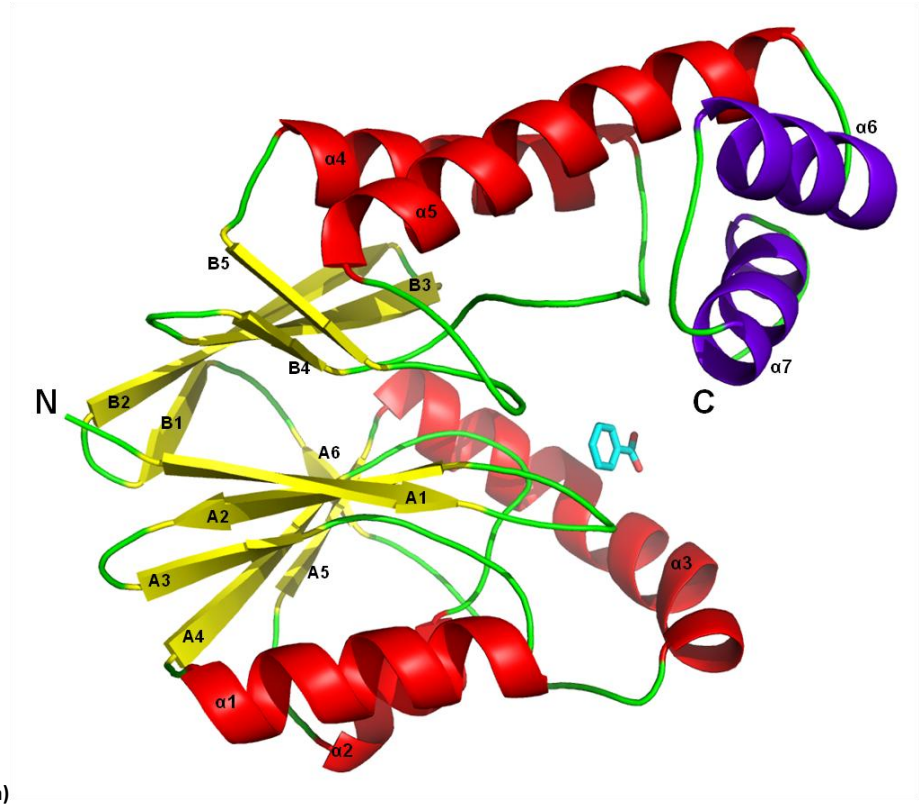
α4
α5
α6
B5
B3
B4
α7
N
B2
B1
C
A6
A1
A2
A3
A5
α3
A4
α1
α2

(a)

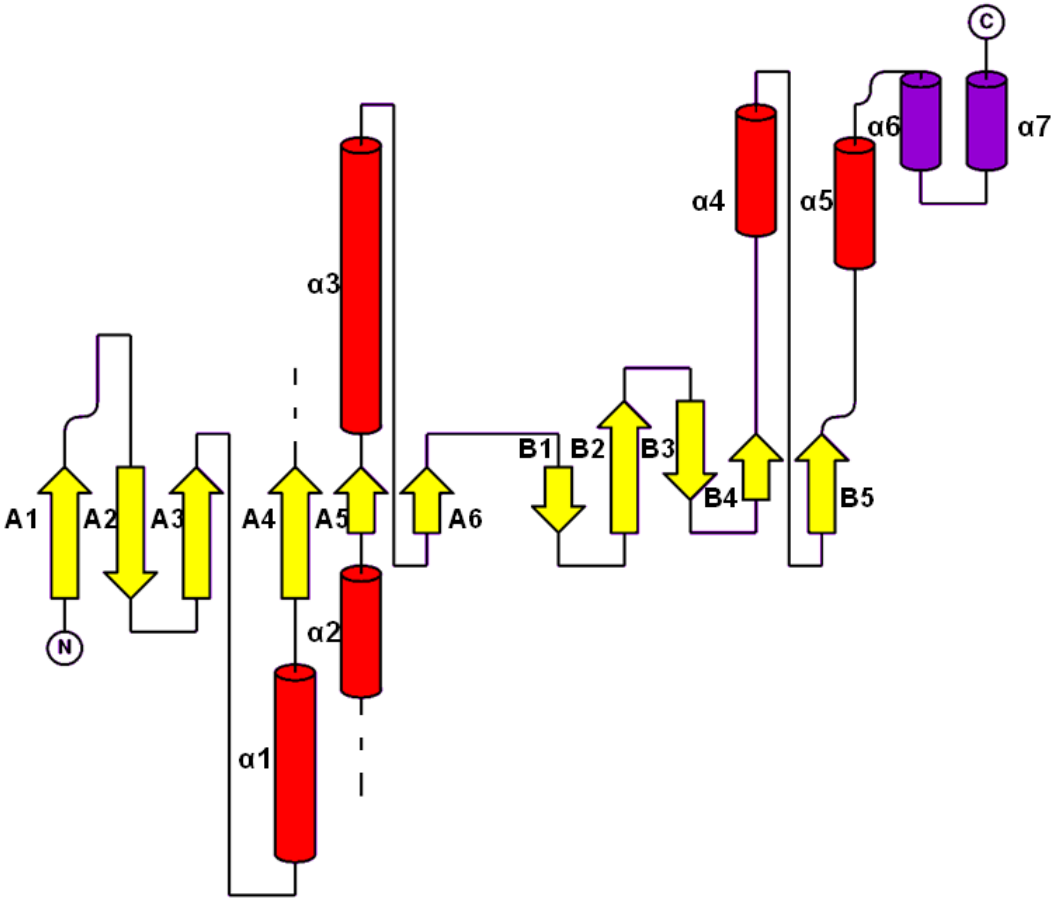
C
α6
α7
α4
α5
α3
B1
B2
B3
B4
B5
A1
A2
A3
A4
A5
A6
α2
α1
N

(b)

Figure 23: Structure of aMBL-1. (a) Ribbon diagram of the aMBL-1 monomer. The benzoate molecule is represented in ball-and-stick mode. (b) Topological diagram of the structure of aMBL-1. Secondary structure elements are labelled according to their position in the primary sequence, also the N and C termini are labelled as N and C, respectively. α-helices are shown as red and purple cylinders and β-strands as yellow arrows.

There is a molecule, interpreted as benzoate, at the mouth of the putative active site (Figure 23a), blocking its entrance.

There are two β-bulges in the structure of aMBL-1. The first one located at the β-strand A4 is a classic bulge formed by 3 residues: Leu79, Lys80 and Val53. The second β-bulge is a G1 bulge placed at the β-strand B4, in which the first residue is in the alpha left conformation: Val171, Lys175 and Ala176 (Figure 24).

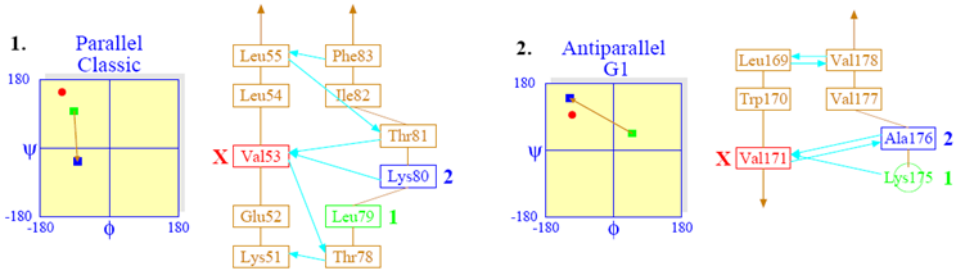

Figure 24: Ramachandran plots for the β-bulges, showing the ψ/ϕ angles of the residues involved. The red circle corresponds to the ψ/ϕ angles of residue X, and the green and blue squares correspond to residues 1 and 2, respectively. The type of bulge is indicated above the Ramachandran plot. To the right of the Ramachandran plot is a schematic diagram indicating the residues and hydrogen bonding patterns in and around the beta bulge.

7.2. DIMER INTERFACE

The asymmetric unit of both crystal forms of aMBL-1 are composed by two monomers related by a non-crystallographic 2-fold axis, similar to other proteins that present the MBL fold [78] [83] [74].

The solvent accessible surface area of both monomers is 11,700 Å^2 with an interface area of 630 Å^2 that falls within the range of values reported for dimeric proteins [150]. These data might indicate that the protein is a dimer in solution (Figure 25a).

The major part of the dimer interface is formed by helix α1 of each monomer that pack against each other in a head-to-tail fashion (Figure 25). Although the nature of the dimer interface is predominantly hydrophobic, polar interactions between the subunits involving hydrogen bonds and Arg-Asp salt bridges are also observed. The interface may be subdivided into three zones according to the main interactions (Figure 25b).

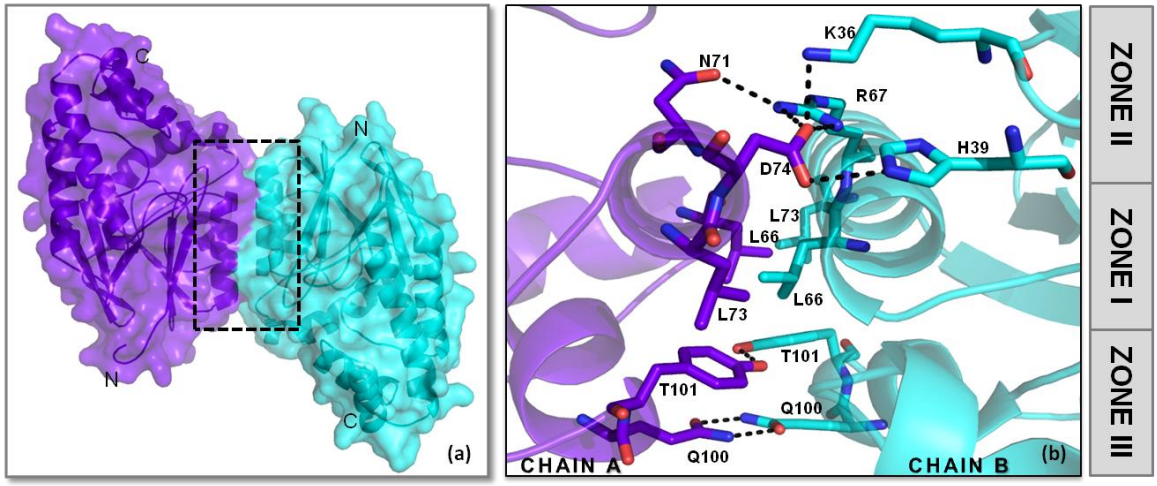

Figure 25: Dimer interface of aMBL-1. (a) View of overall conformation of the dimer and the interaction interface indicated by the black square. (b) Close-up view of the interactions between monomers at the dimer interface with representation of the side chains of residues (sticks) involved in the dimerization. The dimer interface has been divided into three zones, according to location and type of interactions. For clarity, only residues of zone II on the close side of the helix are represented, those on the far side, that are a copy of those represented, are not shown. H-bonds are represented by the black dashed lines.

Zone I is made up by residues from helix α1 of both monomers and defined the central nucleus of the dimer interface. Leu66 and Leu73 from one monomer establish hydrophobic interactions with the corresponding symmetry related residues from the neighboring monomer (Figure 25b).

Zone II is located above this central nucleus and made up, mainly by salt bridges fixing the side chains of the residues involved. They are located at the edge of helix α1 (Arg67) in each monomer reinforced by the side chains of Asn71 and Asp74 from neighboring monomers. Additional residues, Lys36 and His39, from the same monomer close to Arg67, help to stabilize the dimer interface (Figure 25b).

Zone III is made up by residues belonging to helix α2 (Gln100, Tyr101) from both monomers. A symmetrical network of hydrogen bond interactions involving the corresponding side chains help to stabilize this region and further enhanced by hydrophobic interactions between Leu73 and the aromatic ring of Tyr101 (Figure 25b).

A summary of the interactions occurring at the dimer interface is shown in Table 11.

Table 11: Contacts between monomers at the dimer interface

Monomer A	Monomer B	Distance (Å)	Comments
Zone I			
CB L66	O L66	3.97	Hydrophobic interaction
CD1 L66	CD1 L73	3.69	Hydrophobic interaction
CD2 L66	CD2 L66	3.86	Hydrophobic interaction
Zone II			
NH1 R67	OD2 D74	2.90	Salt bridge
NH2 R67	OD1 N71	2.93	Salt bridge
NH2 R67	OD2 D74	2.87	Salt bridge
OD1 N71	NH2 R67	2.86	Salt bridge
OD2 D74	NH1 R67	2.94	Salt bridge
OD2 D74	NH2 R67	2.80	Salt bridge
Zone III			
OE1 Q100	NE2 Q100	2.83	Hydrogen bond
NE2 Q100	OE1 Q100	2.76	Hydrogen bond
OH T101	OH T101	2.71	Hydrogen bond

7.3 PUTATIVE ACTIVE SITE

Most members of the MBL superfamily present a conserved sequence motif, His-X-His-X-Asp/His, that binds the metal atoms and forms the active site of these proteins (Figure 26B) [63].

Sequence and structure alignment of aMBL-1 with other members of the superfamily did not show this conserved motif. The corresponding sequence motif in aMBL-1 is made up by the residues Tyr-X-Asp-X-Asp/His (Figure 26B). Only the last two residues are conserved; but the first two His residues of the motif that bind one of the metal atoms of the active site are not conserved (Figure 26A and B). These two residues have been substituted by residues that will not be able to bind any metal atom the same way as the typical motif of this superfamily. Also, the third His residue involved in the binding of one of the metal atoms (His 189, Figure 26B) is not present in aMBL-1, and has been substituted by an Ile181 (Figure 26B).

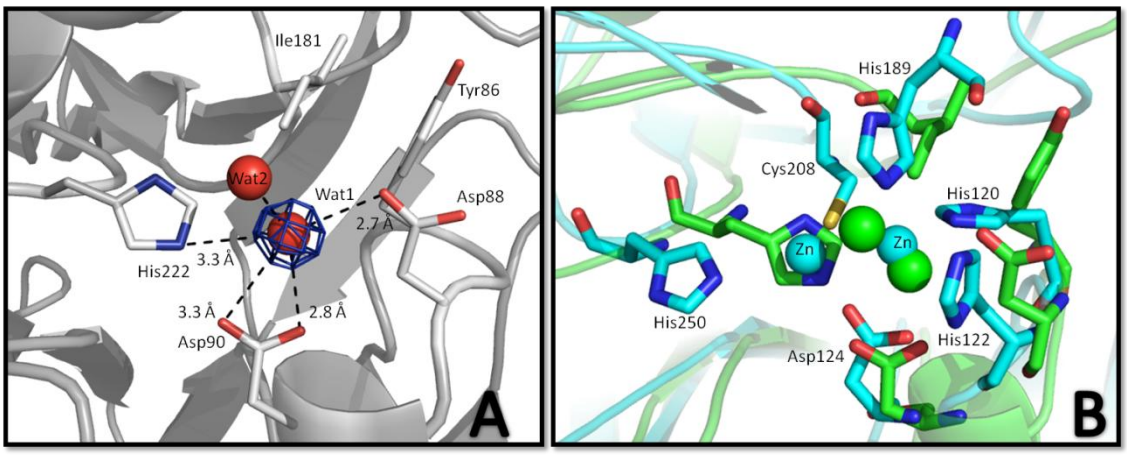

Figure 26: (A) Putative active site of aMBL-1. Residues equivalent to the conserved metal binding motif of the MBL superfamily are represented as sticks. Red balls represent two solvent molecules. (B) Structural alignment of the putative active site of aMBL-1 (blue) with the metal binding motif of the New Delhi-metallo-β-lactamase (NDM, green). Green balls represent solvent molecules from aMBL-1; and blue balls, labeled as Zn, represent the two zinc ions in the active site of NDM.

Although the geometry of the active site is superficially reminiscent of that observed in other members of the MBL superfamily [35], no Zn atoms could be placed in the density observed in this putative active site. The density found at the active site, in the place where one Zn atom is located on the typical metal binding motif, accounts for one molecule of water (Wat1, Figure 26A). This molecule is surrounded by Tyr86, Asp88, Asp90, His222 and Ile181, and displays a tetrahedral coordination through one interaction with Asp88 (2.7 Å), another with His222 (3.3 Å), two more with Asp90 (2.8 and 3.3 Å), and the last interaction, that completes the coordination sphere is to another solvent molecule (Wat2, Figure 26A).

The putative active site of aMBL-1 is located in a deep cavity, and made up by the loops that connect the secondary structure elements A1-A2, A2-α2 and B3-α5 (Figure 27A). The two C-terminal helices (α6 and α7) are located at the entrance of the putative active site blocking the access to the bulk solvent (Figure 27A).

At the entrance of the putative active site there is a hydrophobic cavity made up by three aromatic residues (Phe40, Trp128 and Trp287), Pro89 and Lys124 (Figure 27B). In this cavity there is an extra electron density. This density has been interpreted as a molecule of benzoate due to the shape of the electron density and the nature of the interactions (Figure 27B).

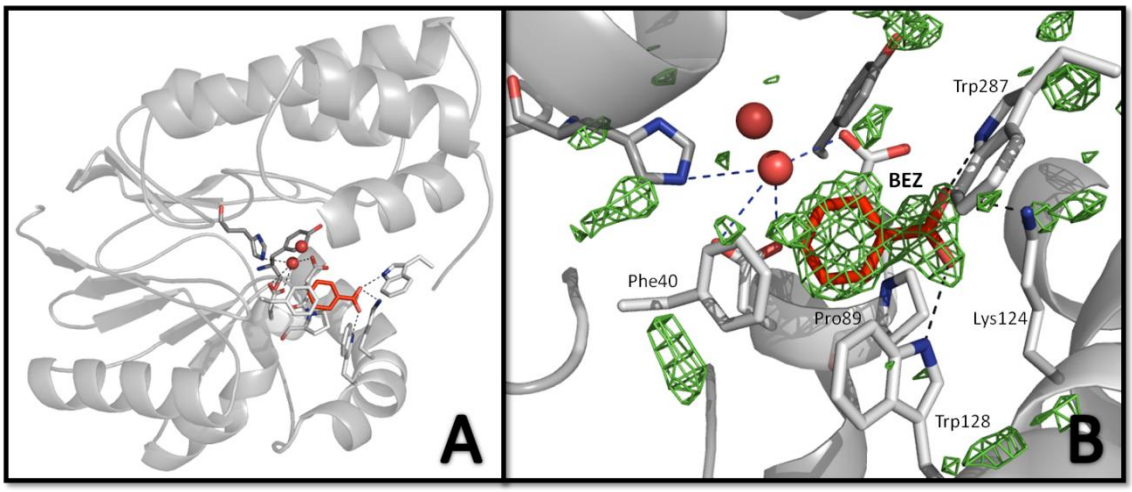

Figure 27: Putative active site of aMBL-1. (A) Location of the active site in the structure. (B) Electron density |2Fo|-|Fc|, contoured at 2σ, modelled as benzoate (BEZ). Hydrogen bonds are indicated by black dashed lines.

The aromatic ring of the benzoate establishes two parallel displaced π-π stacking interactions, one with the aromatic ring from Phe40 and other with Pro89. The two oxygens of the benzoate forms hydrogen bond interactions with the ring nitrogens of Trp287 (3.24 Å) and Trp128 (2.67 Å), and a third interaction to the ε-amino group of Lys124 (2.7 Å) (Figure 28).

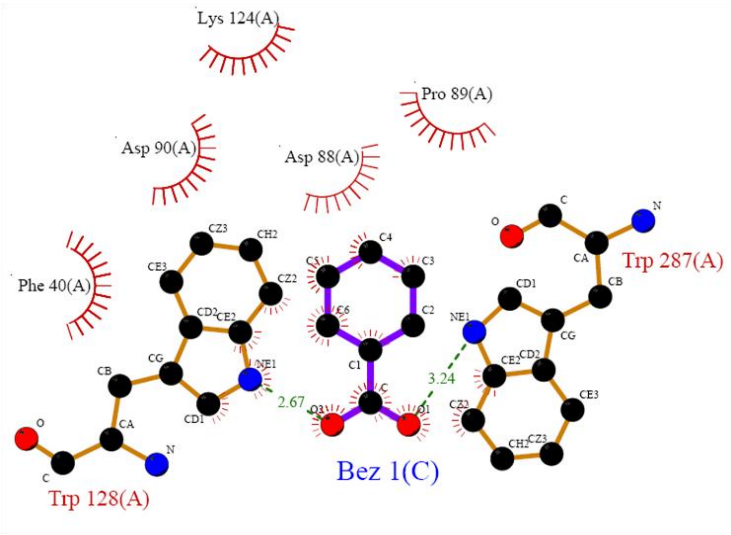

Figure 28: LIGPLOT representation of the hydrogen-bond network involving the benzoate in the putative active site of aMBL-1. Hydrogen bonds are indicated by green dashed lines, while hydrophobic contacts are represented by an arc with spokes radiating towards the ligand atoms they contact.

7.4. CRYSTAL PACKING IN THE TWO CRYSTAL FORMS

The structure of aMBL-1 was solved in two different crystal forms: monoclinic ($P2_1$) and orthorhombic ($P2_12_12_1$). The structure was first solved to 2.4 Å using the orthorhombic crystal form and a three-wavelength SeMet MAD experiment, and the monoclinic crystal form was solved by molecular replacement to 1.7 A using the coordinates of the orthorhombic crystals. In both structures, the asymmetric unit contains two molecules arranged in a head-to-tail manner with subtle differences in the interactions between the subunits. In the monoclinic form, the dimer interface is formed by contacts between the long loop region that connects helix α3 to the β-strand A6 (residues Gly133-Pro143) (Figure 29a). In the orthorhombic crystal form, the subunits are arranged in such a way that monomers A contact via helix α2 and helix α5 and through helix α4 from chain A with helix α2 from chain B.

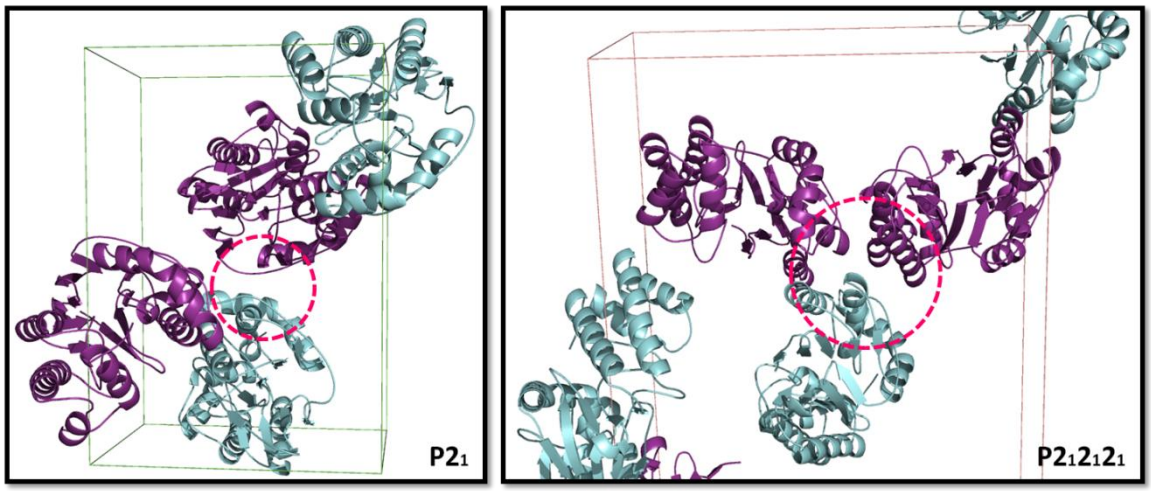

Figure 29: Arrangement of the aMBL-1 dimers in the two crystal forms: (A) Monoclinic ($P2_1$) and (B) orthorhombic ($P2_12_12_1$). The homodimers are depicted in purple (Chain A) and in cyan (chain B) and the interactions area is highlighted in pink.

Superposition of the homodimers in both crystal forms showed the same dimerization interface but with small differences at the C-terminal. The rms deviation value was 1.567 Å for all Cα atoms.

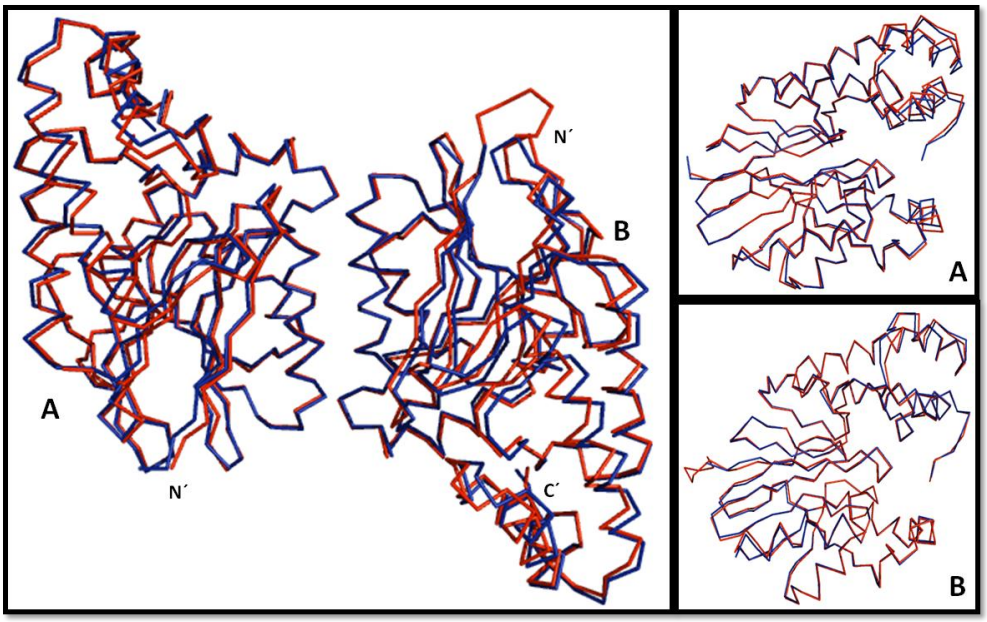

Figure 30: (Right) Superposition of the Cα traces of the dimeric aMBL-1 observed in the two different crystal forms by Superpose program from CCP4. (Left) Superposition of the Cα traces of monomers obtained from the two different crystal forms. The main difference between $P2_1$ (red) and $P2_12_12_1$ (blue) crystal structures was observed at the C-terminus of the protein.

7.5. FUNCTIONAL ASSAYS

7.5.1. SUSCEPTIBILITY TESTING

After confirmation of increased expression of aMBL-1 gene constructions in pE-TRA vector cloned into both strains (*A. baylyi* and *A. baumannii* ATCC 17978) by reverse-transcriptase PCR (RT–PCR) (29.09 fold relative to the house-keeping gene, gyrB), different functional assays were carried out. The characterization goal was to find a biologically relevant function which confirmed the rest of conclusions got from initial x-ray crystallographic studies and to evaluate the hydrolytic efficacy against β-lactam antibiotics of the target protein.

β-lactamase activity was tested by an adaptation of the Masuda method. It was found that background-lawn formation by *E. coli* DH5α cells incubated overnight was inhibited by β-lactam antibiotic confirming the non-hydrolytic activity of these enzymes toward β-lactam antibiotics.

7.5.2. KINETIC EXPERIMENTS

In order to determine which chemical reaction is catalyzed by aMBL-1, diverse enzymatic assays were performed using a set of general chromogenic substrates. These substrates were chosen in order to test all possible functions among members of the MBL superfamily with comparable overall structure.

The β-lactamase activity was assayed against nitrocefin to confirm the previous negative results in the microbiological assays. The obtained results corroborate that aMBL-1 does not show any hydrolytic activity against β-lactam antibiotics.

To determine the glioxalase type II function, experiments against S-D-lactoylglutathione were performed. Any increament of absorbance at 412 nm was detected, confirming that aMBL-1 is also not active against this compound.

In order to analyze its phosphatase activity, serial dilutions of AMBL-1 samples were tested against the pNPP substrate. After 10-30 minutes of incubation at 37 °C any absorption change was observed at 405nm, confirming that the substrate has not been degraded. As indicative of phosphodiesterase activity, enzymatic assay against bispNPP were performed. In this assay, aMBL-1 did not display activity even when several phosphodiesters from the cell as single- and double-stranded DNA were tested.

To test the esterase activity, p-nitrophenyl ester was used, determing the liberation of p-nitrophenol by meassuring the absorbance at 410 nm. No changes were observed certifying that aMBL-1 did not hydrolyze this compound.

Assays for detecting acyl-CoA thioesterase activity thioesterase were performed rendering also negative results.

Finally, these assays were performed at different pH and supplying the buffer with different divalent metal ions (Mg^{2+}, Mn^{2+}…) showing the same negative results.

1. Sequence analysis

1. 1. ALIGNMENT AND SEQUENCE ANALYSIS

The *ABAYE0164* gene encodes a protein, aMBL-2 (http://www.ncbi.nlm.nih.gov/gene/6000355) that was classified by the InterPro web server into the metallo-β-lactamase superfamily. In a BLAST search, AMBL-2 was found to be similar to several metallo-β-lactamases and Zn-dependent hydrolases.

The prediction of the secondary structure elements performed with PSIPRED [141] is shown in Figure 31. In this protein no signal peptide sequence could be detected.

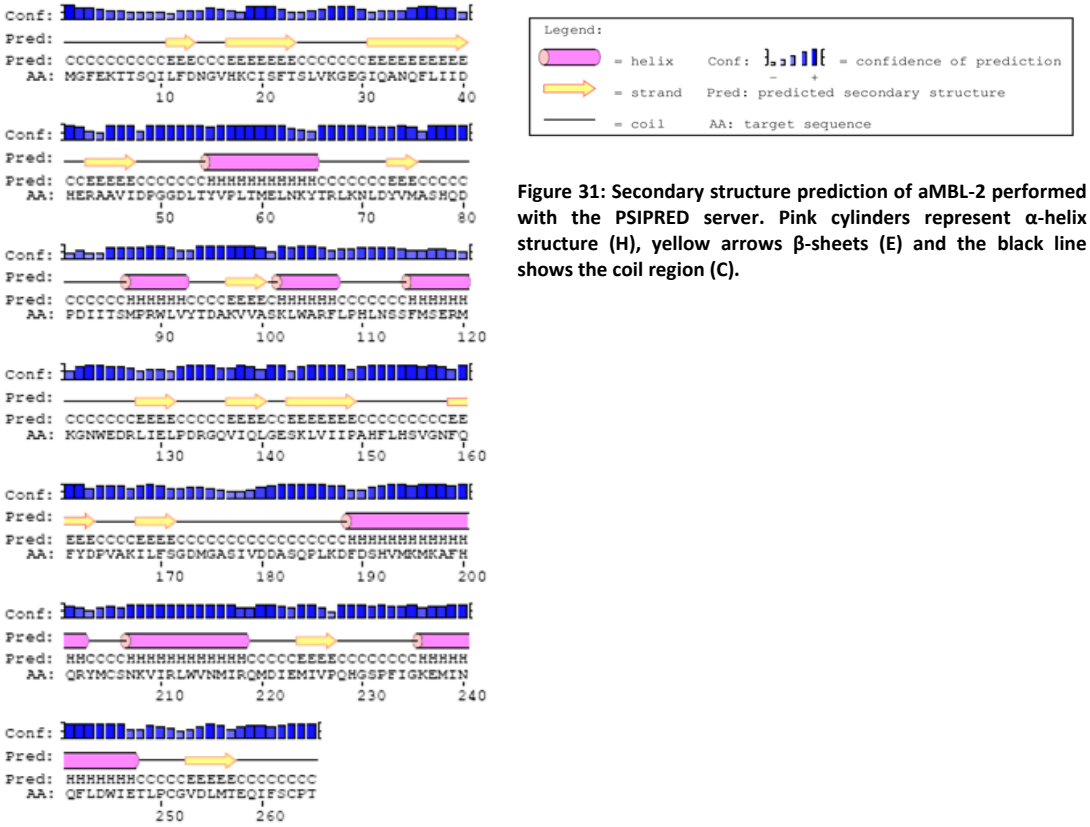

Figure 31: Secondary structure prediction of aMBL-2 performed with the PSIPRED server. Pink cylinders represent α-helix structure (H), yellow arrows β-sheets (E) and the black line shows the coil region (C).

Crystallization propensity predictions were performed with the XtalPred server [144] and aMBL-2 showed a high tendency to crystallize. The HHpred server [132] found a collection of related proteins that share the typical β-sandwich fold of the MBL superfamily.

2. Cloning

The aMBL-2 gene was amplified by PCR from the genome of *A. baumannii strain AYE* using the primers designed on the basis of its nucleotide sequence (see Materials and Methods). Since *Bam*HI restriction site was present into the aMBL-2 cDNA sequence, a silent mutation at the nucleotide position 249 (see Materials and Methods) was performed to eliminate this site without affecting the translated

amino acid sequence of the protein. Clones containing the mutation were selected by restriction analysis (Figure 32), and its sequence was confirmed by DNA sequencing.

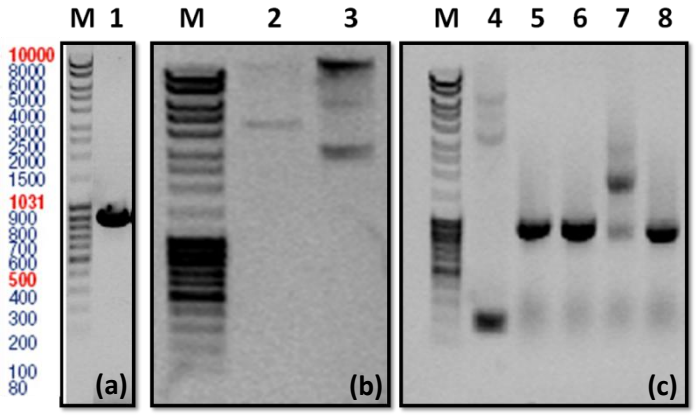

Figure 32: Agarose gels. (a)(1) Amplification of the aMBL-2 gene. (b) Restriction analysis of the mutated aMBL-2 gene in the pCRBlunt vector: (2) linearized vector with a single *Bam*HI site; (3) Non-digested vector. (c) Colony PCR for selection of positive clones (5, 6 and 8); (4) positive control (185 bp); (M) DNA molecular weight marker.

The coding sequence for aMBL-2 was inserted into the bacterial plasmid expression vector pGEX-6p-2 between the *Bam*HI and *Eco*RI restriction sites. This vector expresses the coding sequence for aMBL-2 (amino acids Met1 to Thr265) with an N-terminal GST fusion tag, and a 3C-protease cleavage site between them.

3. Protein expression and purification

3.1. PROTEIN EXPRESSION

Overexpression of soluble aMBL-2 was carried out in *E. coli* Rosetta (DE3) pLysS strain at 37 °C in LB media, induced with a concentration of 1 mM of IPTG during 4 h (Figure 33).

3.2. PROTEIN PURIFICATION

The protein aMBL-2 was purified using the same protocol described for aMBL-1 (see Materials and Methods).

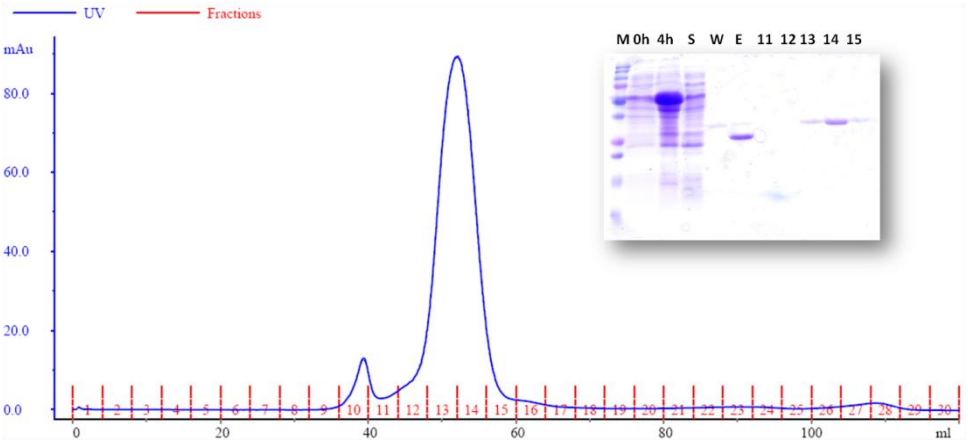

Figure 33: Purification of aMBL-2. Sephacryl S-100 column elution profile. The protein eluted in the second peak as confirmed by SDS PAGE. The inset shows the analysis by SDS-PAGE of the different purification steps of the protein (M, molecular weight marker; 0h, sample before induction, 4h, sample after 4h of induction with IPTG; S, supernatant; W, eluted protein after cleaving with 3C-protease; E, elution of the GST-Tag with 10 mM reduced glutathione; 11-15, corresponding fractions of the size-exclusion chromatography.

3.3. PROTEIN IDENTIFICATION BY MALDI-TOF-MS

A mass fingerprint of aMBL-2 was obtained by MALDI-TOF mass spectrometry. The protein band was excised from the gel followed by limited proteolytic digestion using trypsin. The mass of the breakdown products were compared to that of the theoretically tryptic peptides, and fourteen tryptic peptides were identified. They cover 60.8 % of the protein sequence and showed different percent confidence intervals: 98.9 (green) and 18.4 (red).

MGFEKTTSQILFDNGVHKCISFTSLVKGEGIQANQFLIIDHERAAVIDPGGDLTYVPLTMELNKYTRLKNL
DYVMASHQDPDIITSMPRWLVYTDAKVVASKLWARFLPHLNSSFMSERMKGNWEDRLIELPDRGQVIQ
LGESKLVIIPAHFLHSVGNFQFYDPVAKILFSGDMGASIVDDASQPLKDFDSHVMKMKAFHQRYMCSNK
VIRLWVNMIRQMDIEMIVPQHGSPFIGKEMINQFLDWIETLPCGVDLMTEQIFSCPT

3.4. EXPRESSION OF SeMET-LABELED PROTEIN

The expression and purification protocols for the SeMet labeled aMBL-2 were the same as those used for the native protein. SeMet incorporation was confirmed by mass spectrometry [145]. Sequence analysis and mass spectrometry experiments showed an increase of 703 Da in the labeled sample consistent with the substitution of fifteen methionine residues (Figure 34).

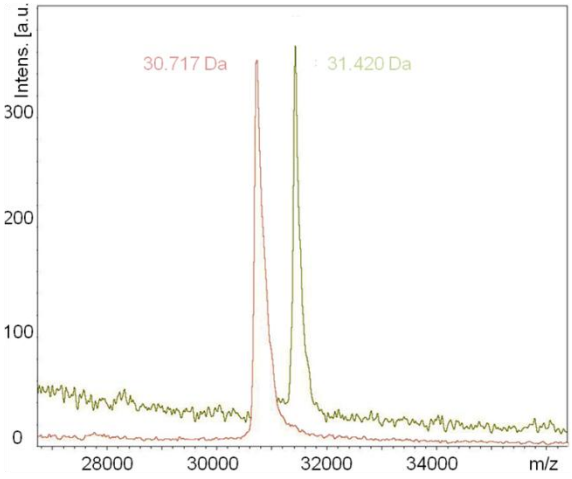

Figure 34: Mass spectra of the native (brown) and the SeMet labeled (green) aMBL-2.

4. Biophysical characterization

4.1. ANALYTICAL GEL FILTRATION

The elution profile of aMBL-2 shows a single peak eluting at 14.88 ml (black line, Figure 35). This corresponds to an apparent molecular mass of 56.23±5 KDa. This indicates that this protein is present as a dimer in solution.

Different standards are labeled as:

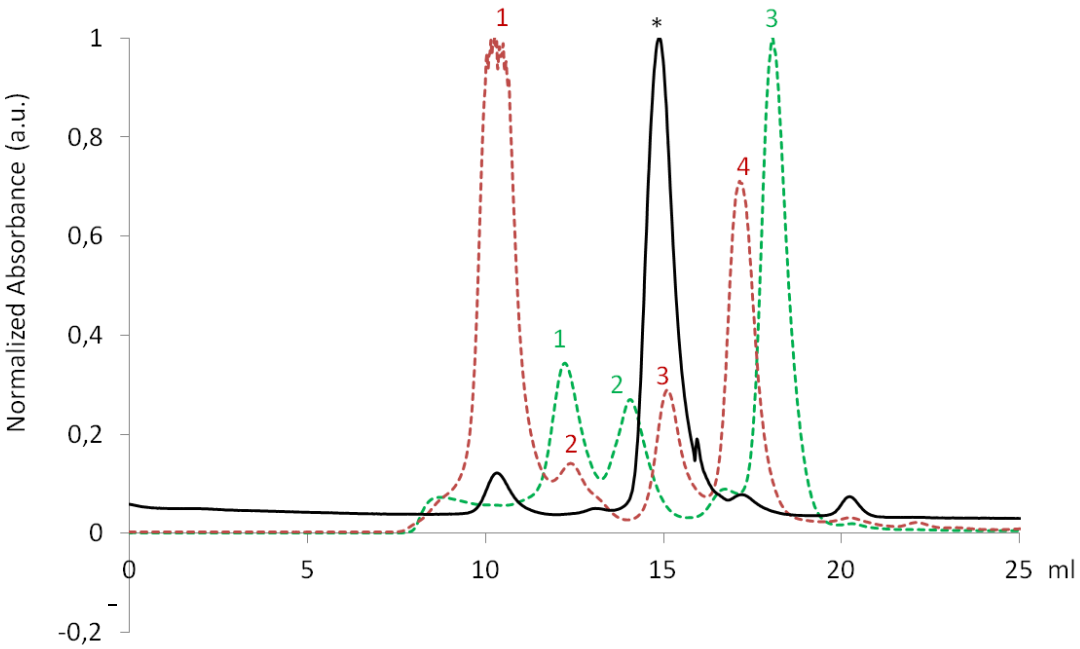

Figure 35: Elution profile of aMBL-2 (black line). Broken lines represent the different molecular weight standard used for calibrating the column. 1, Catalase (240 KDa), 2, Bovine Serum Albumin (BSA) (68 KDa), 3, Cytochrome C (13 KDa). And 1, Ferritin (450 KDa), 2, Aldolase (158 KDa), 3, Albumin egg (45 KDa), 4, Chymotrypsinogen A (25 KDa).

4.2. ANALYTICAL ULTRACENTRIFUGATION

The sedimentation profile of the protein obtained in the velocity experiment (Figure 36) shows a single peak with sedimentation coefficient of 4.2±0.1 S at the lowest protein concentration used (0.3 mg/ml). This corresponds to an apparent molecular mass of 52,148 Da. At higher concentrations of protein (> 0.9 mg/ml) a second peak with a higher sedimentation coefficient appeared.

Sedimentation equilibrium experiments carried out at the same concentrations could not be fitted to one single homogeneous species. Experimental data fitted well to a model containing more than one state (no uniform distribution of residuals) (Figure 36).

The results of both experiments are consistent with the existence of dimer-tetramer equilibrium in solution.

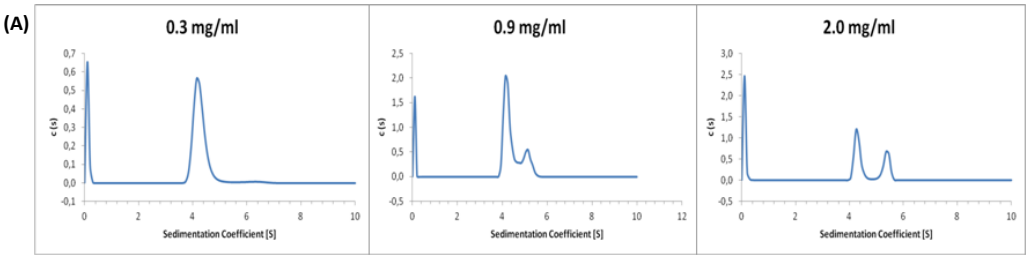

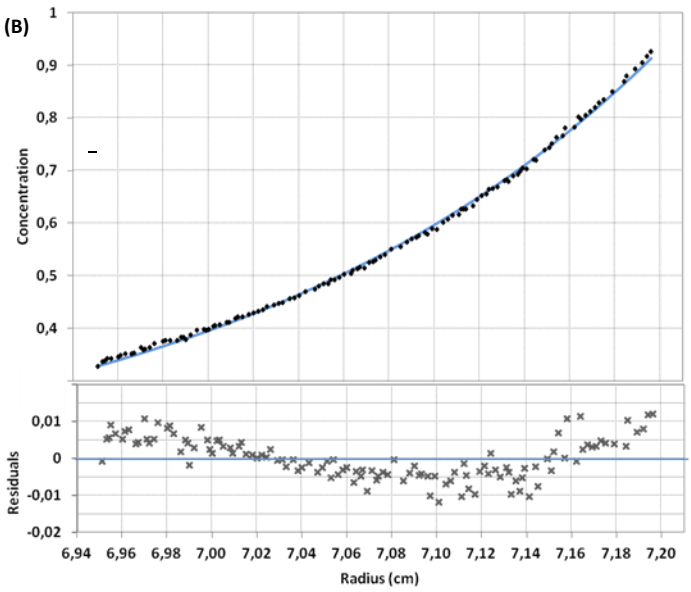

mg/ml	MW
0.3	71.700±1000
0.9	74.400±1000
2.0	74.500±1000

Figure 36: Analytical ultracentrifugation experiments of aMBL-2. (A) Sedimentation velocity profiles at the indicated protein concentrations. (B) Sedimentation equilibrium experiment of aMBL-2. The residuals (lower panel) show the non-uniform fitting between the experimental data and an ideal single-species model (blue line).

5. Protein crystallization

Initial crystallization assays were carried out by the sitting drop vapor diffusion method using sparse matrix crystallization screens at 22 °C [151]. The protein used for crystallization was in 50 mM Tris-HCl, buffered at pH 7.5, containing 100 mM NaCl and 1 mM DTT at 20 mg/ml with drops of 0.2 + 0.2 µl (protein + reservoir solution). Only one condition from the commercial crystallization kits produced crystals (B12 CUSTOM I, 19.43 % PEG-MME 2K, 10 mM EDTA and 0.68 % BOG). Further optimization of this condition (12 % PEG-MME 2K, 12 mM EDTA and 0.68 % BOG) gave quality diffracting crystals with an approximate final size of 400 x 100 x 100 µm (Figure 37).

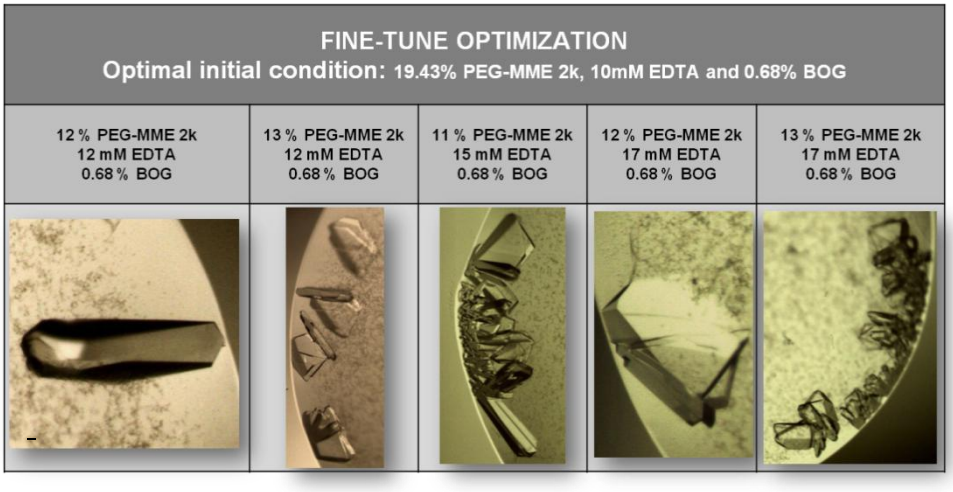

Figure 37: Crystals of aMBL-2 obtained with the optimized crystallization solution.

6. Structure determination

6.1. NATIVE DATASETS

6.1.1. DATA COLLECTION AND PROCESSING

One native dataset was collected on ID14.4 beamline at the ESRF (Grenoble, France) at cryogenic temperatures. Crystals were cryoprotected with 15% PEG 400 in the crystallization condition. Crystals of aMBL-2 belong to the triclinic space group P1 and diffracted up to 2.2 Å. The unit cell contains four molecules per asymmetric unit as derived from self rotation function (Figure 38) and an estimation of the solvent content. Data collection statistics are summarized in Table 12.

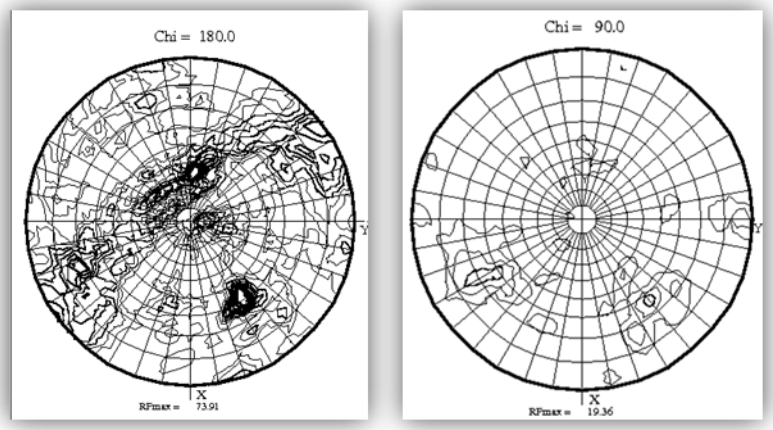

Figure 38: Self Rotation function at Chi = 180° and 90° calculated for the P1 native data of aMBL-2. Two peaks at Chi = 180° and no peaks at Chi = 90° suggested the presence of a dimer of dimers.

As for the first protein aMBL-1, no solution could be found using the molecular replacement method to solve the phase problem. Because of this SeMet labeled protein was produced, crystallized and X-ray diffraction data collected for this protein.

6.2. DERIVATIVE DATASETS

6.2.1. DATA COLLECTION AND PROCESSING

Diffraction data of the aMBL-2 SeMet labeled crystals were collected at ID14.4 (ESRF, Grenoble, France). The experimental wavelengths for the peak, inflection and remote were chosen based on the X-Ray fluorescence scan of the crystal (Figure 39).

Energy (eV)	f´	f´´
12.6597	-7.79	5.13
12.6577	-9.30	3.23

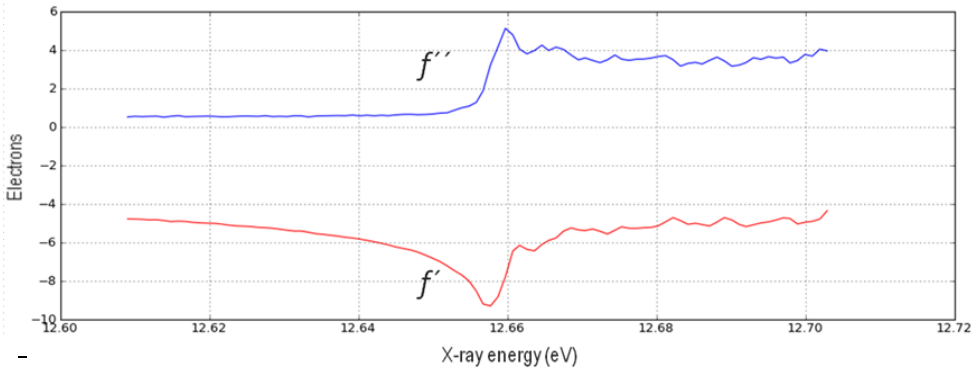

Figure 39: Experimental anomalous scattering from a crystal of Se-Met labeled aMBL-2. The f'' (blue curve) is proportional to the atomic absorption coefficient for a given element at a given energy. Dispersive difference between data is proportional to the difference in f' (red curve).

A highly redundant peak dataset of the SeMet labeled crystal was collected (Figure 40). After collecting this dataset, most likely, the crystal suffered from radiation damage and no more data could be collected. Data collection statistics are summarized in Table 12.

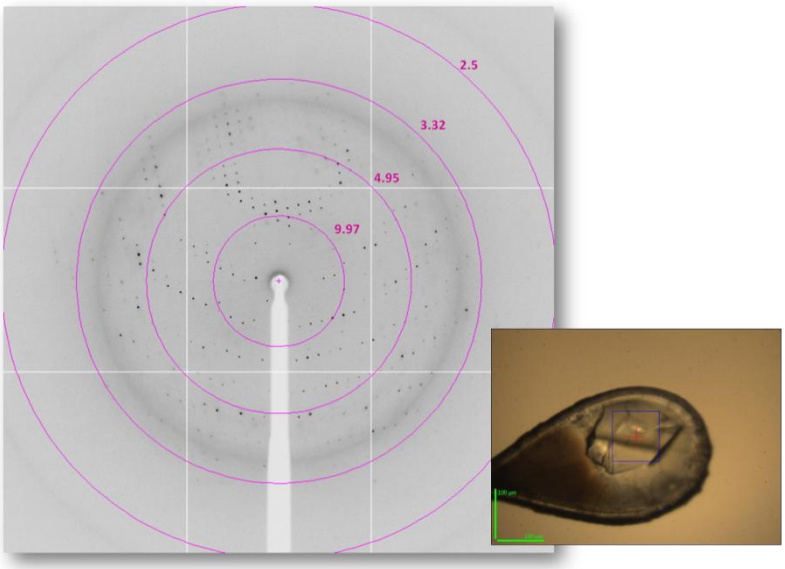

Figure 40: Diffraction pattern of the SeMet labeled triclinic crystal of aMBL-2.

Table 12: Data collection statistics for aMBL-2		
	SeMet-peak	NATIVE
X-ray source	ESRF/ID14.4	
X-ray detector	Q315r ADSC CCD	
Resolution range (last shell) (Å)	48.23 – 2.97 (3.13 – 2.97)	50.0 - 2.30 (2.42 – 2.30)
Number of images	360	
Oscillation range (°)	1.0	
Exposure Time (s)	0.1	
Wavelength (Å)	0.9794	0.9393
Space group	P1	
a, b, c (Å)	59.84, 64.82, 69.07	59.99, 64.56, 69.46
α, β, γ (°)	81.92, 81.65, 75.87	82.10, 81.35, 75.88
Matthews coefficient (Å3 Da^{-1})	2.13	2.14
Solvent content (%)	42.27	42.50
Molecules in the asymmetric unit	4	
Number of observations	151955 (18435)	159316 (23764)
Unique reflections	19842 (2830)	40985 (6084)
Completeness (%)	97.4 (94.6)	92.9 (94.8)
Multiplicity	7.7 (6.5)	3.9 (3.9)
Anomalous completeness	96.4 (93.0)	-
Anomalous multiplicity	3.8 (3.3)	-
R meas [a]*	0.090 (0.522)	0.060 (0.465)
R pim [b]*	0.046 (0.282)	0.030 (0.234)
Mean I/σ(I) [c]*	17.6 (3.5)	15.19 (3.0)
Anomalous signal+	1.33	-
Figure of merit+	0.46	-
Phasing power+	2.07	-

[a] R_{meas} = {Σhkl [N/(N-1)]1/2 Σ_i $|I_i(hkl) - \langle I(hkl)\rangle|$}Patte / Σhkl Σi $I_i(hkl)$, where $I_i(hkl)$ are the observed intensities, <I(hkl)> are the average intensities and N is the multiplicity of reflection hkl; [b] R_{pim} = Σ √(1/n-1) | $I_{hl} - \langle I_h\rangle$| / Σ | $\langle I_h\rangle$|; [c] [I/σ(I)] is the relation between the intensity of the diffraction and the background; *Values in parentheses are for the highest resolution shell. [+] Values at 3.0 Å resolution.

6.3. STRUCTURE DETERMINATION AND REFINEMENT

The anomalous difference Patterson map [152] calculated for the SeMet labeled dataset is shown in Figure 41. At least, several high intensity peaks could be detected this way coming from cross-vectors between different heavy-metal sites.

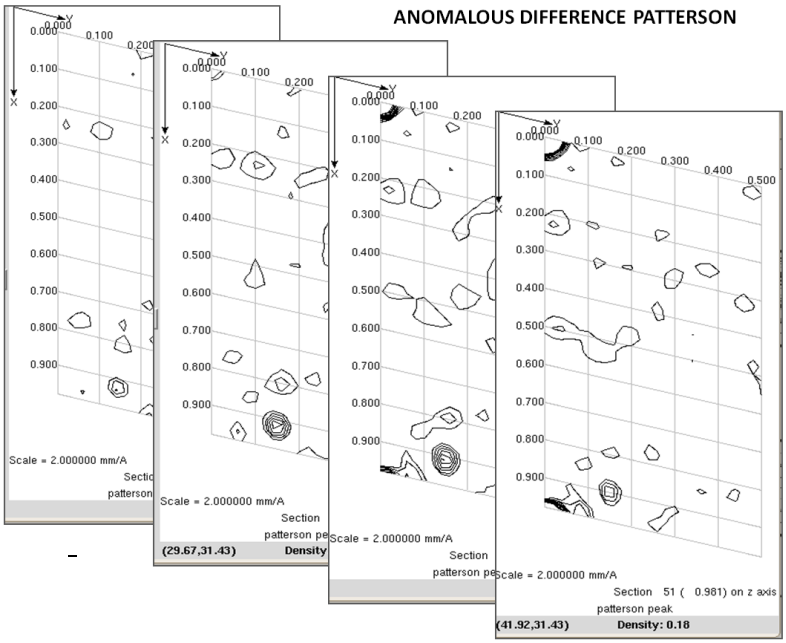

Figure 41: Sections of the anomalous difference Patterson map calculated for the peak data of the SeMet labeled aMBL-2 crystal.

The phases needed to solve the structure were calculated using the peak dataset from the SeMet labeled crystal by SAD. Initial positions for heavy atom sites were calculated with the program SHELX, and these positions were the input for the program SHARP. Twenty Se sites (Table 13) were used for phasing and an initial map at 3.0 Å was obtained as the final output of the program SHARP. These initial phases were extended up to 2.3 Å using the native dataset.

Table 13: Final coordinates and occupancies of the Se atoms

	(fractional coordinates)			
Se atom	x	y	z	Occupancy
1	-0.0041	1.2641	0.0745	1.2681
2	-0.0020	1.1110	0.0827	1.1129
3	-0.0020	1.4074	0.1211	1.4093
4	-0.0015	1.4759	0.0917	1.4774
5	-0.0031	1.0084	0.0853	1.0114
6	0.0003	1.0479	0.0871	1.0476
7	0.0005	1.2429	0.0759	1.2424
8	-0.0020	1.2251	0.1159	1.2271
9	0.0019	0.9507	0.0821	0.9488
10	-0.0003	1.1225	0.0955	1.1228
11	0.0041	1.0073	0.0918	1.0032
12	0.0019	0.8186	0.0827	0.8167
13	0.0028	0.6666	0.0854	0.6638
14	0.0010	0.4197	0.0637	0.4187
15	-0.0007	0.6120	0.1089	0.6126
16	-0.0035	0.6606	0.1262	0.6641
17	0.0006	0.3967	0.0891	0.3961
18	0.0094	0.8201	0.1786	0.8106
19	0.0064	0.5543	0.1103	0.5479
20	-0.0011	0.2920	0.0506	0.2931

An initial model of the content of the asymmetric unit was obtained with the program AUTOBUILD implemented in the PHENIX suite [121] using the initial phases (in form of Hendrickson-Lattman coefficients) obtained with the program SHARP.

The final model was optimized in an iterative process of refinement and manual model building. The refinement statistics are shown in Table 14.

Table 14: Refinement analysis of aMBL-2

Space group	P1
Resolution (Å)	2.3
No. reflections	40591
R_{work}[a] (R_{free}[b]) (%)	28.57 (32.72)
Number of atoms	
Protein	6358
Water	12
Zinc	4
R.m.s.d.[c]	
Bond length (Å)	0.009
Bond angles (°)	1.386
B factor (Å²)	
Protein (main/side chain)	73.88/73.79
Solvent	59.36

6.4. VALIDATION OF THE STRUCTURE

The final aMBL-2 structure contains four molecules in the asymmetric unit together with 12 water molecules and four zinc ions.

The final model was checked for errors using the MolProbity server [123]. The structure has for this resolution acceptable geometry with the fourth molecule (molecule D) in the asymmetric unit highly disordered. The electron density is weakest for this molecule as well as for some disordered long loop regions (Figure 46).

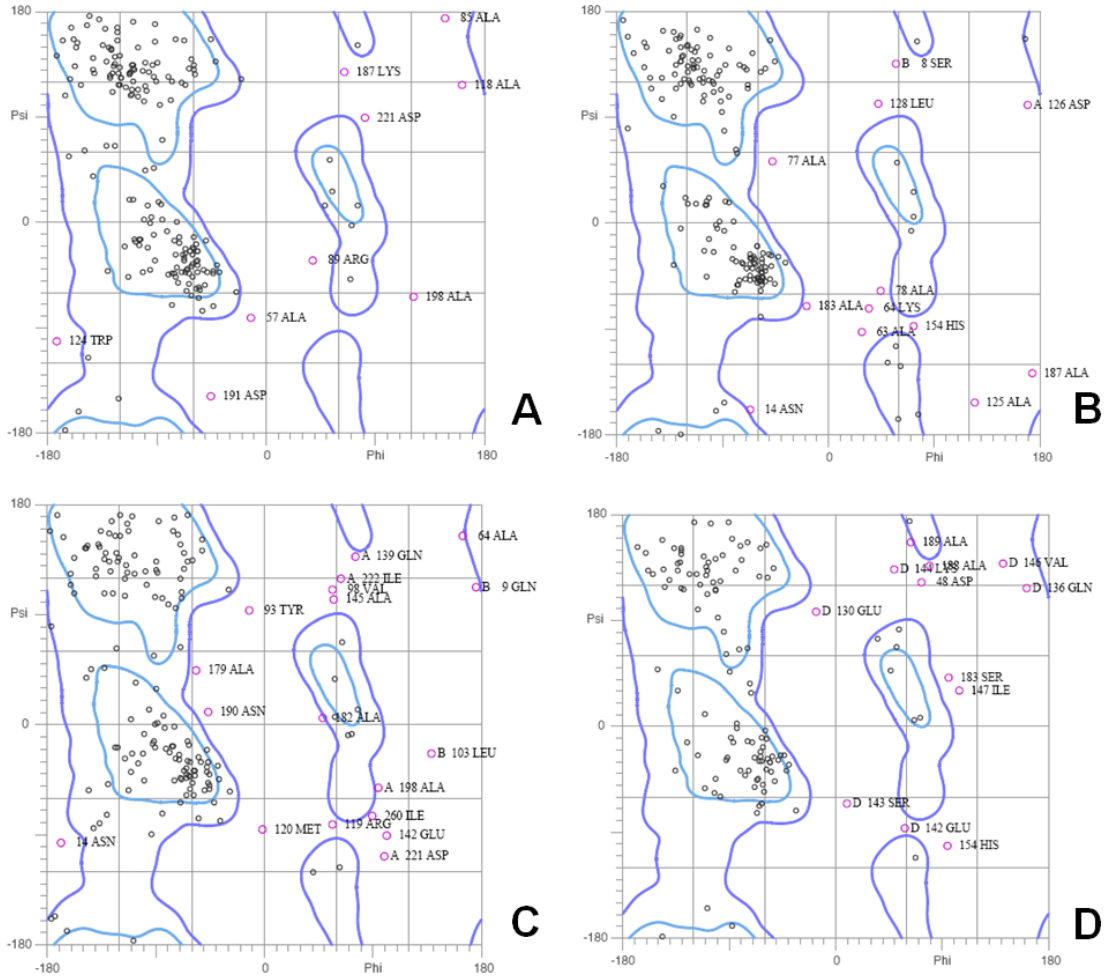

Figure 42: Ramachandran plot for each chain (A, B, C and D) of aMBL-2. The structure has for this resolution acceptable geometry. Molecule A has 95.9 % of all residues in allowed regions; molecule B has 93.8 %; molecule C has 90 % and molecule D has 90 %.

7. Architecture of aMBL-2

7.1. OVERALL FOLDING

The monomer of aMBL-2 has an almost globular shape (Figure 43a) with approximate dimensions of 55 x 45 x 30 Å. The overall structure exhibits the typical αβ/βα fold for members of the MBL superfamily [60, 63] (Figure 43a), with a central core of two facing β-sheets, composed of seven (A1-A7) and six β-strands (B1-B6), respectively, and surrounded by five solvent exposed α-helices (α1 (Ala56-Leu62), α2 (Trp90-Ala93), α3 (Phe199-Tyr203) α4 (Asn207-Arg218) and α5 (Lys236-Glu247)). The first β-sheet, labeled as A, is formed by β-strands A1 (from residue Leu11 to Asp13), A2 (His17-Thr23), A3 (Asn34-Asp40), A4 (Arg43-Ile47), A5 (Leu71-Met75), A6 (Val98-Lys102) and A7 (Leu128-Leu131), while the second, labeled as B, includes β-strands B1 (Gln136-Leu140), B2 (Ser143-Pro149), B3 (Phe159-Asp163), B4 (Ile168-Gly172), B5 (Met224-Pro227) and B6 (Phe233-Gly235). Both β-sheets have mixed parallel (A4, A5, A6 and A7; B4 and B5) and antiparallel (A1, A2 and A3; B1, B2, B3 and B6) β-strands.

Four of the five α-helices are packed parallel against each other, flanking both faces of the β-sandwich at the N- (α1-α2) and C-terminal (α4-α5) regions, respectively. A fifth helix, α3, runs parallel to the second β-sheet and sits close to the floor of the active site, that lies at the interface of the two β-sheets.

Both β-sheets are linked on one side by β-strands A2 and B5 mainly by hydrogen bond interactions, whereas on the other side β-strands A6 and B2 are connected by a tight packing of hydrophobic residues. Moreover, long connections between adjacent strands of the β-sheet as well as part of the loop covering the active site are disordered. The main gaps are found between His78 and Ile 84 (Gap I), that corresponds with a small helix described in other related β-lactamases and bringing one of the catalytic residues (Asp80). Gap II corresponds to a solvent exposed region also near to the active site between residues Leu103 and Ser117, and finally, Gap III is located between residues Val179-Pro185 in a region connecting β-strand B4 with helix α3. For clarity, the connectivity between these structure elements is shown in Figure 43b, where each α-helix and β-strand is numbered sequentially.

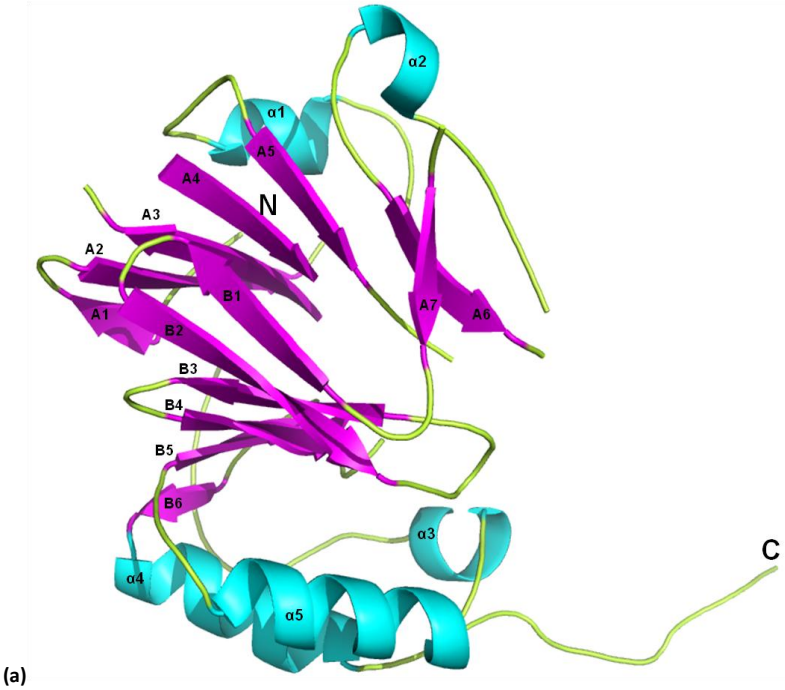

(a)

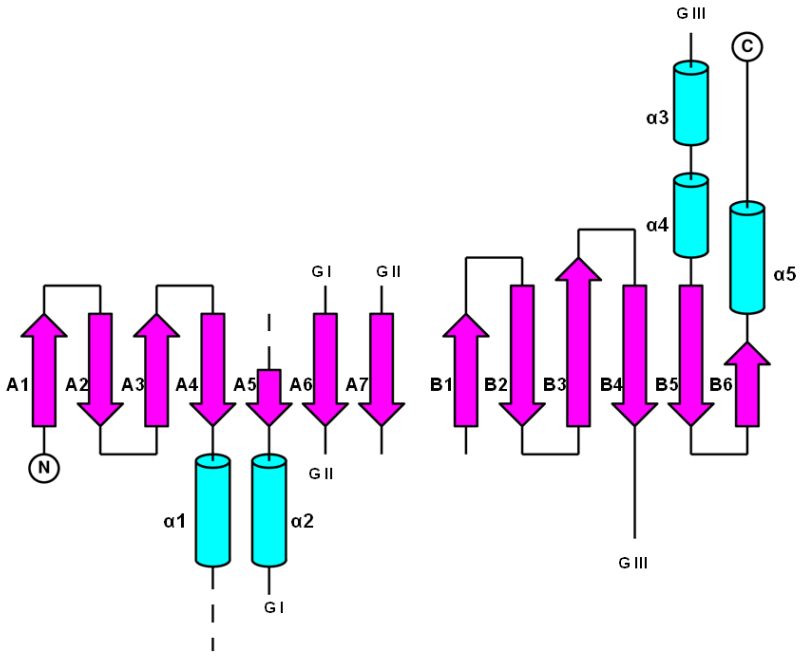

(b)

Figure 43: Structure of aMBL-2. (a) Ribbon diagram of the aMBL-2 monomer. (b) Topological diagram of the structure of aMBL-2. Secondary structure elements are labelled according to their position in the primary sequence, also the N and C termini are labelled as N and C, respectively. α-helices are shown as cyan and β-strands as pink arrows. GI, GII and GIII represents the different gaps in the aMBL-2 model.

7.2. ACTIVE SITE

The structure of aMBL-2 was obtained from crystallization conditions in the presence of EDTA, and we cannot exclude that metal-binding site is partially occupied. The high affinity metal binding site (site 1) as defined in other class B β-lactamases [63] was His-His-His (His84, His86 and His160 for *S. maltophilia* [153]).

Based on a superposition of several class B β-lactamases, allow the identification of two conserved histidines (His78 and His154) near the edge of the β-sandwich in a flexible loop region where some of the residues could not be properly traced (Figure 44). The third residue that would bind the metal ion is an aspartate (Asp80), a non conserved residue in the canonic metal binding motif (HXDXH/H) that could not be traced in the electron density due to the disorder.

The second low affinity metal binding site (site 2) could not be identified due to the high disorder at the region where it should be located.

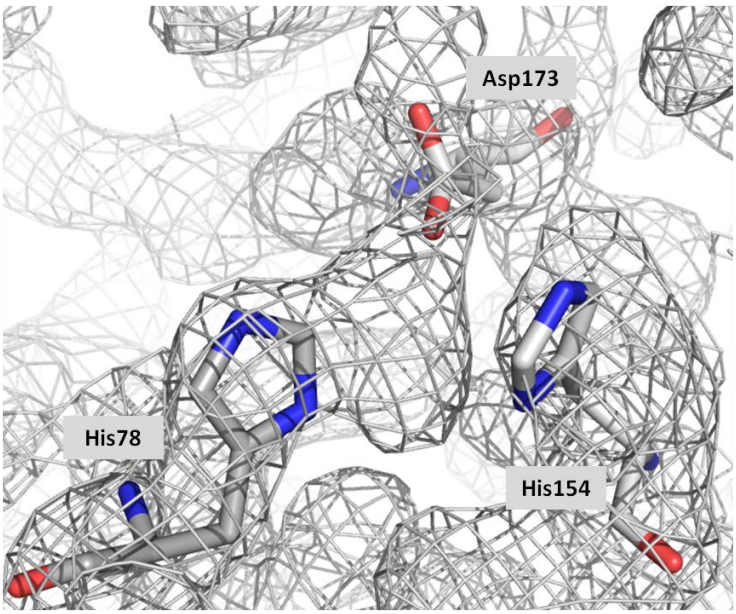

Figure 44: Electron density in the active site of aMBL-2 showing the 2Fo-Fc map (contoured at 1.2σ). Residues are drawn in ball-and-stick representation with oxygen, nitrogen, and carbon atoms shown in red, blue, and grey, respectively.

The superposition of the metallo-β-lactamase L1 from *S. maltophilia* with the aMBL-2 showed the two conserved histidines in a similar localization as in the canonical metal binding motif. The third histidine is replaced by an aspartate (Asp80) that could not be seen in the structure (Figure 45).

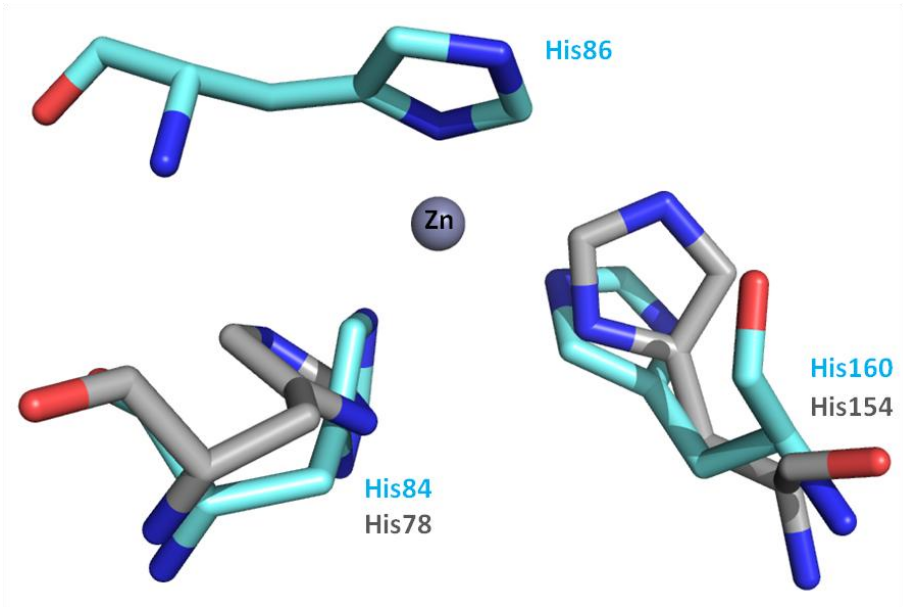

Figure 45: Superposition of the high affinity zinc binding site of L1 from *S. Maltophilia* (blue) and aMBL-2 (grey). Residues are drawn in ball-and-stick mode.

7.3. QUATERNARY STRUCTURE

The asymmetric unit of AMBL-2 has four molecules showing an oligomerisation state that could be associated to a dimer of dimers (Figure 46).

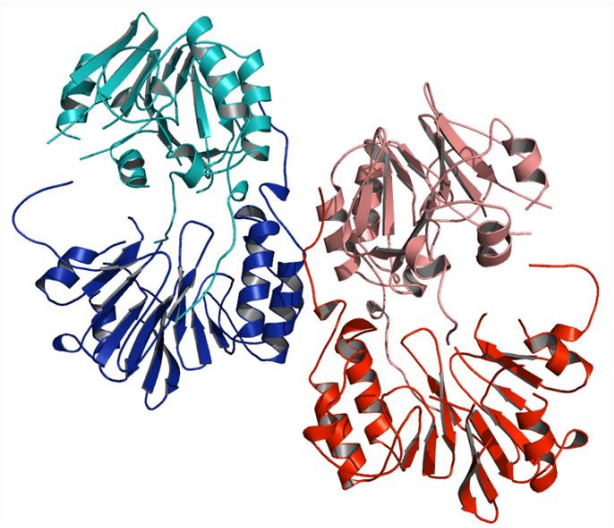

Figure 46: Quaternary structure of aMBL-2. Chain A, light blue; chain B, dark blue; chain C, red; chain D, pink.

The most striking interactions involve C-terminal residues of the two monomers of the dimer forming an extended U-shaped structure mutually stabilized by both electrostatic and hydrophobic contributions.

The dimerization area is formed by residues coming from the extended C-terminal arm of one monomer (Asp254, Met256, Glu258) with residues from the helix α4 of the second subunit (Lys208-Asn215), establishing predominantly hydrophobic interactions (Figure 47). At the end of the C-terminal region, there is a helix3-10 that also takes part of this main dimerization interface by connecting Ser262 and Gln259 with Arg134 from the second chain.

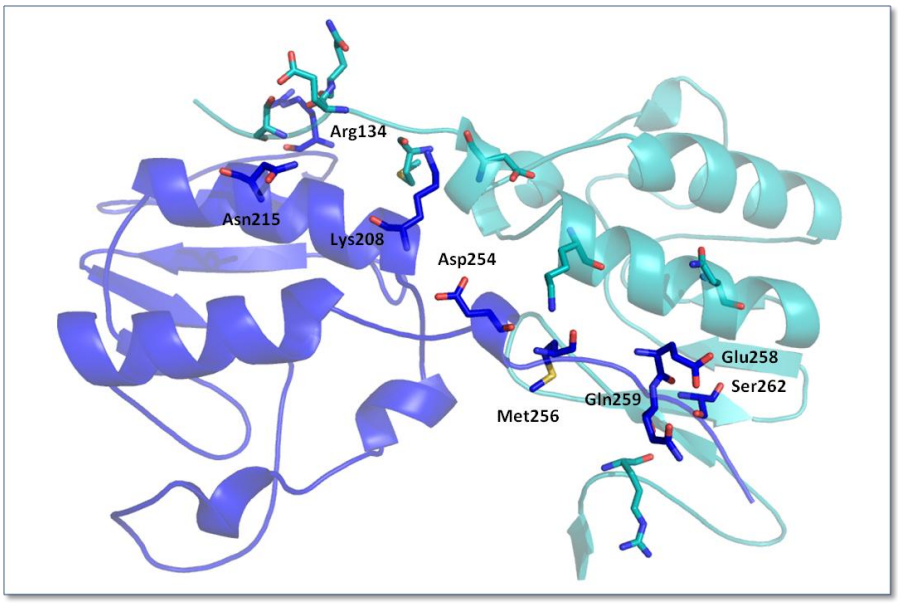

Figure 47: Zoom of the dimerization area between chains A (dark blue) and B (light blue). For clarity, only residues from chain A are labelled, but same residues participating in the interaction from chain B are also represented.

8. Functional assays

8.1. MICROBIOLOGICAL ASSAYS

Antibiotic degradation assays were carried out using *E.coli* DH5α by an adaptation of the Masuda method. As can be seen in Figure 48, E. coli cells were able to grow in the presence of OXA, a known class D β-lactamase [129], as well as aMBL-2 with no significant differences in the inhibition halo around the antibiotic disk.

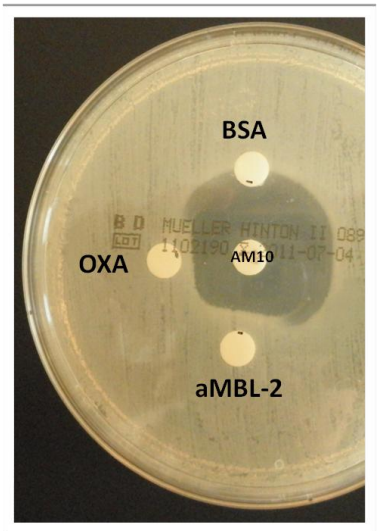

Figure 48: Antibiotic degradation assays by an adaptation of the Masuda method. Disks containing: OXA (45μg), (+) control (enzyme with well-known β-lactamase activity), BSA (45μg), (-) control (enzyme without β-lactamase activity) and aMBL-2 (45 μg) were placed around an ampicillin disk (AM10,10μg). Tests were performed with Mueller-Hinton agar and inoculums of 5 x10^5 *E. coli* DH5α cells/ml.

The susceptibility patterns of AMBL-2 are listed in Table 15. The aMBL-2 enzyme showed a low hydrolytic activity against most of β-lactams tested by E-tests, in comparison with others reported MBLs. The lowest concentration of the antibiotic that completely inhibited growth (recorded as the MIC) was only one or two dilutions higher relative to the control (empty pETRA vector).

Table 15: MICs of A. baumannii strains with cloned genes used in this work													
Strain	Construction	MIC (μg/ml)*											
		P	AM	PIP	CF	FOX	CXM	CAZ	CTX	FEP	IMP	MER	AZM
A.baylyi	pETRA	16	4	32	32	32	8	8	4	2	0.06	0.12	16
	pETRA + N14	16	8	32/256+°	32	64	16	8	8	4+	0.25+	0.12	32
A.baumannii ATCC 17978	pETRA	32	32	64	256	128	256	16	32	4	0.25	0.25	32
	pETRA + N14	32	64	128	512	256	256	16	32/256°	16	0.25	0.25	64

***P, penicillin; AM, ampicillin; PIP, piperacillin; CF, cephalothin; FOX, cefoxitin; CXM, cefuroxime CAZ, ceftazidime; CTX, cefotaxime; FEP, cefepime; IMP, imipenem; MER, meropenem; AZM, aztreonam.**
+ Isolated colonies growth within the zone of inhibition around the strip in E-test assays.
° Growth among next dilutions in broth microdilution method. Cut-off is dubious.

8.2. ENZYMATIC ACTIVITY

The kinetic parameters of aMBL-2 toward nitrocefin and selected antibiotics were investigated (Table 16).

aMBL-2 exhibits relatively low affinity constants (Km) values, similar to other class B β-lactamases [References], indicating a high affinity of aMBL-2, particularly to carbapenems but with a significantly reduced catalytic efficiency (Kcat/Km).

Table 16: Kinetic parameters of aMBL-2 against some β-lactams			
β-Lactam	Km (μM)		
Nitrocefin	68.31 ± 15.7		
	kcat (s^{-1})	Km (μM)	kcat /Km (mM^{-1} s^{-1})
Ampicillin	0.2284 ± 0.011	108.3 ± 6.0	2.109
Piperacillin	0.2839 ± 0.007	236.1 ± 28.7	12.025
Cefalotin	0.0325 ± 0.0013	229.55 ± 29.78	0.1416
Cefuroxime	ND	4208.90 ± 260.36	ND
Imipenem	6.28 E-09 ± 0.32	13.01 ± 0.304	5.827 E-07
Meropenem	ND	1.121 ± 0.104	ND

DISCUSSION

IV. DISCUSSION

The MBL superfamily constitutes a large and diverse group of proteins involved in a variety of biological functions. Their ubiquitous distribution over the three biological domains suggests their functional importance and the ancient origin of the family. Members of the MBL superfamily are characterized by a similar αββα sandwich fold with a conserved HXHXD/H motif in the active site coordinating one or two metal ions (preferentially zinc). This core domain represents the minimal structure needed for a functional protein. Besides this domain, members of this family present additional domains. These additional domains define the specificity of these members [37, 154].

From the genome of *Acinetobacter baumannii* AYE, the genes ABAYE3862 and ABAYE0164 were selected that encodes for two proteins belonging to the MBL superfamily. These two proteins were selected due to their singular metal-binding motif that differs from the canonical sequence [Reference].

These two genes, ABAYE3862 and ABAYE0164, were cloned from genomic DNA and their respective encoded proteins, aMBL-1 and aMBL-2, were biophysically and biochemically characterized as well as their 3D structure determined by X-ray crystallography.

CHAPTER 1: aMBL-1

The aMBL-1 amino acid sequence has a 99 % identity with a protein encoded by the A1S_2957 gene in *A. baumannii* ATCC 17978, which was identified by Hood *et al* as belonging to a global regulatory system that may contribute to the antibiotic resistance in this organism [8]. A subsequent screening with PCR confirmed the presence of the aMBL-1 gene in a large collection of pathogen strains isolated from different clinical sources, as well as in the non-pathogenic *Acinetobacter* ADP1 strains.

1. Overall fold

aMBL-1 has been crystallized in two different crystal forms, monoclinic and orthorhombic. Monoclinic crystals were obtained at pH 6.7 with crystallization conditions from a commercial kit and the orthorhombic crystal form with an optimized solution at pH 7.5. The structure was solved by MAD using an orthorhombic SeMet labeled crystal and refined against a high-resolution native data set at 1.9 Å resolution. Also, the structure was solved at 1.7 Å resolution in the monoclinic crystal lattice by molecular replacement using the orthorhombic aMBL-1 structure as search model.

Its structure exhibits a globular overall shape with the typical β-sandwich fold of the MBL superfamily that consists of two facing β-sheets composed of parallel and antiparallel β-strands, surrounded by seven solvent exposed α-helices (Figure 23, Results Chapter 1). An interesting feature of this structure is the presence of a longer C-terminal region built by two extra additional α-helices out of the MBL fold. These two helices close over a hydrophobic pocket where a ligand interpreted as benzoate that could be assigned as a putative substrate binding site.

2. Putative active site

Unlike most members of the MBL superfamily, aMBL-1 presented an unusual sequence motif made up by residues Tyr-X-Asp-X-Asp/His in the putative active center, where no metal atom was found. The electron density found at the putative active site could be interpreted as a water molecule. Some other reported members of this superfamily also differ from the canonical HXHXD/H motif. It is the case of the class B β-lactamases CphA (PDB 3iof) the most similar structure to aMBL-1, which is also showing an unusual coordination of the catalytically essential zinc ion (Figure 49).

The metal binding site of YcbL (PDB 2xf4), a member of the glyoxalase type II (GLX2) family, is also separate from the canonical sequence motif. The presence of a metal in YcbL is located at the active site being responsible for the catalytic activity of this protein [155].

Only two residues of the putative metal binding motif from aMBL-1 are conserved when compared two these two proteins described above. These are the His222 and Asp90. The other two residues that in CphA and YcbL are able to bind to metal ions, are not present in aMBL-1. They are substituted by Tyr91 and Ile181, two hydrophobic residues that would not coordinate any metal ion. These might explain the fact that no metal atoms have been identified at the putative active site, together with the lack of enzymatic activity for the assays performed in this study.

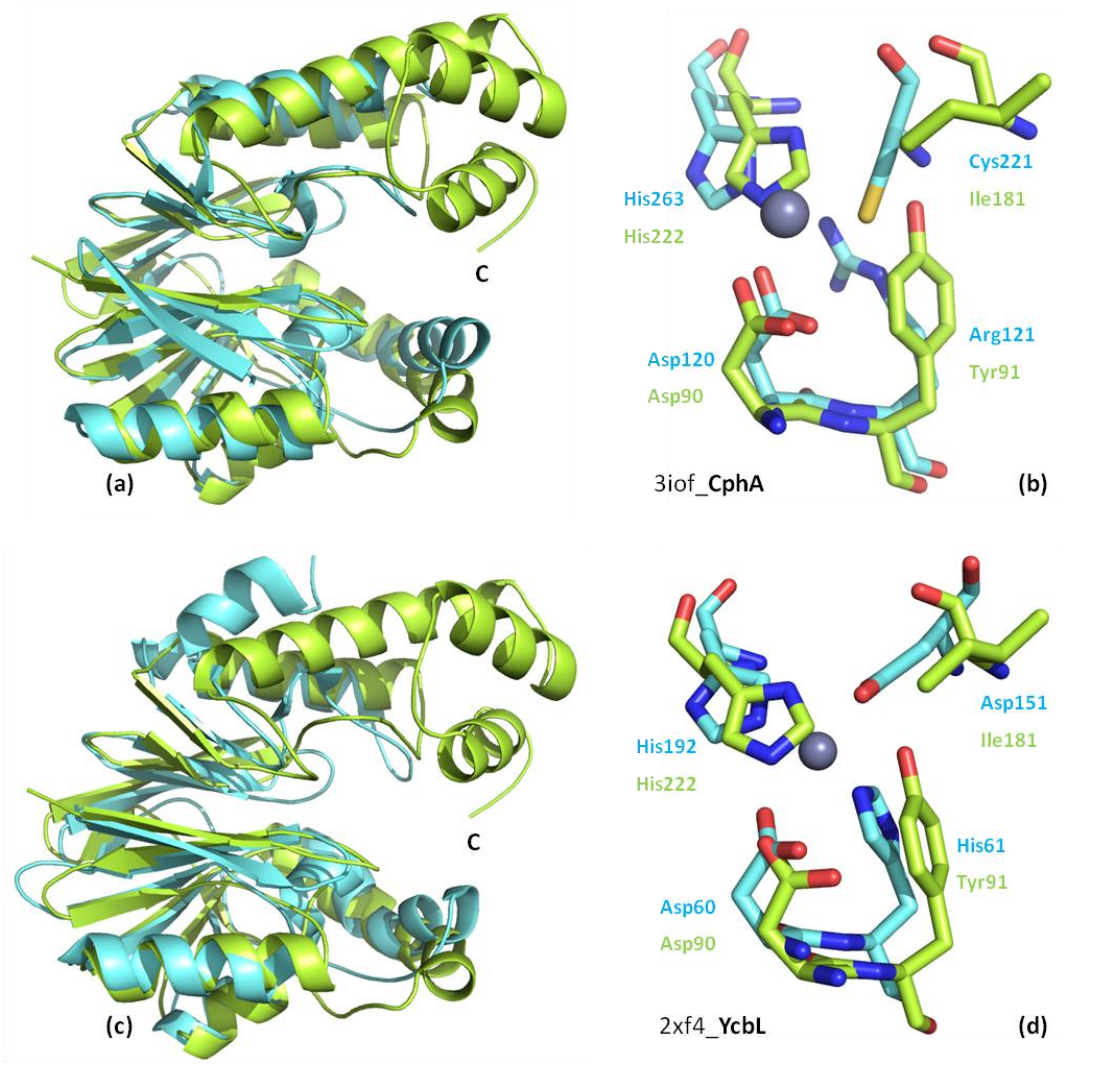

Figure 49: Structural alignment and superposition of the active site residues in the metal binding site. aMBL-1 (green), CphA (PDB ID 3iof; cyan) and YcbL (PDB ID 2xf4; cyan). Zinc ions are shown as grey spheres.

3. Putative binding site

Every structure of members of the MBL superfamily shows the substrate binding site located at the external edge of the β-sandwich, in an open cleft at the interface containing one or two metal ions coordinated through residues from the conserved motif HXHXD/H (Figures 5, 7, 8 and 9, Introduction) [61].

The electron density located close to the putative metal binding motif interpreted as a molecule of benzoate could represent the natural substrate-binding site of aMBL-1. The structure of one member of the MBL superfamily, PqsE, also contained a molecule interpreted as benzoate as a copurified ligand bound tightly to the iron atoms of the active site of this protein [36]. The possible role of this molecule is not supported by any experimental results, but they postulate a possible implication in the regulatory function of PqsE through a chorismate-derived molecule.

The binding mode of the benzoate molecule in aMBL-1 is different from that of PsqE. This might be due to the lack of metals, or it might represent the real binding mode of the possible substrate of aMBL-1 (Figure 27, Results Chapter 1).

Another common feature of these two proteins is the presence of tunnels that reach the active site (Figure 50). Yu *et al.* [36] postulated that the natural substrate of PqsE could be an elongated molecule due to the presence of these tunnels. In the case of aMBL-1 there is a continuous tunnel that crosses over the putative active site. The benzoate molecule is located in the middle of this tunnel, as in the case of PqsE, indicating also the possibility of an elongated substrate also for aMBL-1. These similarities together with the periplasmic location of the protein raises the possibility that it might acts as a sensor/regulator binding some molecule that might act as a signal for the bacterium not having any hydrolytic activity but acting as a transporter of the extracellular signal.

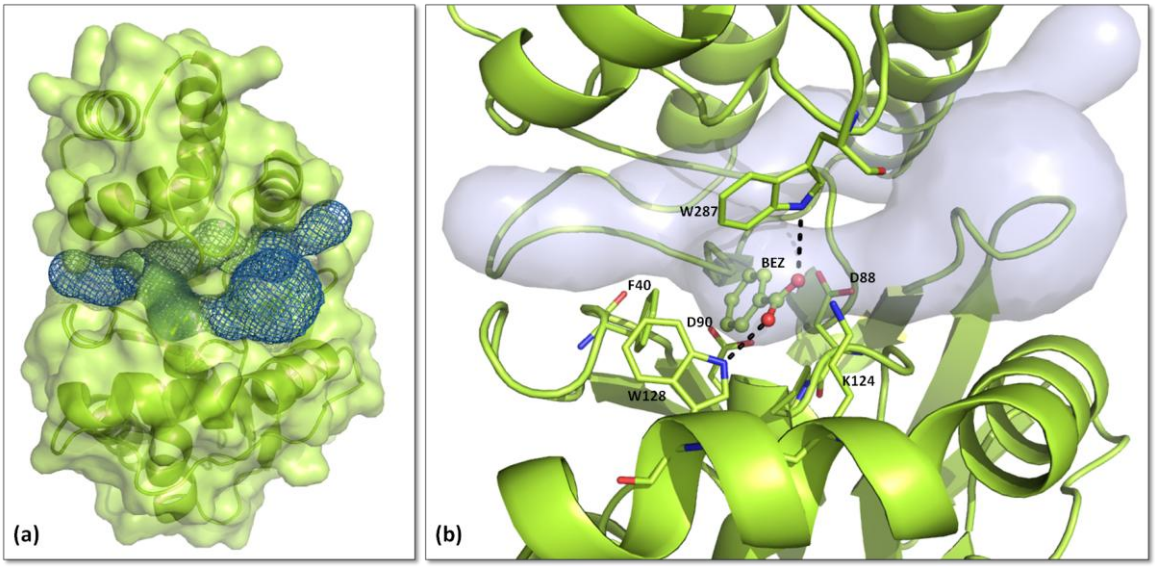

Figure 50: Tunnels at the putative binding site of aMBL-1. (a) Transparent surface representation of the aMBL-1 structure, with two tunnels shown as blue mesh. (b) Representation in sticks of the main residues from the hydrophobic pocket. The benzoate molecule is represented in ball-and-stick mode.

The structure of aMBL-1 might represent the closed form of the protein. The two C-terminal extra helices close over the entrance of the active site and the Trp, present at the penultimate position of the sequence, establish a bond with benzoate maintaining this close conformation.

4. Comparison with other members of the MBL superfamily / Classification

A search for similar structures deposited in the PDB data bank through DALI [156] showed, as expected, that aMBL-1 is similar to members of the MBL superfamily. The best hits are summarized in Table 17. Among those structures there are members of the class B β-lactamases, glyoxalase II family, an alkylsulfatase, a flavoprotein (rubredoxin) and two quinolone signal response protein (PqsE and ST1585).

Table 17: Best matches for AMBL-1 according to Dali

Name	PDB ID	Z score	rmsd	Description
Cph-A	3iof	21.1	2.7	MBL Subclass B2
SFH-1	3sd9	20.5	2.7	MBL Subclass B2
SPM-1	2fhx	19.1	2.6	MBL Subclass B1
BcII	1bmc	19.0	2.3	MBL Subclass B1
PqsE	2q0i	18.6	3.4	Quinolone signal response protein
NDM-1	3s0z	18.2	2.4	MBL Subclass B1
YcbL	2xf4	17.9	2.7	Glioxalase Type II
ST1585	3adr	17.6	3.3	Quinolone signal response protein
SDSA1	2cg2	15.8	3.3	Alkylsulfatase
ROO	1e5d	15.3	3.5	Rubredoxin: Oxygen oxidoreductase

The most similar structures, according to DALI, are members of the class B metallo-β-lactamases followed by other proteins that show unknown or different enzymatic activities. Despite this similarity, aMBL-1 presents shorter β-sheets compared to the metallo-β-lactamases, composed by five strands in the former while in the latter group they are composed, usually, by seven strands (Figure 49a).

The structural alignment of aMBL-1 with YcbL (Glioxalase type II) is shown in Figure 49c. The most significant differences are the connectivity of helix α3 with the N-terminal β-sheet, and the C-terminal helices. In this last case it can be observed that the YcbL presents two smaller helices that do not cover completely the C-terminal β-sheet whereas, in aMBL-1 there are four helices covering this sheet and also closing over the entrance of the putative active site.

The two helices of the C-terminal region of aMBL-1 is a feature not only present in this protein. It can be observed in, at least, two other members of the MBL superfamily, PsqE (the quinolone signal response protein from *Pseudomonas aeruginosa*, involved in a quorum sensing pathway) [36] and ST1585 from *Sulfolobus tokadaii* [157] that is present also in many other Archaea. In these two cases this feature is represented by two and one helices, respectively.

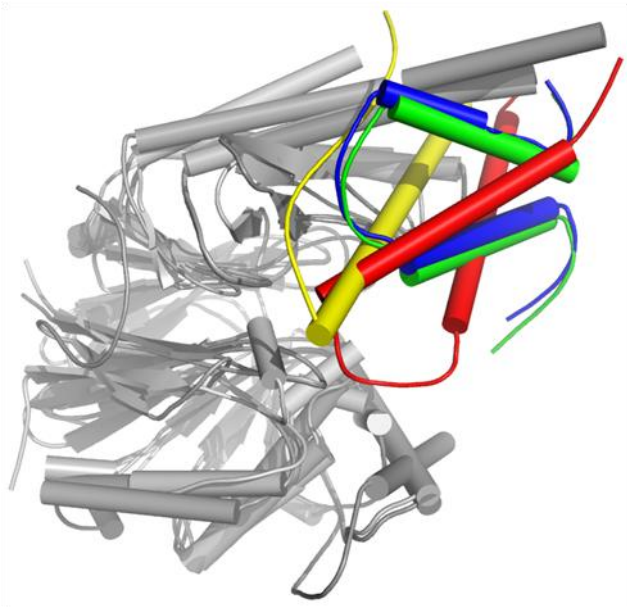

Figure 51: Structural alignment of aMBL-1 (blue, $P2_1$, and green, $P2_12_12_1$), PsqE (red), and ST1585 (yellow). The MBL domain is represented in grey and only the extra C-terminal helices are colored.

In these three protein types the C-terminal helices are located at the entrance of the active site. They do not show a similar orientation among these proteins, as can be seen in Figure 51, PsqE has two helices and ST1585 presents only one. The fact that in every case only one type of structure, the putative closed form, hampers the possible interpretation of the role of this C-terminal feature.

PqsE and ST1585 are placed into group 0 of the MBL superfamily, without any assigned function. The fact that aMBL-1 also presents the C-terminal feature and no known function has been assigned, yet, to this protein prompted us to, tentatively, classify the protein into the group 0 of the MBL superfamily.

The protein aMBL-2 showed some antibiotic degradation capability and also is most similar in overall fold and metal binding site motif to the metallo-β-lactamases. This data allow its classification as part of the class B subfamily of this type of enzymes.

1. Overall fold

The structure of aMBL-2 shows the typical metallo-β-lactamase αβ/βα sandwich fold. The two central facing β-sheets are composed by seven (A1-A7) and six strands (B1-B6), flanked by solvent exposed α-helices, two on each side (α1-α2 and α4-α5) packed in a parallel fashion. A fifth helix, α3, lies at the interface of the two β-sheets close to the catalytic site. The most characteristic difference with the well conserved topology of the metallo-β-lactamases is the presence of a C-terminal extension that embraces a second monomer forming a dimer that has been characterized by analytical gel filtration and analytical ultracentrifugation (see Results).

Most of the members of the class B metallo-β-lactamases are present as monomers in solution. Only β-lactamase L1 from *Stenotrophonomas maltophilia* showed a higher order of oligomerization, a tetramer in solution [153]. aMBL-2 has been found to be a dimer in solution, and the crystal structure shows an association that represents a dimer of dimers (Figure 46, Results).

The dimer arrangement of aMBL-2 has an U-shape that leaves the two active sites at the sides of the bottom of this U and separated by 17 Å (Figure 52A). This represents a new arrangement for this type of proteins and might influence the substrate selection. L1 from *S. maltophilia* shows a different mode of oligomerization showing a dimer of dimers where every monomer interacts with the other three members of the tetramer (Figure 52B). In L1 all the active sites are not related with each other pointing towards the external solvent region arranged in the four vertices of the square that define the tetramer. Also, this U-shape of the dimer might allow for opening-closing movements upon substrate binding, modifying the binding site in the process.

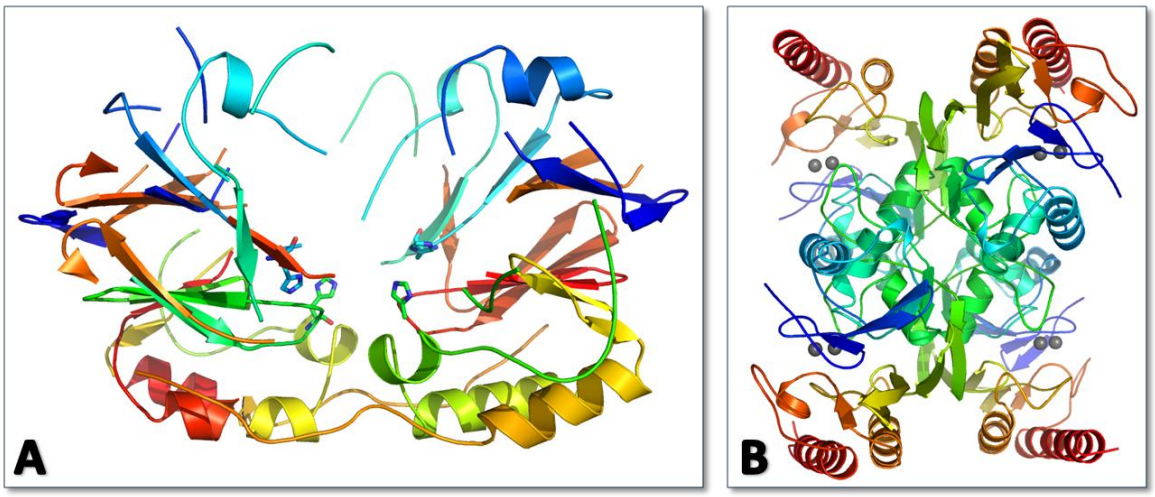

Figure 52: Ribbon representation of the quaternary structure of (A) aMBL-2 with residues at the putative active site represented in ball-and-sticks mode and (B) L1 with the zinc ions represented as grey spheres.

The crystal structure of aMBL-2 shows regions of the protein not well defined. One of these regions comprises one complete monomer of the four present in the asymmetric unit. Besides this fact, the regions with higher disorder might be related to the dimer organization. The arms of the U-shape that are composed by one βα side of the MBL fold are less defined, and this might support the opening-closing movements that might take place during catalysis.

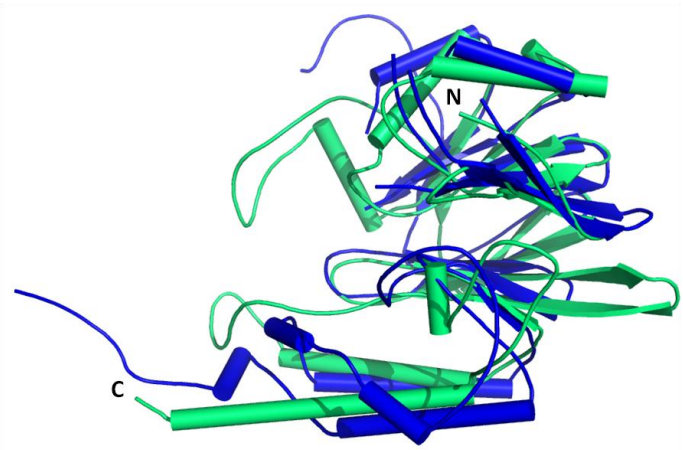

Figure 53: Structural alignment of the monomers of aMBL-2 (blue) and L1 (green).

The protein aMBL-2 showed a tendency to form tetramers with a dependency to the concentration, as seen by analytical ultracentrifugation. These data might explain the presence of a four monomers in the asymmetric unit arranged as a dimer of dimers. This oligomerization state (tetramer) might not be present *in vivo* due the high concentrations needed for its formation *in vitro*. Most likely the oligomerization state *in vivo* and the active form of the enzyme would be the dimer.

2. Putative active site

The residues involved in the binding of the first metal ion with high affinity of the metallo-β-lactamases is well conserved among the class B subfamily of these antibiotic degrading enzymes forming the so called canonical binding site (HXHXD/H). An inspection of the alignment of the possible residues from aMBL-2 that might constitute this site (H^{78}-X-D^{80}-X-D^{82}/H^{154}) showed the conservation of three of them with one substitution, H⇒D^{80} (Figure 54). The presence of this Asp in place of the canonical His should not hamper the binding of a catalytic metal at its binding site. The fact that no metal ion has been observed in the crystal structure might be a consequence of the presence of high concentration of the EDTA chelating agent in the crystallization condition, which might also explain the high degree of disorder observed at the metal binding site.

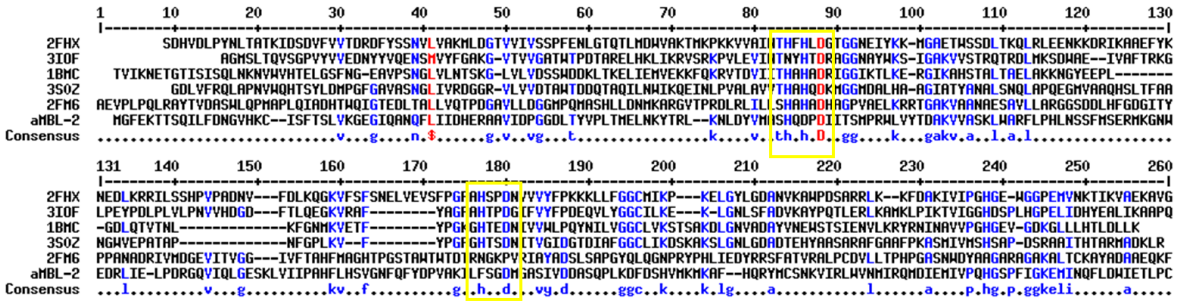

Figure 54: Sequence alignment of class B β-lactamase enzymes. SPM-1 from *P.aeruginosa* (2FHX), CphA from *Aeromonas hydrophila* (3IOF), BcII from *Bacillus cereus* (1BMC), NDM-1 from *Klebsiella pneumoniae* (3S0Z), L1 from *S. maltophilia* (2FM6) and aMBL-2 from *A. baumannii*. The yellow squares highlight the main residues from the metal ion binding site.

Enzymatic assays carried out with aMBL-2 showed its capability, although limited, to degrade β-lactam antibiotics. No high activity has been detected with this protein against the antibiotic tested. This might be due to the fact that we have not been able to find the appropriate substrate. In any case this measured activity indicates the presence of metal ions necessary for this type of enzymes to carry out its catalytic activity.

The two proteins of this study were selected using sequence information that allowed their classification as members of the MBL superfamily. Also, the differences in the canonical metal binding motif raised the curiosity of our laboratory. Due to the relation of these proteins a comparison of both structures will be presented.

1. *Overall fold*

A superposition of the structure of the monomers of aMBL-1 and aMBL-2 is presented in Figure 55. A general view shows that both proteins share the MBL fold typical of the superfamily. A closer look begins to highlight the differences.

The main differences that can be observed in the overall fold of these two proteins can be summarized as follows:

aMBL-1

The presence of an extra helix, $\alpha 3$, located sequentially between both sheets that forms like a floor for the active site, and the two extra helices located at the C-terminal closing over the putative active site.

aMBL-2

This protein presents two more strands in the sheet closer to the N-terminal, and a C-terminal extension that protrudes out of the core of the protein.

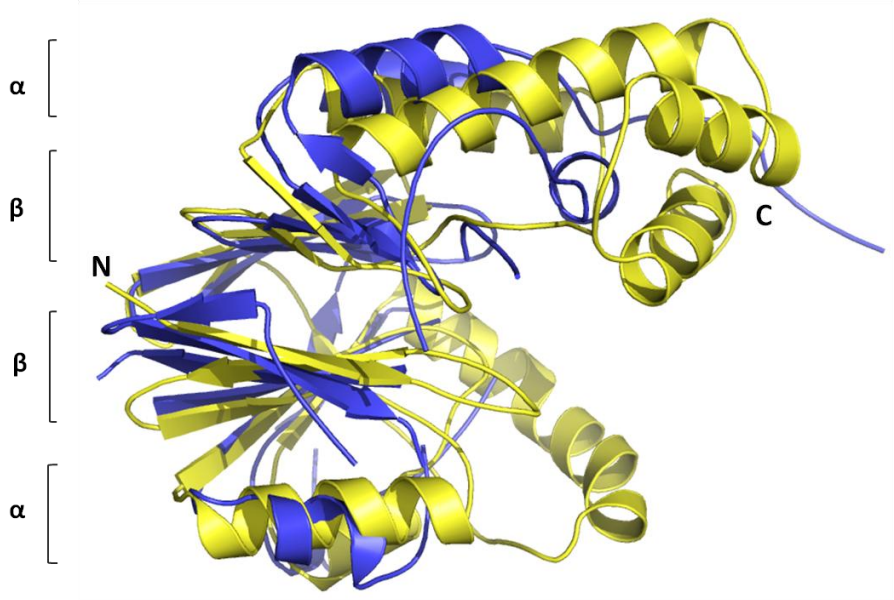

Figure 55: Structural alignment of the monomers of aMBL-1 (yellow) and aMBL-2 (blue).

2. *Dimerization*

Curiously both proteins aggregate forming dimers. A comparison of both types of dimers shows that very different regions of the protein are involved in each case. In the case of aMBL-1 the dimer interface is made up by the first two N-terminal helices that place the monomers in a back-to-back fashion with the active sites far from each other. In the case of aMBL-2 the dimer interface is made up by the C-terminal extension that embraces the neighboring monomer and leaves both active sites close to each other inside the U-shape of the final dimer.

3. Active site

The residues in the putative active sites of both proteins differ greatly. While aMBL-2 resembles the canonical metal binding motif of the metallo-β-lactamases, and most likely will bind a catalytic metal; aMBL-1 does not conserve most of the residues of this motif. Also, no metal could be defined in its structure indicating a different role *in vivo*, not depending on any catalytic to carry out its function, and serving as a transporter of some kind of signal.

CONCLUSIONES

CONCLUSIONES

- Hemos resuelto las estructuras tridimensionales de las proteínas aMBL-1 y aMBL-2 por cristalografía de rayos-X utilizando fases experimentales con cristales derivatizados con seleno-metionina. Ambas estructuras exhiben el típico plegamiento metallo-beta-lactamasa, que consiste en dos grupos centrales de láminas-beta flanqueados a ambos lados por hélices alfa expuestas al solvente.

- aMBL-1 presenta un dominio adicional formado por dos hélices alfa en la región C-terminal que cierran un bolsillo hidrofóbico dónde se localiza el sitio activo putativo.

- La comparación de la secuencia primaria de aMBL-1 con otros miembros de la superfamilia de las metallo-beta-lactamasas, nos indica la presencia de un motivo Tyr-X-Asp-X-Asp/His, diferente del motivo canónico de unión a metal descrito para esta familia. No se ha podido identificar ningún ión metálico en esta región, esencial para la catálisis de un gran número de reacciones dónde intervienen miembros de esta superfamilia.

- Se identificó una molécula de benzoato en la intersección de dos túneles que recorren la proteína hasta alcanzar el sitio putativo de unión a substratos. La identificación de moléculas análogas se ha descrito para PqsE.

- aMBL-1 comparte diversas similitudes estructurales con otras proteínas ya identificadas en la superfamilia de MBL's y que definen un nuevo grupo con función aún desconocida (grupo 0). Aunque no se ha determinado ninguna función específica para este grupo de proteínas, la localización periplasmática sugiere un posible papel como sensor/regulador mediante la unión a moléculas que pueden actuar cómo señales para la bacteria.

- aMBL-2 exhibe el plegamiento característico de las β-lactamasas de clase B, encontrándose en ella los elementos estructurales conservados en la superfamilia de las metalo-beta-lactamasas: un núcleo central formado por dos láminas beta, de siete y cinco hebras, respectivamente, y flanqueadas por ambos lados por hélices alfa.

- aMBL-2 presenta una alta afinidad por ampicillina, piperacillina y especialmente por carbapenémicos, aunque su capacidad de hidrólisis es baja. Esto podría ser debido al hecho de que aún no hemos sido capaces de encontrar el sustrato apropiado. En cualquier caso, la actividad β-lactamasa indica la presencia de iones metálicos necesarios para llevar a cabo la actividad catalítica.

- aMBL-2 se encuentra integrado en el genoma de varias especies del género *Acinetobacter*, pudiendo ser un reservorio para nuevos mecanismos de resistencia, debidos a la contínua evolución provocada por la presión antibiótica.

BIBLIOGRAPHY

1. Joly-Guillou, M.L., *Clinical impact and pathogenicity of Acinetobacter.* Clin Microbiol Infect, 2005. **11**(11): p. 868-73.
2. Perez, F., et al., *Global challenge of multidrug-resistant Acinetobacter baumannii.* Antimicrob Agents Chemother, 2007. **51**(10): p. 3471-84.
3. Giamarellou, H., *Treatment options for multidrug-resistant bacteria.* Expert Rev Anti Infect Ther, 2006. **4**(4): p. 601-18.
4. Peterson, L.R., *Squeezing the antibiotic balloon: the impact of antimicrobial classes on emerging resistance.* Clin Microbiol Infect, 2005. **11 Suppl 5**: p. 4-16.
5. McGowan, J.E., Jr., *Resistance in nonfermenting gram-negative bacteria: multidrug resistance to the maximum.* Am J Med, 2006. **119**(6 Suppl 1): p. S29-36; discussion S62-70.
6. Van Looveren, M. and H. Goossens, *Antimicrobial resistance of Acinetobacter spp. in Europe.* Clin Microbiol Infect, 2004. **10**(8): p. 684-704.
7. Rello, J. and E. Diaz, *Acinetobacter baumannii: a threat for the ICU?* Intensive Care Med, 2003. **29**(3): p. 350-1.
8. Hood, M.I., et al., *Acinetobacter baumannii increases tolerance to antibiotics in response to monovalent cations.* Antimicrob Agents Chemother, 2010. **54**(3): p. 1029-41.
9. Vallenet, D., et al., *Comparative Analysis of Acinetobacters: Three Genomes for Three Lifestyles.* PLoS One, 2008. **3**(3): p. e1805.
10. Adams, M.D., et al., *Comparative Genome Sequence Analysis of Multidrug-Resistant Acinetobacter baumannii.* Journal of Bacteriology, 2008. **190**(24): p. 8053-8064.

11. Rice, L.B., *Federal funding for the study of antimicrobial resistance in nosocomial pathogens: no ESKAPE.* J Infect Dis, 2008. **197**(8): p. 1079-81.
12. Danziger, L. and S. Pendland, *Bacterial resistance to beta-lactam antibiotics.* American Journal of Health-System Pharmacy, 1995. **52**(suppl 2): p. S3-S8.
13. Spratt, B.G., *Resistance to antibiotics mediated by target alterations.* Science, 1994. **264**(5157): p. 388-93.
14. McDowell, T.D. and K.E. Reed, *Mechanism of penicillin killing in the absence of bacterial lysis.* Antimicrob Agents Chemother, 1989. **33**(10): p. 1680-5.
15. Ghuysen, J.M., et al., *Penicillin and beyond: evolution, protein fold, multimodular polypeptides, and multiprotein complexes.* Microb Drug Resist, 1996. **2**(2): p. 163-75.
16. Goffin, C. and J.M. Ghuysen, *Multimodular penicillin-binding proteins: an enigmatic family of orthologs and paralogs.* Microbiol Mol Biol Rev, 1998. **62**(4): p. 1079-93.
17. Davies, J., *Bacteria on the rampage.* Nature, 1996. **383**(6597): p. 219-20.
18. Walsh, C., *Molecular mechanisms that confer antibacterial drug resistance.* Nature, 2000. **406**(6797): p. 775-781.
19. Heinemann, J.A., *How antibiotics cause antibiotic resistance.* Drug Discov Today, 1999. **4**(2): p. 72-79.
20. Bellido, F., J.C. Pechere, and R.E. Hancock, *Reevaluation of the factors involved in the efficacy of new beta-lactams against Enterobacter cloacae.* Antimicrob Agents Chemother, 1991. **35**(1): p. 73-8.
21. Wilke, M.S., A.L. Lovering, and N.C. Strynadka, *Beta-lactam antibiotic resistance: a current structural perspective.* Curr Opin Microbiol, 2005. **8**(5): p. 525-33.
22. Beveridge, T.J., *Structures of gram-negative cell walls and their derived membrane vesicles.* J Bacteriol, 1999. **181**(16): p. 4725-33.
23. Kuehn, M.J. and N.C. Kesty, *Bacterial outer membrane vesicles and the host-pathogen interaction.* Genes Dev, 2005. **19**(22): p. 2645-55.
24. Massova, I. and S. Mobashery, *Kinship and diversification of bacterial penicillin-binding proteins and beta-lactamases.* Antimicrob Agents Chemother, 1998. **42**(1): p. 1-17.
25. Fisher, J.F., S.O. Meroueh, and S. Mobashery, *Bacterial resistance to beta-lactam antibiotics: compelling opportunism, compelling opportunity.* Chem Rev, 2005. **105**(2): p. 395-424.
26. Frere, J.M., *Beta-lactamases and bacterial resistance to antibiotics.* Mol Microbiol, 1995. **16**(3): p. 385-95.
27. Poole, K., *Resistance to beta-lactam antibiotics.* Cell Mol Life Sci, 2004. **61**(17): p. 2200-23.
28. Livermore, D.M., *beta-Lactamases in laboratory and clinical resistance.* Clin Microbiol Rev, 1995. **8**(4): p. 557-84.
29. Ambler, R.P., *The structure of beta-lactamases.* Philos Trans R Soc Lond B Biol Sci, 1980. **289**(1036): p. 321-31.
30. Bush, K., G.A. Jacoby, and A.A. Medeiros, *A functional classification scheme for beta-lactamases and its correlation with molecular structure.* Antimicrob Agents Chemother, 1995. **39**(6): p. 1211-33.
31. Huovinen, P. and G.A. Jacoby, *Sequence of the PSE-1 beta-lactamase gene.* Antimicrob Agents Chemother, 1991. **35**(11): p. 2428-30.
32. Jaurin, B. and T. Grundstrom, *ampC cephalosporinase of Escherichia coli K-12 has a different evolutionary origin from that of beta-lactamases of the penicillinase type.* Proc Natl Acad Sci U S A, 1981. **78**(8): p. 4897-901.
33. Ouellette, M., L. Bissonnette, and P.H. Roy, *Precise insertion of antibiotic resistance determinants into Tn21-like transposons: nucleotide sequence of the OXA-1 beta-lactamase gene.* Proc Natl Acad Sci U S A, 1987. **84**(21): p. 7378-82.

34. Neuwald, A.F., et al., *Extracting protein alignment models from the sequence database.* Nucleic Acids Res, 1997. **25**(9): p. 1665-77.
35. Daiyasu, H., et al., *Expansion of the zinc metallo-hydrolase family of the beta-lactamase fold.* FEBS Lett, 2001. **503**(1): p. 1-6.
36. Yu, S., et al., *Structure Elucidation and Preliminary Assessment of Hydrolase Activity of PqsE, the Pseudomonas Quinolone Signal (PQS) Response Protein.* Biochemistry, 2009. **48**(43): p. 10298-10307.
37. Shimada, A., et al., *The first crystal structure of an archaeal metallo-β-lactamase superfamily protein; ST1585 from Sulfolobus tokodaii.* Proteins: Structure, Function, and Bioinformatics, 2010. **78**(10): p. 2399-2402.
38. Cricco, J.A. and A.J. Vila, *Class B beta-lactamases: the importance of being metallic.* Curr Pharm Des, 1999. **5**(11): p. 915-27.
39. Cameron, A.D., et al., *Crystal structure of human glyoxalase II and its complex with a glutathione thiolester substrate analogue.* Structure, 1999. **7**(9): p. 1067-78.
40. Chen, L., et al., *Rubredoxin oxidase, a new flavo-hemo-protein, is the site of oxygen reduction to water by the "strict anaerobe" Desulfovibrio gigas.* Biochem Biophys Res Commun, 1993. **193**(1): p. 100-5.
41. McDaniel, R., et al., *Engineered Biosynthesis of Novel Polyketides: actVII and actIV Genes Encode Aromatase and Cyclase Enzymes, Respectively.* Journal of the American Chemical Society, 1994. **116**(24): p. 10855-10859.
42. Fernandez-Moreno, M.A., et al., *Nucleotide sequence and deduced functions of a set of cotranscribed genes of Streptomyces coelicolor A3(2) including the polyketide synthase for the antibiotic actinorhodin.* J Biol Chem, 1992. **267**(27): p. 19278-90.
43. Bartel, P.L., et al., *Biosynthesis of anthraquinones by interspecies cloning of actinorhodin biosynthesis genes in streptomycetes: clarification of actinorhodin gene functions.* J Bacteriol, 1990. **172**(9): p. 4816-26.
44. Tavtigian, S.V., et al., *A candidate prostate cancer susceptibility gene at chromosome 17p.* Nat Genet, 2001. **27**(2): p. 172-80.
45. Jenny, A., H.P. Hauri, and W. Keller, *Characterization of cleavage and polyadenylation specificity factor and cloning of its 100-kilodalton subunit.* Mol Cell Biol, 1994. **14**(12): p. 8183-90.
46. Jenny, A., et al., *Sequence similarity between the 73-kilodalton protein of mammalian CPSF and a subunit of yeast polyadenylation factor I.* Science, 1996. **274**(5292): p. 1514-7.
47. Richter, D., E. Niegemann, and M. Brendel, *Molecular structure of the DNA cross-link repair gene SNM1 (PSO2) of the yeast Saccharomyces cerevisiae.* Mol Gen Genet, 1992. **231**(2): p. 194-200.
48. Dronkert, M.L., et al., *Disruption of mouse SNM1 causes increased sensitivity to the DNA interstrand cross-linking agent mitomycin C.* Mol Cell Biol, 2000. **20**(13): p. 4553-61.
49. Moshous, D., et al., *Artemis, a novel DNA double-strand break repair/V(D)J recombination protein, is mutated in human severe combined immune deficiency.* Cell, 2001. **105**(2): p. 177-86.
50. Dreisenkelmann, B., *Translocation of DNA across bacterial membranes.* Microbiological Reviews, 1994. **58**(3): p. 293–316.
51. Solomon, J.M. and A.D. Grossman, *Who's competent and when: regulation of natural genetic competence in bacteria.* Trends Genet, 1996. **12**(4): p. 150-5.
52. Gosink, K.K., et al., *Role of novel choline binding proteins in virulence of Streptococcus pneumoniae.* Infect Immun, 2000. **68**(10): p. 5690-5.
53. Vollmer, W. and A. Tomasz, *Identification of the teichoic acid phosphorylcholine esterase in Streptococcus pneumoniae.* Mol Microbiol, 2001. **39**(6): p. 1610-22.

54. Metcalf, W.W. and B.L. Wanner, *Mutational analysis of an Escherichia coli fourteen-gene operon for phosphonate degradation, using TnphoA' elements.* J Bacteriol, 1993. **175**(11): p. 3430-42.
55. Schlenzka, W., et al., *CMP-N-acetylneuraminic acid hydroxylase: the first cytosolic Rieske iron-sulphur protein to be described in Eukarya.* FEBS Lett, 1996. **385**(3): p. 197-200.
56. Komatsu, T., et al., *Molecular characterization of an Enterobacter cloacae gene (romA) which pleiotropically inhibits the expression of Escherichia coli outer membrane proteins.* J Bacteriol, 1990. **172**(7): p. 4082-9.
57. Davison, J., et al., *Cloning and sequencing of Pseudomonas genes determining sodium dodecyl sulfate biodegradation.* Gene, 1992. **114**(1): p. 19-24.
58. Tomasek, P.H. and J.S. Karns, *Cloning of a carbofuran hydrolase gene from Achromobacter sp. strain WM111 and its expression in gram-negative bacteria.* J Bacteriol, 1989. **171**(7): p. 4038-44.
59. Nikawa, J., P. Sass, and M. Wigler, *Cloning and characterization of the low-affinity cyclic AMP phosphodiesterase gene of Saccharomyces cerevisiae.* Mol Cell Biol, 1987. **7**(10): p. 3629-36.
60. Carfi, A., et al., *The 3-D structure of a zinc metallo-beta-lactamase from Bacillus cereus reveals a new type of protein fold.* EMBO J, 1995. **14**(20): p. 4914-21.
61. Bebrone, C., *Metallo-beta-lactamases (classification, activity, genetic organization, structure, zinc coordination) and their superfamily.* Biochem Pharmacol, 2007. **74**(12): p. 1686-701.
62. Aravind, L., *An evolutionary classification of the metallo-beta-lactamase fold proteins.* In Silico Biol, 1999. **1**(2): p. 69-91.
63. Crowder, M.W., J. Spencer, and A.J. Vila, *Metallo-beta-lactamases: novel weaponry for antibiotic resistance in bacteria.* Acc Chem Res, 2006. **39**(10): p. 721-8.
64. Wommer, S., et al., *Substrate-activated zinc binding of metallo-beta -lactamases: physiological importance of mononuclear enzymes.* J Biol Chem, 2002. **277**(27): p. 24142-7.
65. Roy, C., et al., *beta-Lactamases and susceptibility phenotypes to beta-lactam antibiotics in Escherichia coli strains.* J Antimicrob Chemother, 1992. **29**(5): p. 593-4.
66. Yang, Y.J. and D.M. Livermore, *Interactions of meropenem with class I chromosomal beta-lactamases.* J Antimicrob Chemother, 1989. **24 Suppl A**: p. 207-17.
67. Thornalley, P.J., *The glyoxalase system: new developments towards functional characterization of a metabolic pathway fundamental to biological life.* Biochem J, 1990. **269**(1): p. 1-11.
68. Richard, J.P., *Kinetic parameters for the elimination reaction catalyzed by triosephosphate isomerase and an estimation of the reaction's physiological significance.* Biochemistry, 1991. **30**(18): p. 4581-5.
69. McCoy, J.G., et al., *Structure of an ETHE1-like protein from Arabidopsis thaliana.* Acta Crystallogr D Biol Crystallogr, 2006. **62**(Pt 9): p. 964-70.
70. Vogel, A., et al., *ElaC encodes a novel binuclear zinc phosphodiesterase.* J Biol Chem, 2002. **277**(32): p. 29078-85.
71. Schiffer, S., S. Rosch, and A. Marchfelder, *Assigning a function to a conserved group of proteins: the tRNA 3'-processing enzymes.* EMBO J, 2002. **21**(11): p. 2769-77.
72. Minagawa, A., et al., *A novel endonucleolytic mechanism to generate the CCA 3' termini of tRNA molecules in Thermotoga maritima.* J Biol Chem, 2004. **279**(15): p. 15688-97.
73. Ezraty, B., B. Dahlgren, and M.P. Deutscher, *The RNase Z homologue encoded by Escherichia coli elaC gene is RNase BN.* J Biol Chem, 2005. **280**(17): p. 16542-5.
74. Vogel, A., et al., *The tRNase Z family of proteins: physiological functions, substrate specificity and structural properties.* Biol Chem, 2005. **386**(12): p. 1253-64.

75. Li de la Sierra-Gallay, I., O. Pellegrini, and C. Condon, *Structural basis for substrate binding, cleavage and allostery in the tRNA maturase RNase Z.* Nature, 2005. **433**(7026): p. 657-61.
76. Wanner, B.L., *Gene regulation by phosphate in enteric bacteria.* J Cell Biochem, 1993. **51**(1): p. 47-54.
77. Podzelinska, K., et al., *Structure of PhnP, a phosphodiesterase of the carbon-phosphorus lyase pathway for phosphonate degradation.* J Biol Chem, 2009. **284**(25): p. 17216-26.
78. Hove-Jensen, B., F.R. McSorley, and D.L. Zechel, *Physiological role of phnP-specified phosphoribosyl cyclic phosphodiesterase in catabolism of organophosphonic acids by the carbon-phosphorus lyase pathway.* J Am Chem Soc, 2011. **133**(10): p. 3617-24.
79. Hove-Jensen, B., et al., *Accumulation of intermediates of the carbon-phosphorus lyase pathway for phosphonate degradation in phn mutants of Escherichia coli.* J Bacteriol, 2010. **192**(1): p. 370-4.
80. Fuqua, C., M.R. Parsek, and E.P. Greenberg, *Regulation of gene expression by cell-to-cell communication: acyl-homoserine lactone quorum sensing.* Annu Rev Genet, 2001. **35**: p. 439-68.
81. Lin, Y.H., et al., *Acyl-homoserine lactone acylase from Ralstonia strain XJ12B represents a novel and potent class of quorum-quenching enzymes.* Mol Microbiol, 2003. **47**(3): p. 849-60.
82. Dong, Y.H., et al., *AiiA, an enzyme that inactivates the acylhomoserine lactone quorum-sensing signal and attenuates the virulence of Erwinia carotovora.* Proc Natl Acad Sci U S A, 2000. **97**(7): p. 3526-31.
83. Hagelueken, G., et al., *The crystal structure of SdsA1, an alkylsulfatase from Pseudomonas aeruginosa, defines a third class of sulfatases.* Proc Natl Acad Sci U S A, 2006. **103**(20): p. 7631-6.
84. Dong, Y.J., et al., *Crystal structure of methyl parathion hydrolase from Pseudomonas sp. WBC-3.* J Mol Biol, 2005. **353**(3): p. 655-63.
85. Dunlap, P.V. and S.M. Callahan, *Characterization of a periplasmic 3':5'-cyclic nucleotide phosphodiesterase gene, cpdP, from the marine symbiotic bacterium Vibrio fischeri.* J Bacteriol, 1993. **175**(15): p. 4615-24.
86. Xu, R.X., et al., *Atomic Structure of PDE4: Insights into Phosphodiesterase Mechanism and Specificity.* Science, 2000. **288**(5472): p. 1822-1825.
87. Francis, S.H., et al., *Zinc interactions and conserved motifs of the cGMP-binding cGMP-specific phosphodiesterase suggest that it is a zinc hydrolase.* J Biol Chem, 1994. **269**(36): p. 22477-80.
88. Callahan, S.M., N.W. Cornell, and P.V. Dunlap, *Purification and properties of periplasmic 3':5'-cyclic nucleotide phosphodiesterase. A novel zinc-containing enzyme from the marine symbiotic bacterium Vibrio fischeri.* J Biol Chem, 1995. **270**(29): p. 17627-32.
89. Girard, G. and G.V. Bloemberg, *Central role of quorum sensing in regulating the production of pathogenicity factors in Pseudomonas aeruginosa.* Future Microbiol, 2008. **3**(1): p. 97-106.
90. Dosselaere, F. and J. Vanderleyden, *A metabolic node in action: chorismate-utilizing enzymes in microorganisms.* Crit Rev Microbiol, 2001. **27**(2): p. 75-131.
91. Diggle, S.P., et al., *Functional genetic analysis reveals a 2-Alkyl-4-quinolone signaling system in the human pathogen Burkholderia pseudomallei and related bacteria.* Chem Biol, 2006. **13**(7): p. 701-10.
92. Dubern, J.F. and S.P. Diggle, *Quorum sensing by 2-alkyl-4-quinolones in Pseudomonas aeruginosa and other bacterial species.* Mol Biosyst, 2008. **4**(9): p. 882-8.
93. Calfee, M.W., J.P. Coleman, and E.C. Pesci, *Interference with Pseudomonas quinolone signal synthesis inhibits virulence factor expression by Pseudomonas aeruginosa.* Proc Natl Acad Sci U S A, 2001. **98**(20): p. 11633-7.

94. Fournier, P.E., et al., *Comparative genomics of multidrug resistance in Acinetobacter baumannii.* PLoS Genet, 2006. **2**(1): p. e7.
95. Bolton, E.T. and C.B. Mc, *A general method for the isolation of RNA complementary to DNA.* Proc Natl Acad Sci U S A, 1962. **48**: p. 1390-7.
96. Kaelin, W.G., Jr., et al., *Expression cloning of a cDNA encoding a retinoblastoma-binding protein with E2F-like properties.* Cell, 1992. **70**(2): p. 351-64.
97. Walker, P.A., et al., *Efficient and Rapid Affinity Purification of Proteins Using Recombinant Fusion Proteases.* Nat Biotech, 1994. **12**(6): p. 601-605.
98. Aranda, J., et al., *A rapid and simple method for constructing stable mutants of Acinetobacter baumannii.* BMC Microbiol, 2010. **10**: p. 279.
99. Sambrook, J., Russell, D.W., *Molecular cloning: a laboratory manual*. 2001, New York: Cold Spring Harbor Laboratory.
100. Hendrickson, W.A., J.R. Horton, and D.M. LeMaster, *Selenomethionyl proteins produced for analysis by multiwavelength anomalous diffraction (MAD): a vehicle for direct determination of three-dimensional structure.* EMBO J, 1990. **9**(5): p. 1665-72.
101. Rupp, B., *Biomolecular Crystallography: Principles, Practice, and Application to Structural Biology*. 2009, Garland Science: New York.
102. Doublie, S., ed. *METHODS IN ENZYMOLOGY*. Vol. 276. 1997. 523-530.
103. Schuck, P. and P. Rossmanith, *Determination of the sedimentation coefficient distribution by least-squares boundary modeling.* Biopolymers, 2000. **54**(5): p. 328-41.
104. Schuck, P., *Size-distribution analysis of macromolecules by sedimentation velocity ultracentrifugation and lamm equation modeling.* Biophys J, 2000. **78**(3): p. 1606-19.
105. Schuck, P., et al., *Size-distribution analysis of proteins by analytical ultracentrifugation: strategies and application to model systems.* Biophys J, 2002. **82**(2): p. 1096-111.
106. Cole, J.L., *Analysis of heterogeneous interactions.* Methods Enzymol, 2004. **384**: p. 212-32.
107. Jancarik, J., et al., *Crystallization and preliminary X-ray diffraction study of the ligand-binding domain of the bacterial chemotaxis-mediating aspartate receptor of Salmonella typhimurium.* J Mol Biol, 1991. **221**(1): p. 31-4.
108. Gonzalez, A., A.W. Thompson, and C. Nave, *Cryo-protection of protein crystals in intense x-ray beams.* Journal Name: Review of Scientific Instruments; (United States); Journal Volume: 63:1, 1992: p. Medium: X; Size: Pages: 1177-1180.
109. Doublie, S., *Preparation of selenomethionyl proteins for phase determination.* Methods Enzymol, 1997. **276**: p. 523-30.
110. Hendrickson, W.A., *Determination of macromolecular structures from anomalous diffraction of synchrotron radiation.* Science, 1991. **254**(5028): p. 51-8.
111. Leslie, A.G.W., *"Recent changes to the MOSFLM package for processing film and image plate data".* Joint CCP4 + ESF-EAMCB Newsletter on Protein Crystallography, 1992. **26**.
112. Collaborative, *The CCP4 suite: programs for protein crystallography.* Acta Crystallographica Section D, 1994. **50**(5): p. 760-763.
113. Potterton, E., et al., *A graphical user interface to the CCP4 program suite.* Acta Crystallogr D Biol Crystallogr, 2003. **59**(Pt 7): p. 1131-7.
114. Winn, M.D., et al., *Overview of the CCP4 suite and current developments.* Acta Crystallogr D Biol Crystallogr, 2011. **67**(Pt 4): p. 235-42.
115. French, S. and K. Wilson, *On the treatment of negative intensity observations.* Acta Crystallographica Section A, 1978. **34**(4): p. 517-525.
116. Kabsch, W., *Xds.* Acta Crystallogr D Biol Crystallogr, 2010. **66**(Pt 2): p. 125-32.
117. Diederichs, K., S. McSweeney, and R.B. Ravelli, *Zero-dose extrapolation as part of macromolecular synchrotron data reduction.* Acta Crystallogr D Biol Crystallogr, 2003. **59**(Pt 5): p. 903-9.

118. Evans, P., *Scaling and assessment of data quality.* Acta Crystallogr D Biol Crystallogr, 2006. **62**(Pt 1): p. 72-82.
119. Uson, I. and G.M. Sheldrick, *Advances in direct methods for protein crystallography.* Curr Opin Struct Biol, 1999. **9**(5): p. 643-8.
120. Vonrhein, C., et al., *Automated structure solution with autoSHARP.* Methods Mol Biol, 2007. **364**: p. 215-30.
121. Adams, P.D., et al., *PHENIX: a comprehensive Python-based system for macromolecular structure solution.* Acta Crystallographica Section D, 2010. **66**(2): p. 213-221.
122. Emsley, P., et al., *Features and development of Coot.* Acta Crystallographica Section D, 2010. **66**(4): p. 486-501.
123. Davis, I.W., et al., *MolProbity: all-atom contacts and structure validation for proteins and nucleic acids.* Nucleic Acids Research, 2007. **35**(suppl 2): p. W375-W383.
124. DeLano, W.L., ed. *The PyMol Molecular Graphics System*. ed. D. Scientific. 2002: San Carlos, CA, USA.
125. Kuznetsova, E., et al., *Enzyme genomics: Application of general enzymatic screens to discover new enzymes.* FEMS Microbiol Rev, 2005. **29**(2): p. 263-79.
126. Wang, Z., W. Fast, and S.J. Benkovic, *On the Mechanism of the Metallo-β-lactamase from Bacteroides fragilis†.* Biochemistry, 1999. **38**(31): p. 10013-10023.
127. McManus-Munoz, S. and M.W. Crowder, *Kinetic Mechanism of Metallo-β-lactamase L1 from Stenotrophomonas maltophilia†.* Biochemistry, 1999. **38**(5): p. 1547-1553.
128. Minasov, G., X. Wang, and B.K. Shoichet, *An ultrahigh resolution structure of TEM-1 beta-lactamase suggests a role for Glu166 as the general base in acylation.* J Am Chem Soc, 2002. **124**(19): p. 5333-40.
129. Santillana, E., et al., *Crystal structure of the carbapenemase OXA-24 reveals insights into the mechanism of carbapenem hydrolysis.* Proc Natl Acad Sci U S A, 2007. **104**(13): p. 5354-9.
130. Wayne, P., *Clinical and Laboratory Standards Institute. Performance standards for antimicrobial susceptibility testing.* 17th informational supplement, 2007.
131. Hunter, S., et al., *InterPro in 2011: new developments in the family and domain prediction database.* Nucleic Acids Research, 2012. **40**(D1): p. D306-D312.
132. Söding, J., A. Biegert, and A.N. Lupas, *The HHpred interactive server for protein homology detection and structure prediction.* Nucleic Acids Research. **33**(suppl 2): p. W244-W248.
133. Yamaguchi, Y., et al., *Crystallographic investigation of the inhibition mode of a VIM-2 metallo-beta-lactamase from Pseudomonas aeruginosa by a mercaptocarboxylate inhibitor.* J Med Chem, 2007. **50**(26): p. 6647-53.
134. Murphy, T.A., et al., *Crystal structure of Pseudomonas aeruginosa SPM-1 provides insights into variable zinc affinity of metallo-beta-lactamases.* J Mol Biol, 2006. **357**(3): p. 890-903.
135. Oke, M., et al., *The Scottish Structural Proteomics Facility: targets, methods and outputs.* J Struct Funct Genomics, 2010. **11**(2): p. 167-80.
136. Zhang, H. and Q. Hao, *Crystal structure of NDM-1 reveals a common β-lactam hydrolysis mechanism.* The FASEB Journal, 2011. **25**(8): p. 2574-2582.
137. Di Matteo, A., et al., *The O2-scavenging flavodiiron protein in the human parasite Giardia intestinalis.* J Biol Chem, 2008. **283**(7): p. 4061-8.
138. Marasinghe, G.P., et al., *Structural studies on a mitochondrial glyoxalase II.* J Biol Chem, 2005. **280**(49): p. 40668-75.
139. Frazao, C., et al., *Structure of a dioxygen reduction enzyme from Desulfovibrio gigas.* Nat Struct Biol, 2000. **7**(11): p. 1041-5.
140. Mount, D.W., *Using the Basic Local Alignment Search Tool (BLAST).* Cold Spring Harb Protoc, 2007. **2007**(7): p. pdb.top17-.

141. McGuffin, L.J., K. Bryson, and D.T. Jones, *The PSIPRED protein structure prediction server.* Bioinformatics, 2000. **16**(4): p. 404-405.
142. Linding, R., et al., *GlobPlot: Exploring protein sequences for globularity and disorder.* Nucleic Acids Res, 2003. **31**(13): p. 3701-8.
143. Juncker, A.S., et al., *Prediction of lipoprotein signal peptides in Gram-negative bacteria.* Protein Sci, 2003. **12**(8): p. 1652-62.
144. Slabinski, L., et al., *XtalPred: a web server for prediction of protein crystallizability.* Bioinformatics, 2007. **23**(24): p. 3403-5.
145. Chait, B.T., *Mass spectrometry--a useful tool for the protein X-ray crystallographer and NMR spectroscopist.* Structure, 1994. **2**(6): p. 465-7.
146. Colfen, H., et al., *The Open AUC Project.* Eur Biophys J, 2010. **39**(3): p. 347-59.
147. Murshudov, G.N., A.A. Vagin, and E.J. Dodson, *Refinement of macromolecular structures by the maximum-likelihood method.* Acta Crystallogr D Biol Crystallogr, 1997. **53**(Pt 3): p. 240-55.
148. Yao, J.-X., *On the application of phase relationships to complex structures. XVIII. RANTAN-random MULTAN.* Acta Crystallographica Section A, 1981. **37**(5): p. 642-644.
149. Painter, J. and E.A. Merritt, *Optimal description of a protein structure in terms of multiple groups undergoing TLS motion.* Acta Crystallogr D Biol Crystallogr, 2006. **62**(Pt 4): p. 439-50.
150. Janin, J., S. Miller, and C. Chothia, *Surface, subunit interfaces and interior of oligomeric proteins.* J Mol Biol, 1988. **204**(1): p. 155-64.
151. Jancarik, J. and S.-H. Kim, *Sparse matrix sampling: a screening method for crystallization of proteins.* Journal of Applied Crystallography, 1991. **24**(4): p. 409-411.
152. Patterson, A.L., *A Fourier Series Method for the Determination of the Components of Interatomic Distances in Crystals.* Physical Review, 1934. **46**(5): p. 372-376.
153. Ullah, J.H., et al., *The crystal structure of the L1 metallo-beta-lactamase from Stenotrophomonas maltophilia at 1.7 A resolution.* J Mol Biol, 1998. **284**(1): p. 125-36.
154. Carine, B., *Metallo-β-lactamases (classification, activity, genetic organization, structure, zinc coordination) and their superfamily.* Biochemical Pharmacology, 2007. **74**(12): p. 1686-1701.
155. Stamp, A.L., et al., *Structural and functional characterization of Salmonella enterica serovar Typhimurium YcbL: an unusual Type II glyoxalase.* Protein Sci, 2010. **19**(10): p. 1897-905.
156. Holm, L. and P. Rosenström, *Dali server: conservation mapping in 3D.* Nucleic Acids Research, 2010. **38**(suppl 2): p. W545-W549.
157. Shimada, A., et al., *The first crystal structure of an archaeal metallo-beta-lactamase superfamily protein; ST1585 from Sulfolobus tokodaii.* Proteins, 2010. **78**(10): p. 2399-402.